Characterization of Silicon Photomultipliers Before and After Neutron Irradiation

Charakterisierung von Silizium-Photomultipliern vor und nach Neutronenbestrahlung

von:
Michael Sergej Nitschke
geboren am
22. Februar 1989

Masterarbeit im Studiengang Physik
Universität Hamburg

2016

1. Gutachterin: Prof. Dr. Erika Garutti
2. Gutachter: Dr. Jörn Schwandt

"Nothing is impossible. Not if you can imagine it. That's what being a scientist is all about."
"No, that's what being a magical elf is all about."
– *Cubert J. and Prof. Hubert J. Farnsworth*

Characterization of Silicon Photomultipliers Before and After Neutron Irradiation

Abstract

In this thesis the influence of neutron irradiation on silicon photomultipliers (SiPMs) is investigated.
SiPMs are detectors made of a matrix of single photon avalanche diodes connected in parallel and operated in Geiger mode, which means that they are operated at a voltage higher than their breakdown voltage. In Geiger mode photons can create electron-hole pairs inside the SiPM that cause charge avalanches, which can be registered as a flowing current. This way a SiPM can achieve up to single photon resolution. Because of their small size and the low price SiPMs became an attractive alternative to photomultiplier tubes.
Several SiPMs from the company KETEK were characterized using current-voltage measurements, capacitance-voltage-frequency measurements and charge-voltage measurements. This was done before having them irradiated with neutrons and afterwards. The goal is to compare the SiPM properties and performance as well as to quantify the influence of neutron induced radiation damages.

Zusammenfassung

In dieser Masterarbeit wird er Einfluss von Neutronenstrahlung auf Silizium Photomultiplier (SiPMs) untersucht.
Als SiPM bezeichnet man einen Detektor bestehend aus einer Matrix von Lawinenphotodioden, die parallel geschaltet und im Geiger Modus betrieben werden. Das heißt, dass sie mit einer Spannung über der Durchbruchspannung betrieben werden. Im Geiger Modus können einzelne Photonen Ladungslawinen auslösen, die als Strom registriert werden können. Dadurch ist es möglich, mit SiPMs einzelne Photonen zu detektieren. Aufgrund ihrer kleinen Abmaße und des günstigen Preises wurden SiPMs zu einer attraktiven Alternative zu Photoelektronenvervielfachern.
Es wurden mehrere SiPMs der Firma KETEK mit unterschiedlichen Messmethoden charakterisiert. Die Messungen umfassten das Aufnehmen von Strom-Spannungs-Kurven, Kapazität-Spannungs-Frequenz-Kurven sowie Spannungs-Ladungs-Messungen. Diese wurden bevor und nachdem die SiPMs mit Neutronen bestrahlt wurden, genommen. Das Ziel ist es, die Eigenschaften und Leistungsfähigkeit der SiPMs vorher und nachher zu vergleichen und den Einfluss neutroneninduzierter Schäden zu quantifizieren.

Table of Contents

1 Introduction **1**

2 Physics Background **5**
2.1 Photon-Matter Interactions 5
2.1.1 Thomson and Rayleigh Scattering 6
2.1.2 Photoelectric Effect 7
2.1.3 Compton Scattering 7
2.1.4 Pair Production 8
2.2 Electron Band Model 8
2.3 Semiconductor Basics 9
2.3.1 Doping of Semiconductors 12
2.4 P-N Junction 14
2.4.1 P-N Junction under Bias 15
2.5 Avalanche Photodiodes 17
2.6 Silicon Photomultipliers 22
2.6.1 SiPM Working Principle 22
2.6.2 Breakdown Voltage 23
2.6.3 Dark Counts 24
2.6.4 Cross-Talk 27
2.6.5 Afterpulses 29
2.7 Radiation Damages in Silicon and Semiconductor Devices 30
2.7.1 Generation of Defects 31
2.7.2 Effect of Radiation Damages in Silicon Photomultipliers 32
2.7.3 Annealing of Defects 34
2.7.4 Methods to Improve Radiation Hardness 34

3 Characterization Methods **37**
3.1 KETEK SiPMs 37
3.2 Current-Voltage Measurements 39
3.2.1 Measurement Setup 40
3.2.2 Forward Bias Characteristic 41
3.2.3 Reverse Bias Characteristic 43
3.3 Capacitance-Voltage-Frequency Measurements 51
3.3.1 CV-f Curve Characteristics 51
3.3.2 Determination of SiPM Parameters 52
3.4 Charge-Voltage Measurements 57
3.4.1 Measurement Setup 58
3.4.2 Charge-Voltage Histograms 60

3.4.3 Determination of the Gain and Breakdown Voltage 64
3.4.4 Determination of the Dark Count Rate 66
3.4.5 Determination of the Cross-Talk and Afterpulse Probability 68

4 Analysis Results **71**
4.1 Current-Voltage Measurements 71
4.1.1 IV Curve Characteristics before Neutron Irradiation 72
4.1.2 IV Curve Characteristics after Neutron Irradiation 74
4.1.3 Investigation of the Quenching Resistance 79
4.1.4 Investigation of the Breakdown Voltage 81
4.1.5 Investigation of the Factor n 85
4.2 Capacitance-Voltage-Frequency Measurements 87
4.2.1 Investigation of the Quenching Resistance and Parasitic Resistance 88
4.2.2 Investigation of the Pixel Capacitance 91
4.2.3 Investigation of the Recharge Time 92
4.2.4 Investigation of the Series Inductance 94
4.3 Charge-Voltage Measurements 96
4.3.1 QDC measurements before Neutron Irradiation 96
4.3.2 QDC measurements after Neutron Irradiation 105

5 Conclusion and Outlook **111**

A Appendix **115**

Literature **117**

B Acknowledgement **123**

Eidesstattliche Erklärung **125**

1 Introduction

Light is an essential part not only of our everyday life but also for life in general. For that reason, it is clear that light has been part of scientific debates for a long time.
Until the beginning of the 20th century it was not clear how to properly and completely describe light and its features. There were constant arguments about light having either a wave- or a particle-like character. At the end of the 19th century, due to research done by scientists like James Clerk Maxwell or Heinrich Hertz, wave models were the mainly accepted models to describe the properties of light [1]. Maxwell's work also proved that visible light is just a tiny fraction of a larger phenomenon, namely electromagnetic waves. However, with the discovery and investigation of the photoelectric effect by e.g. Alexandre Becquerel, Heinrich Hertz or Philipp Lenard and finally the theoretic model established by Albert Einstein, it became clear that light inhibits both particle- and wave-like characteristics. This led to the quantum theory of light that is based on the work of Max Born, Pascual Jordan and Werner Heisenberg. Arthur Compton, known for his discovery of the Compton-effect, eventually established the name $photon$ for the quantum of electromagnetic radiation.

Since then scientists, engineers and technicians have used both characteristics of light in order to detect electromagnetic waves or photons of all wavelengths. This is important in many different applications [2]:
As a part of radiation protection in places like hospitals or nuclear power plants photons have to be detected.
For determining the hazard-free duration of a stay in space for astronauts, it has to be known how much radiation passes through a space shuttle.
In hospitals X-rays are used to acquire images of the interior of the human body. In material science or engineering X-rays are used to detect weak spots in devices and ensure the safety of their users.
Of course the detection of light also plays a big role in physics. Astronomers study our universe by detecting photons emitted by stars thousands or millions of years ago. On the other end of the length scale, particle physicists need to detect photons to investigate collisions of particles in facilities like CERN.
Also one of the latest big discoveries in physics, namely the direct detection of gravitational waves, would not have been possible without photodetectors.

Commonly used devices for the detection of photons from the visible to ultraviolet range are photomultiplier tubes (PMT). Their function is based on the photoelectric effect:
Incoming photons hit a photocathode which then emits photoelectrons. The photoelectrons are accelerated towards an electrode called dynode. When they hit the dynode each

electron creates up to 10 secondary electrons, depending on the voltage. Afterwards, the secondary electrons are again accelerated by another dynodes where the same multiplication takes place. This is repeated multiple times until a large amount of electrons is created, which is then registered as an electric current with an anode at the end of the photomultiplier tube. The tubes are evacuated to ensure that the electrons do not interact with any other particles.
Depending on the kind of radiation that is to be detected, wavelength shifting crystals are placed in front of the PMT to maximize the amount of photoelectrons created [3]. Because PMTs combine a high gain with low noise, a fast response to incoming radiation and a large detection area, they are widely used since the 1930s.
Nonetheless, PMTs have some major drawbacks: They need to be operated with high voltage (normally in kV-range). Additionally, they are hard to miniaturize [4], although some companies like Hamamatsu are developing very small Micro PMTs which also use low voltages [5]. Lastly, due to their operation principle, PMTs cannot be used inside magnetic fields.

In the 1990s silicon based photon detectors became more and more popular and were intensively studied. In the early 2000s a new kind of detector emerged that has been intensely investigated and improved since then [6]. It is called silicon photomultiplier (SiPM)[7], avoids the named disadvantages PMTs have and consequently has replaced PMTs in many applications.
A SiPM is a matrix of single-photon avalanche diodes (SPADs) connected in parallel. In simple terms, a SPAD is a reversely biased p-n junction operated in the so called Geiger mode. This means that the applied reverse voltage at which the SPAD operates is above the breakdown voltage of the diode. Optical photons are able to penetrate into the diode and release electrons via the photoelectric effect. The consequently created electron-hole pairs (ehp) are accelerated by the strong electric field inside the diode and cause a cascade of further ehps due to impact ionizations. If this cascade does not break off and is self-sustaining, it is called Geiger discharge or Geiger avalanche. It results in a current that can be measured.
The advantages of SiPMs, compared to PMTs, are their small size (pixel sizes of down to 15 μm) and the low production prices. Furthermore, they can be operated at low voltages (< 50 V in the case of the SiPMs investigated for this thesis) resulting in low power consumption, and they are insensitive to magnetic fields because they do not rely on accelerating electrons over longer distances.
Of course, SiPMs also have some drawbacks: Compared to PMTs they show a higher dark current and dark count rate (DCR), caused by tunneling effects, thermal excitations, cross-talk (XT) or afterpulses (AP). Furthermore, both of the latter features might even increase by damages due to radiation either by photons or high energy particles. This is a major concern when they are used in radiation environments like in high energy physics experiments. Current experiments involving SiPMs are ILC, ATLAS, ALICE or CMS [8].

Numerous studies on the damages caused by particles and photons have been done in order to understand the underlying physics and to improve the radiation hardness of SiPMs. To cite some of them:
The effects of proton irradiation have been studied amongst others by Y. Musienko et al. [9]. For their studies SiPMs of five different producers (CPTA, FBK, Hamamatsu, Pulsar, Zecotek) were irradiated with 82 MeV protons up to $2 \cdot 10^{10}\, cm^{-2}$ of 1 MeV neutron equivalent flux. The irradiation resulted in a serious increase of the leakage current and the dark count rate (DCR) of the devices. The Zecotek and FBK devices showed the smallest increase ($\approx$ factor 6) and the Hamamatsu devices the largest increase ($\approx$ factor 12) at excess voltages up to 6 V. On the other hand, no changes in the breakdown voltage and quenching resistance were observed. The CPTA and Pulsar devices showed a significant reduction of the signal amplitude at high excess voltages (V_{exc}> 4 V). The Zecotek SiPM also showed a significant decrease at low excess voltages.
The effects of neutrons were investigated by Y. Qiang et al. [10]. To create neutron irradiation they hit a thin lead target with a 1 GeV electron beam. This method was chosen because it allowed them to have SiPMs operating and illuminated with an LED while being irradiated. The fluence reached in this way was $3.7 \cdot 10^9\ n_{eq}/cm^2$. They found that the DCR and the dark current at a fixed excess voltage increased linearly with the neutron fluence. Also they observed that part of the acute damage would permanently recover at a certain temperature and that raising the temperature leads to even further recovery.
X-ray irradiation studies have been done by C. Xu et al. [11]. They irradiated SiPMs with X-rays to doses of up to 20 MGy. Their results showed that up to doses of 20 kGy the performance of the SiPM is barely affected by X-ray radiation damage. For higher doses significant increases in the DCR and the cross-talk probability were observed whereas the gain stayed nearly constant. The DCR increased about an order of magnitude for excess voltages above 1.8 V and the cross-talk probability increased by up to 50 %.
Possible ways to improve the radiation hardness of silicon detectors in general were presented by G. Lindström et al. [12] as well as by G. Casse et al. [13]. Both observe that enriching silicon with oxygen has a positive influence on the radiation hardness of silicon detectors. Furthermore, they conclude, that operating the devices at low temperatures and using guard ring structures is helpful for operating these devices in radiation environments.
For the specific case of SiPMs there are e.g. studies by T. Nakamori [14]. They investigated several new designs for SiPMs in terms of their X-ray radiation hardness. Their conclusion is that in order to obtain radiation hard SiPMs, it is best to use small pixel sizes (SiPMs with 15 μm pitch performed better than those with 100 μm), operate them at small excess voltages and try to minimize the after-pulse probability.

The aim of this thesis is to contribute to these studies and to investigate the effects of neutron irradiation on SiPMs manufactured by KETEK. For this, 20 samples of KETEK SiPMs have been characterized using different measurements procedures. These procedures in-

clude current-voltage (IV) and capacity-voltage-frequency measurements (CV-f) as well as charge-voltage measurements (QDC measurements, since they include a charge to digital converter (QDC) as an essential part of the setup). The characterization has been done before and after neutron irradiation at different fluences, ranging from 10^9 n_{eq}/cm^2 to 10^{12} n_{eq}/cm^2, in order to quantify the impact of the damages.
The IV- and CV-f measurements are used to determine static features of the SiPM. Observables extracted from IV-/CV-f curves are the pixel capacitance, the quenching resistance and the breakdown voltage. On the other hand, from the charge-voltage measurements dynamic features of the SiPM were obtained. In this case dynamic means, that they are not constant and depend on the applied voltage. The extracted observables are gain, DCR, XT and AP probability but also the breakdown voltage.
While the IV- and CV-f measurements and their respective analysis could easily be repeated with the irradiated samples, the same was not possible for the charge-voltage measurements. Their analysis depends on the discrimination of signals/peaks from single pixels discharging. Due to the high dark current after irradiation this discrimination was no longer possible for all the devices. A way to resolve this is to repeat the charge-voltage measurements at low temperatures (-40 °C [15]) but the setup used in the course of this thesis did not provide this possibility.

The thesis is divided into three main chapters. The first chapter presents the theoretical description of the physical processes that are relevant to understand the working principle of silicon detectors in general and SiPMs in particular. Additionally, the mechanisms of radiation damage in silicon are described with a focus on the damage caused by neutrons.
In the second chapter the three different kinds of measurements are described, namely the IV-, CV-f and QDC measurements. The chapter includes information about the basic principles of the measurements, the setups used as well as the analysis used to extract relevant observables from them.
The third chapter contains the measurement results from before and after irradiation. These results are compared and explanations for the observed or absent changes are given.
The thesis is closed by a short conclusion of the work done and an outlook on planned future studies and possible improvements.

2 Physics Background

The intention of this chapter is to give a short overview of the theoretical background needed to understand the physical processes and phenomena discussed in this thesis.
Section 2.1 is about the interaction of photons with matter. This is crucial to understand the detection mechanism of photons in a SiPM, that is based on the photoelectric effect.
In section 2.2 the electron band model is explained, which is the theoretical basis for solid state detectors. This model is able to explain the properties of semiconductors that make them suitable for the detection of photons.
The basics of semiconductors are then described in section 2.3. It also contains a sub chapter about the doping of semiconductors, a technique that is applied in every modern semiconductor device including SiPMs.
When two oppositely doped regions are combined in a semiconductor device (so called *p-n junction*), a depleted region is formed. Its properties are discussed in section 2.4.
Section 2.5 introduces avalanche photodiodes, devices that are making use of the p-n junction in order to detect photons. As already mentioned, in a SiPM there are many (up to thousands) of these photodiodes connected in parallel.
Why it is makes sense to connect thousands of photodiodes in parallel and thus creating a SiPM, is explained in section 2.6. Topics covered in this section are the working principle of these devices, their breakdown voltage, the cause of dark counts and also cross-talk and afterpulses.
In the last section 2.7, the topic of radiation damages is addressed. Their generation, the resulting effects on silicon and SiPMs as well as how they can be avoided or even undone are discussed.

2.1 Photon-Matter Interactions

The working principle of a SiPM or semiconductor detectors in general is based upon the interaction of photons with matter. This chapter will give a brief overview of those interactions as described in [16].
Foundation for the correct description of interactions of light with matter is the quantum nature of light. That is to say, the fact that light shows both wave-like and particle-like behavior. For a long time, light was thought to be either of corpuscular nature (Newton's corpuscular theory of light [17]) or of wave-like nature (Thomas Young's wave theory [17]). With the development of the quantum theory and the description of light with photons of discrete energy depending on their frequency f or wavelength λ it was possible to describe on an atomic scale what happens when light interacts with matter. The

energy of a photon can be calculated according to the formula [1]:

$$E = h \cdot f = \frac{h \cdot c}{\lambda} \tag{2.1}$$

Optical photons have a wavelength of 380 nm (blue light) to 750 nm (red light), which corresponds to energies of 3.26 eV to 1.65 eV.
Depending on the energy of the photon that is interacting with a solid state body, there are several possibly occurring phenomena: Photon excitation, where the energy of an absorbed photon causes an atom or molecule to jump to a higher energy state, Thomson and Rayleigh scattering, the photoelectric effect, Compton scattering or pair production. The latter four processes will be described in this chapter with a focus on the photoelectric effect, because this effect dominates in the energy region of visible photons (see Fig. 2.1).

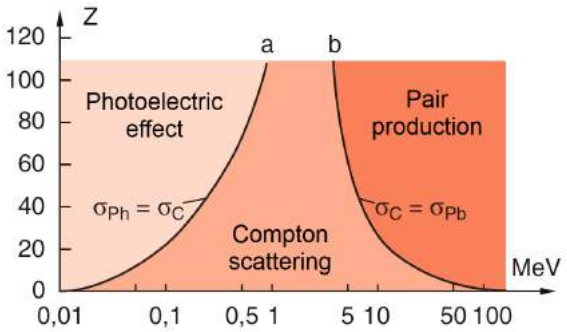

Fig. 2.1: Dominant light matter interaction effects as a function of the atomic number Z and the photon energy E_γ. For small energies the photon effect is dominant [16].

2.1.1 Thomson and Rayleigh Scattering

An effect that is still explainable using classical electrodynamics is the Thomson scattering. It describes the elastic scattering of electromagnetic radiation by a charged particle. In the classical model, the scattering happens because the electric field of the incoming wave accelerates the charged non-relativistic particle, which results in the particle emitting radiation with the same frequency as the incoming wave. As a consequence the kinetic energy of the particle as well as, looking at the process quantum-mechanically, the frequency of the incoming photon will remain the same. Thomson scattering occurs for low energy photons (of the radio or microwave range) with $f \ll \frac{m \cdot c^2}{h}$ [16] , where m denotes the charged particle's mass.
If a electromagnetic wave is scattered by neutral polarizable particles, one speaks of Rayleigh scattering. In the case of Rayleigh scattering, the wave also accelerates the particle with the difference that it induces a dipole moment, in order to have the neutral particle emit electromagnetic radiation again.

2.1.2 Photoelectric Effect

For photons with higher energies (i.e. the range of visible to ultraviolet light) there is the possibility of the photon being absorbed by a shell electron of the interacting atom. The absorbed energy will cause the electron to be ejected with a resulting kinetic energy of [18]:

$$E_{kin} = h \cdot f - E_b \tag{2.2}$$

where E_b stands for the binding energy of an outer shell electron. From this equation it becomes clear that the photons have to have an energy higher than the binding energy of the outer shell electron, i.e. $h \cdot f > E_b$ [2]. In a silicon crystal the binding energy is 1.12 eV, whereas the binding energy for an electron in a single atom ranges between 1839 eV for the 1s orbital and 99 eV for the 2p orbital [19].
Since the photon is absorbed, the interacting atom has to take up some of the photons momentum otherwise momentum and energy conservation would be violated. In other words, there can be no photoelectric effect on free electrons. Another consequence of this is, that the photoelectric absorption probability is higher for more tightly bound electrons. So as soon as the incoming photon has an energy high enough to release an electron from the inner shells, the ejected electron will be mostly from one of the inner shells.
Depending on where the released electrons go, the photoelectric effect is classified into the outer or inner photoelectric effect.
If the electron leaves the surface of its solid state body, we speak of the outer photoelectric effect. On the other hand, if the electron stays within the solid state body and moves to a different atom, where it could for example be available as an conduction electron, we speak of the inner photoelectric effect.
The inner photoelectric effect is what makes the detection of photons with a SiPM possible.

2.1.3 Compton Scattering

If the photon energy is way higher than the binding energy of the interacting electron, i.e. if $h \cdot f \gg E_b$, the electron can be seen as free from the photon's point of view [18]. Compton scattering describes a direct elastic collision between the two. Under those circumstances, the photon will give part of its energy and momentum to the electron, resulting in a change of the photon's wavelength. Depending on the angle under which the photon is scattered the amount of energy varies. If the photon back scatters, i.e. if the scattering angle is 180°, the maximal amount of energy is transferred.

2.1.4 Pair Production

As soon as the energy of the incoming photon is larger than twice the rest mass energy of an electron, in other words larger than $2 \cdot m_e c \approx 1.02\ MeV$, it may produce an electron-positron pair as it interacts with a charged particle. Due to momentum conservation this can only occur close to a charged massive object that can take up the excessive amount of momentum, while the photon interacts with this object's Coulomb field. The photon's threshold energy E_{th} for this to happen depends on the rest mass M of the charged particle [18]:

$$E_{th} = 2m_e c^2 + \left(1 + \frac{m_e}{M}\right) \tag{2.3}$$

So the lighter the charged particle is, the more energy the photon needs to create an electron-positron pair.

2.2 Electron Band Model

SiPMs are semiconductor devices. To understand what a semiconductor is, the band model of solid state materials has to be understood. This model is (next to many other things) able to explain why some materials are conductors while others are isolators [2]. Typical isolators have a specific resistance of $10^{10}\ \Omega \cdot m$ and higher, whereas conductors might have a specific resistance of $10^{-8}\ \Omega \cdot m$. The explanation of this large difference lies in the reciprocal electromagnetic influence of atoms. If two atoms approach each other their energy levels will change. In the case of e.g. two approaching hydrogen-atoms with n=2 (corresponds to 3.4 eV) the two former degenerated energy levels will split into two different states as soon as the atoms distance goes below a certain value.
When N equal atoms approach, so that their electronic orbits overlap, their degenerate energy levels will also split up, but in this case in N different energy levels. In Fig. 2.2 for example the splitting of two energy levels for six atoms as a function of distance between them is shown [2].

Furthermore, if we look at a solid state body with $N > 10^{23}\ atoms/cm^3$ there will be a similar amount of energy levels whose difference in energy is so small that the levels can be seen as a continuum. This continuum is called *energy band*. For N degenerate energy levels in a combination of atoms there will be N energy bands. The crucial bands are the two highest bands, which are called *valence* and *conduction band*. Assuming a temperature of 0 K, the valence band is the highest occupied band while the conduction band is the first unoccupied band. These bands can be energetically close (a few eV) or far (tens of eV) from each other and they might even overlap [20].
In the latter case, the material is a conductor. Since the valence and conduction band

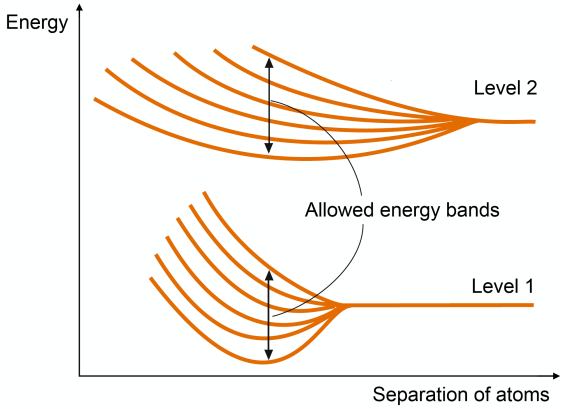

Fig. 2.2: Splitting of the two energy levels of six equal atoms as a function of distance.

overlap, the unoccupied energy levels are energetically right above the occupied ones and electric fields may easily excite valence electrons to jump into states of the conduction band, resulting in a current. On the other hand, filled bands do not contribute to electrical conductivity, because electrons are fermions and can only move to unoccupied states. So if there is an energy gap between the highest filled and the next empty band, a comparable electric field will not cause a current inside the material at 0 K. However, in the case of a small band gap, above 0 K the thermal energy of the solid may suffice to excite valence electrons into the conduction band, thereby causing a current when an electric field is applied. In contrast to conductors, the resistivity of semiconductors decreases with increasing temperatures.
In conductors the resistivity rises with increasing temperatures. The reason for this is that the mobility of electrons declines, because raising the temperature results in stronger lattice vibrations, thus more collisions between electrons and atomic nuclei occur [2]. This also happens for semiconductors. However, in semiconductors an increase of the temperature also allows more electrons to move to the conduction band and this effect dominates. Further properties of semiconductors are explained in the following chapter.

2.3 Semiconductor Basics

Above 0 K it is possible that an electron of the full valence band is thermally excited, leaves the valence band and occupies a state in the conduction band. This electron can now contribute to a current. In addition to this, whenever an electron leaves the conduction band, an empty state is left behind. These empty states are called holes. If an electric field is applied, all the electrons in the valence band will move in the opposite direction of the electric field. Since all the free electrons have a momentum/wave vector k_e and the momentum has to be conserved, the holes have to have a momentum $k_h = -k_e$ [3]. This results in a movement of the holes in the direction of the electric field. The holes

behave like positive charges moving through the semiconductor (see Fig. 2.3). Nonetheless, it is not really a positive charge that is moving, but instead electrons from the valence band that are occupying the vacant energy states thus resulting in a current that can be described as a current of positive charges.

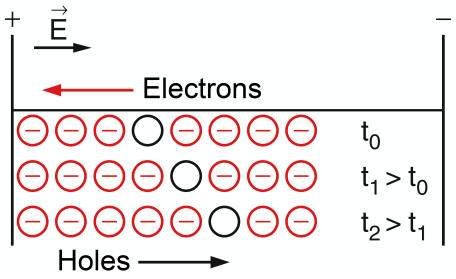

Fig. 2.3: Scheme of the conductance of holes in the valence band of a semiconductor [3].

A main feature of semiconductors is their negative temperature coefficient of resistivity. Similar to conductors increasing the temperature results in increased scattering of electrons by the lattice ions due to thermal vibrations. However, unlike in conductors the conductivity of semiconductor still increases with rising temperature because the effect of having more free charge carriers available for conductance dominates [21]. This does not only happen because more electrons are excited thermally but also because the bandgap decreases with increasing temperature, which can be seen in Fig. 2.4.

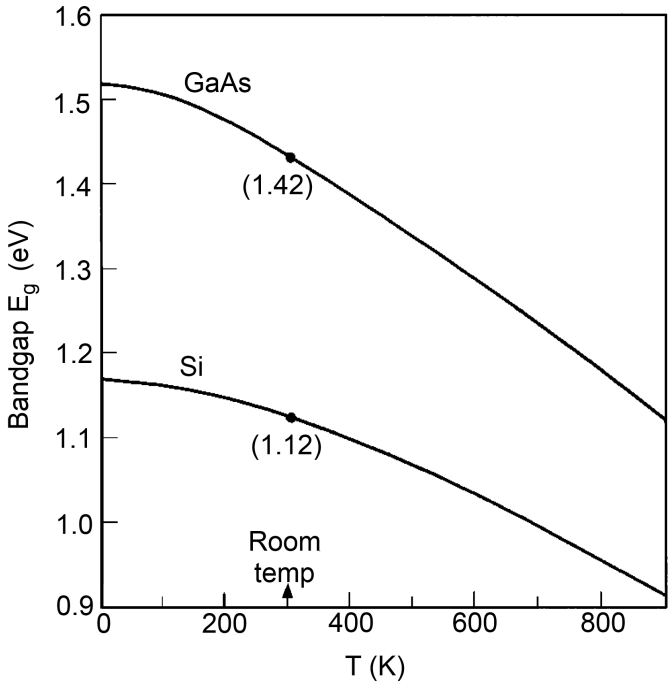

Fig. 2.4: Temperature dependence of the energy bandgaps of Si and GaAs. In both cases E_g decreases with increasing temperature [21].

The conductivity of semiconductors is based on electrons leaving the valence band and

occupying states in the conductance band. However, there a two ways this can take place. Semiconductors can either have a direct or an indirect bandgap. Whether a material is a direct or indirect semiconductor depends on the relation between the valence and the conductance band. This can be seen in the momentum space: In most semiconductors the maximum of the valence band occurs at an effective momentum $k = 0$, in the center of the Brillouin-zone [20]. The position of the minimum of the conductance band now determines the type of semiconductor:
In direct semiconductors the minimum lies directly above the maximum of the valence band at $k = 0$. Whereas in indirect semiconductors the minimum lies a finite momentum vector away from the top of the valence band (see Fig. 2.5). Examples for direct semiconductors would be gallium arsenide or gallium nitride and indirect semiconductors are for example germanium or silicon. Silicon has a direct bandgap of 3.4 eV and an indirect bandgap of 1.12 eV.

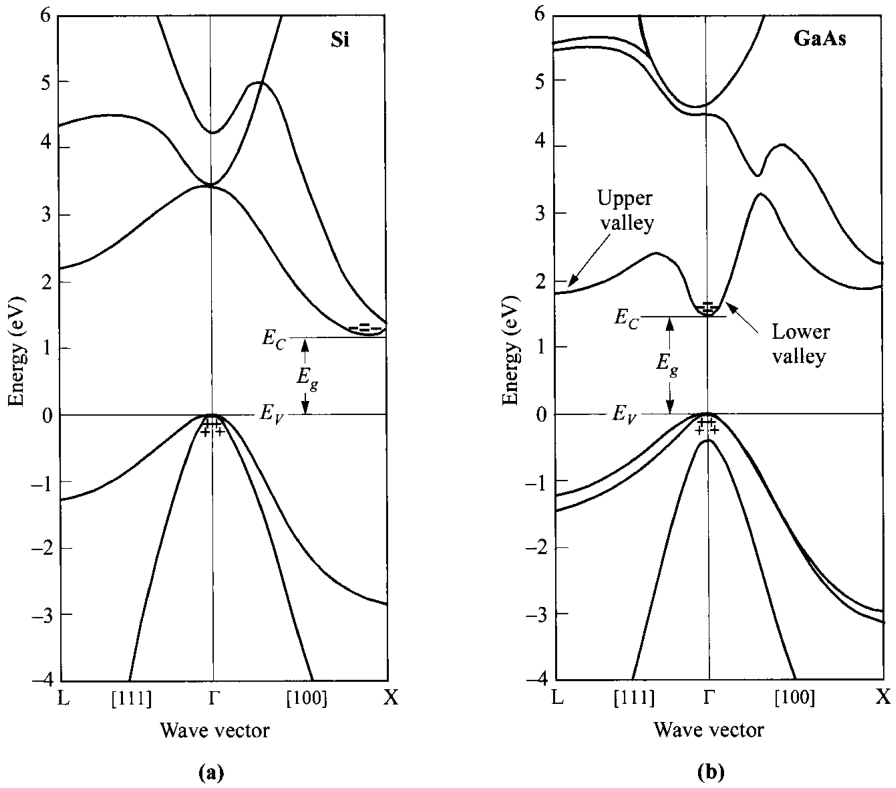

Fig. 2.5: Energy bands of Si (a) and GaAs(b). E_g stands for the energy bandgap, E_C for the energy of the conduction band and E_V for the energy of the valence band. The plus signs mark holes whereas the minus signs mark electrons. The difference between an indirect bandgap (Si), where the extrema of the bands are not on top of each other but separated by a finite wave vector, and a direct bandgap (GaAs), where they are on top of each other, can be clearly seen [21].

In the case of direct semiconductors, a photon with an energy larger than the bandgap is able to create an electron-hole-pair on its own. On the other hand, in indirect semiconductors the small momentum of the photon is not sufficient and an additional phonon

(e.g. from thermal excitations) is needed to ensure momentum is conserved. This can be seen in Fig. 2.6. As a result direct semiconductors have a higher interaction with light than indirect semiconductors and absorb light more easily.

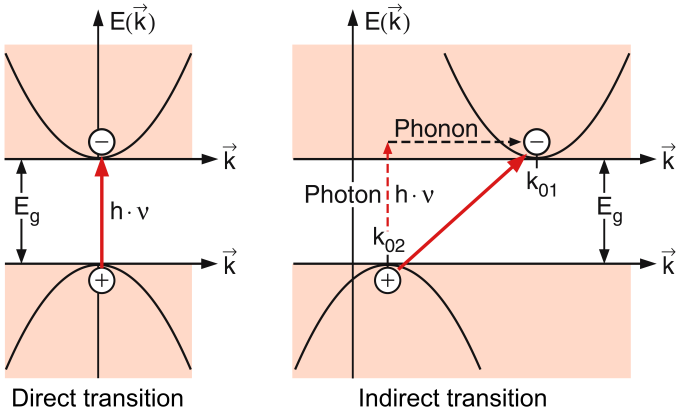

Fig. 2.6: Direct and indirect transitions inside a semiconductor taking place when a photon is absorbed. In the case of an indirect transition an additional phonon is required to conserve the momentum [3].

2.3.1 Doping of Semiconductors

In technical applications it is common to increase the conductivity of semiconductors by adding impurity atoms to the main material. This procedure is called *doping* and it is crucial to the avalanche process taking place in a SiPM pixel. Doping can be done by heating up the original material and adding impurity atoms, which then disperse in the crystal by diffusion. Another possibility is to shoot the impurity atoms as ions with high energy (in the range from some 100 eV to keV) into the original crystal [22]. The inserted atoms can then be placed on an interstice or replace a regular atom in the crystal lattice.
In silicon, which has four electrons in its valence shell, each of the electrons forms a covalent bound with one of the four neighboring atoms (diamond structure). Now one can either add atoms that have one valence electron more (e.g. Arsenic or Phosphorus) or one valence electron less (e.g. Boron or Gallium). This is what is usually done, but it is also possible to add impurities with more than one valence electron more/less [23].
In the first case, four of the five valence electrons of each impurity atom will be used to form the covalent bound, while the fifth is not participating in this bond and is just attracted by the coulomb force of the neighboring ion rumps. This results in an excess of weakly bound electrons that can easily be excited into the conduction band and then contribute to the electrical conduction. Because of the excess of negative charges semiconductors doped in this way are called *n-type* semiconductors. In the band model the energy levels of the excess electrons are just below the conduction band and because they can donate electrons to the conduction band without leaving holes in the valence band,

they are named *donor levels*.
Similar to this, adding atoms with one valence electron less, causes an excess of holes. These holes can be easily occupied by electrons which results in a movement of the holes which is equal to a positive current. The empty energy levels introduced in this way lie just above the valence band and are called *acceptor levels* because of their ability to accept electrons. Semiconductors doped with acceptor impurities are called *p-type* semiconductors. In Fig. 2.7 examples of n- and p-type doping in silicon and the resulting energy levels are shown.

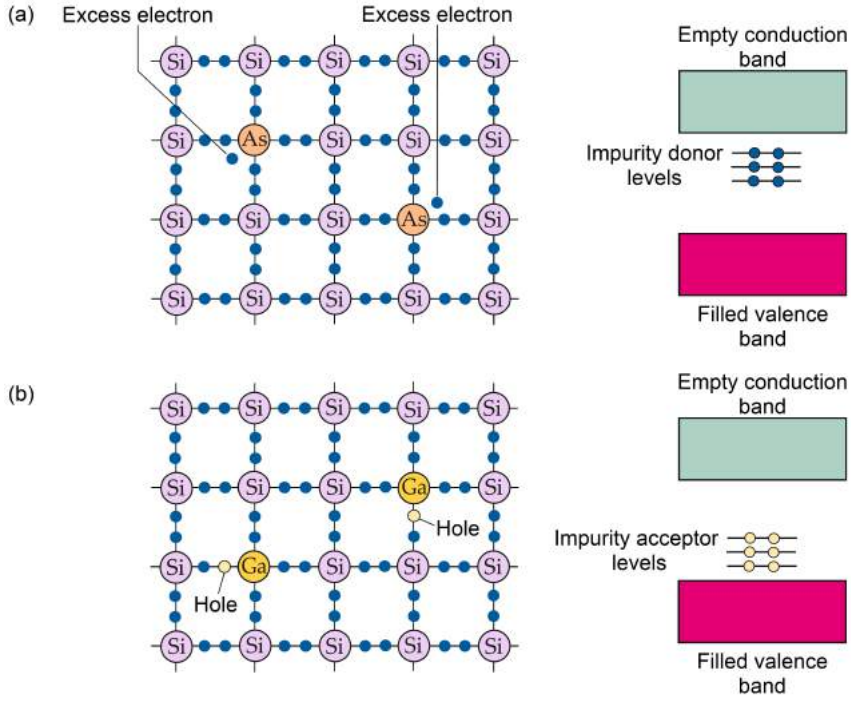

Fig. 2.7: Left side: Lattice structures of (a) n-doped Si with added As-atoms and (b) p-doped Si with added Ga-atoms. On the right side a scheme of where the impurity levels are situated with respect to the valence and conduction band is shown [23].

To indicate the density of doping, superscripted plus or minus signs are used. A strong doping is depicted with a $+$, corresponding to a doping of $10^{18} - 10^{20}\ cm^{-3}$ impurity atoms. Even higher dopings are marked with two plus signs. For weakly doped areas a $-$ is used, this corresponds to a doping of $10^{13} - 10^{15}\ cm^{-3}$ impurity atoms. If neither a $+$ or a $-$ sign is used, the doping is around $10^{15} - 10^{18}\ cm^{-3}$ [24] [25].

P- vs N-Type Conductivity

The type of the semiconductor also determines which charge carriers dominate the conductivity. In an undoped or intrinsic semiconductor both the number of acceptors N_A and the number of donors N_D are equal to zero: $N_A = N_D = 0$ and the density of charge

carriers is $p = n = n_i$, where n_i is the intrinsic charge carrier density (pure silicon at room temperature has $n_i \approx 9.7 \cdot 10^{15} m^{-3}$ [21]). From the Fermi-distribution which describes the density of charge carriers it follows that [26]:

$$n \cdot p = n_i^2 \tag{2.4}$$

In p-type semiconductors mainly the holes contribute to the conductivity and it holds: $N_A \neq 0,\ N_D = 0$ thus $p \gg n$ and $p > n_i$. Consequently, holes are the majority charge carriers and electrons the minority charge carriers.
The opposite holds in n-type semiconductors where the electrons dominate the conductance: $N_A = 0,\ N_D \neq 0$ thus $n \gg p.$ and $n > n_i$. Hence, holes are the minority charge carriers and electrons the majority charge carriers.
Of course there also exist mixed types of semiconductors. Furthermore, the situations of $N_A = 0$ or $N_D = 0$ are purely theoretical. In real semiconductors it holds either $N_A \gg N_D$ or $N_D \gg N_A$ respectively.

2.4 P-N Junction

In many technical applications like LEDs or transistors, n- and p-type semiconductors are combined and put on top of each other. The simplest device created in this way is a *p-n diode*, which consists of an n-doped and a p-doped side and electric contacts at each side. By combining the two types of doped semiconductors a transition layer, the so-called *p-n junction* is created [3].
If a p- and an n-type semiconductor are directly connected, a steep gradient of charge carrier concentrations is created and the charge carriers try to reach the equilibrium state of $n = p = n_i$ (see equation (2.4)). This means that the excess electrons diffuse from the n- to the p-region and vice versa, the excess holes diffuse from the p- to the n-region. In the region near the junction, holes and electrons will recombine so that a region with barely any free charge carriers is generated. This region is called *depletion zone* or *space charge region* and has a high resistivity. As a consequence of electrons leaving the n-zone and holes leaving the p-zone, there are positive donor ions left behind in the n-zone as well as negative acceptor ions in the p-zone. In the p-zone a negative space charge density is then formed and a positive space charge density in the n-zone. As a result, an electric field arises at the p-n junction pushing the diffused charge carriers back to their original position. The electric field reaches its peak value at the junction and can be calculated using [21]:

$$E_{peak} = -\frac{q_0 \cdot N_D \cdot W_{Dn}}{\epsilon_r} = -\frac{q_0 \cdot N_A \cdot W_{Dp}}{\epsilon_r} \tag{2.5}$$

Where q_0 is the elementary charge, ϵ_r the relative permittivity of the solid, N_D and N_A are the donor/acceptor concentrations and W_{Dn}, W_{Dp} are the widths of the space charge region in the n- and p-region. The width of the space charge region is called *depletion width* W_D and is a function of the built-in voltage V_{bi} as well as the doping concentrations N_A and N_D. It can be calculated by using the following formula [21]:

$$W_D(V_{bi}) = W_{Dn}(V_{bi}) + W_{Dp}(V_{bi}) = \sqrt{\frac{2\epsilon_r}{q_0} \cdot \left(\frac{N_A + N_D}{N_A \cdot N_D}\right) \cdot V_{bi}} \tag{2.6}$$

At one point, a dynamic equilibrium between diffusion and drift current sets in. What follows is a constant potential difference (i.e. a voltage) that prevents any further charge flow. This is called *built-in voltage*, since it is present even in the absence of any external bias. In Fig. 2.8 the p-n junction, the depletion zone and the described features are depicted. The figure shows an *abrupt junction*, which is a p-n junction with one side having a considerably higher doping than the other.
In addition to this, the energy-band scheme of the p-n junction is also shown in Fig. 2.8. Following the formula $E = q_0 \cdot U$, the built-in voltage results in a bending of the energy bands at the junction [3]. The built-in voltage and consequently the bending of the energy is depending on the concentrations of the minority and majority carriers. The higher their concentrations the higher the built-in voltage and the energy bending become. This can be seen in the following equation [20]:

$$V_{bi} = \frac{q_0 \cdot N_D \cdot W_{Dn}^2}{2\epsilon_r} + \frac{q_0 \cdot N_A \cdot W_{Dp}^2}{2\epsilon_r} \tag{2.7}$$

2.4.1 P-N Junction under Bias

As mentioned before SiPMs are operated with a reverse voltage applied. But what does that mean? The dynamic equilibrium of drift and diffusion currents in a diode is disturbed as soon as a voltage is applied at the p- and n-zone. There are two possibilities in applying a voltage:
Firstly, having the positive pole connected to the p-zone and the negative to the n-zone. This is called *forward biasing*.
Secondly, having the negative pole connected to the p-zone and the positive to the n-zone. This is called *reverse biasing*.
What happens in each of the cases can be easily seen looking at equation (2.6). The potential difference V_{bi} is exchanged with $V_{tot} = V_{bi} - V_{forw}$ or $V_{tot} = V_{bi} + V_{rev}$ (where V_{forw} and V_{rev} have a positive value) [20].
Forward biasing results in a decrease of the depletion width because the charge carriers are pushed towards the junction. The excess electrons from the p-region are pushed to

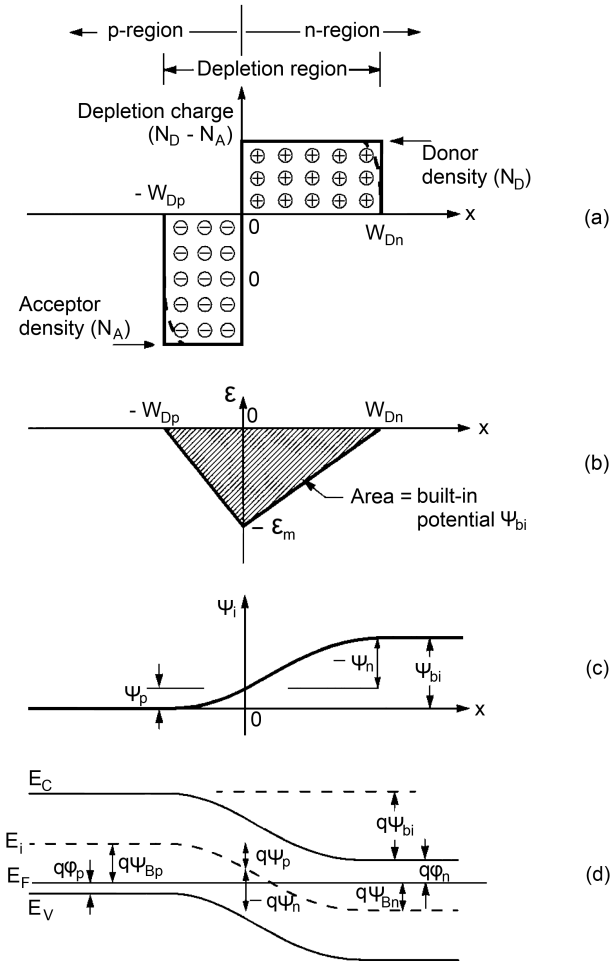

Fig. 2.8: Properties of an abrupt p-n junction. (a) Space-charge distribution. (b) Electric field distribution. (c) Potential distribution showing the built-in potential. (d) Energy-band scheme [21].

the n-region and the excess holes from the n-region to the p-region where they recombine. The charge carriers removed due to recombination get replenished by the contacts at the n-/p-region, which results in the forward current.

It is possible to divide the contributions of the recombining charge carriers to the current into three parts, depending on where the recombination takes place. Firstly, electrons and holes can recombine in the neutral n-doped zone. Secondly, they can recombine in the neutral p-doped zone and thirdly, the recombination can happen in the space charge region. If the recombination occurs within one of the neutral zones, the resulting current is called diffusion current. If it occurs within the space charge region, we speak of recombination current. Since the space charge region diminishes with increasing forward bias, the contribution of the recombination current decreases with voltage until the diffusion current dominates [26].

Reverse biasing results in an increase of the depletion width because the free charge carriers are pulled away from the junction. A reverse biased diode is high-ohmic and just

a small current is flowing. Unlike the forward current, the reverse current is not based on recombination of electrons and holes but on the generation and separation of electron-hole pairs. There are two contributions to this current: *generation* and *diffusion current* [26]. The generation current is caused by the spontaneous/thermal generation of electron-hole pairs inside the depletion region that get separated because of the applied voltage. In a silicon p-n junction this is the dominant contribution to the reverse current [21].
The diffusion current as the name implies is based on diffusion: Even without an electric field in the semiconductor, electron-hole pairs created outside the depletion region can be separated since they have a thermal velocity. The electrons and holes will then diffuse from a place with higher charge carrier concentration to a place with lower concentration, in order to restore the equilibrium. When a charge carrier reaches the edge of the space-charge region two cases have to be distinguished:
Electrons from the n-region and holes from the p-region reaching the edge will be pushed back. Whereas holes from the n-region and electrons from the p-region will be swept toward the opposing side by the electric field of the space-charge region. Consequently, the diffusion current is created by the minority carriers, because the majority carriers moving towards the opposite side will be reflected at the space charge region and move back.
In both cases, the charge carriers will then be extracted via the electric contacts which results in a current called *leakage current*.
Reverse biased diodes will nevertheless become conducting if the applied voltage is high enough. The reason for this *breakdown* is that at a certain level the electric field is strong enough to strip of electrons from their atomic bonds and accelerate them across the junction [23]. The voltage at which this process starts, is called *breakdown voltage* and if the applied voltage is increased even more, the accelerated electrons can cause impact ionizations, which result in more electrons causing even further impact ionizations. Hence, an avalanche of charge carriers is triggered that gives this process the name *avalanche breakdown*. Fig. 2.9 shows the current of a diode as a function of voltage in forward and reverse direction.

2.5 Avalanche Photodiodes

Devices that are making use of the avalanche multiplication to detect photons are avalanche photon diodes (APDs) and single-photon avalanche diodes (SPADs) [27]. In Fig. 2.10 a cross-section of an APD as well as its electric field, assuming uniform doping, is shown. As it can be seen, the design includes more than a simple p-n junction. Instead there are additional p-regions, an n-doped guard ring and an SiO_2 layer on top of the junction. The SiO_2 works as an anti-reflective layer. The guard ring is built-in to create a more uniform electric field in the multiplication zone to avoid breakdown due to high field regions at the edges.

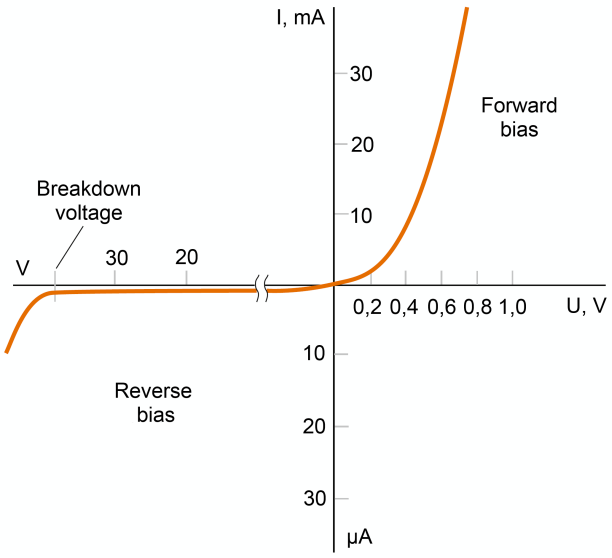

Fig. 2.9: Current-voltage characteristic of a diode. A forward biased diode allows a high current to flow whereas with reverse biasing below breakdown there is only a minimal current flowing. Above breakdown, the current increases by multiple orders of magnitude [23].

APDs are operated at reverse bias below the breakdown voltage [18]. Incoming photons create electron-hole pairs by the photoelectric effect and the E-field separates electrons and holes from each other. The reverse biasing causes an electric field that is high enough to strongly accelerate the charge carriers so that they can create new electron-hole pairs by impact ionization. After the collisions they gain enough energy to cause further ionizations. This leads to a charge avalanche. In other words, in an APD a single photoelectron is able to produce an amplified current signal. It should be mentioned, that the probability of creating secondary electron-hole pairs depends on the electric field and is different for electrons and holes. In silicon, electrons have a higher ionization rate than holes thus the avalanches are mainly initiated by electrons [28].
Because of the intrinsic signal amplification it is possible to use APDs for low intensity light detection and in the case of SPADs to detect single photons.
While APDs and SPADs can technically be designed in the same way, the difference between an APD and a SPAD is that APDs work close to but below the breakdown voltage, while SPADs are operated at 10 to 20 % above breakdown [18].
Their gain is a function of temperature and applied voltage. In the case of APDs it is in the range of several hundred whereas SPADs can reach gains up to thousands. The advantage of a lower reverse biasing is that APDs work in the linear mode, in which the current created is proportional to the detected light intensity. In contrast to this, SPADs work in a highly non-linear region that allows single photon detection (see Fig. 2.11). However, this comes at the cost that one is not able to distinguish the signal of two or more incoming photons from the signal caused by a single photon anymore. In both

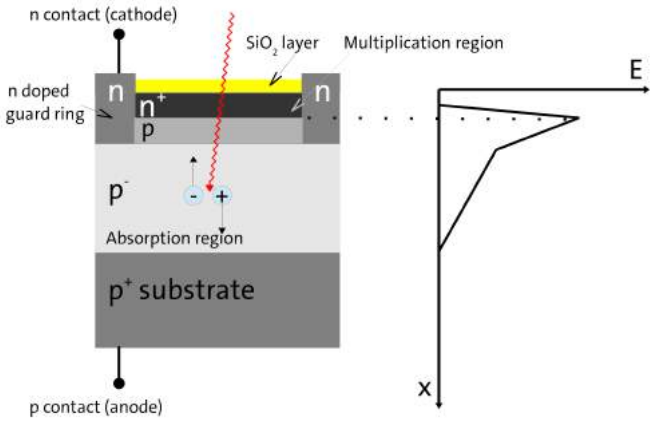

Fig. 2.10: Left: The doping scheme of an avalanche photodiode built on a p-type substrate. On top there is an SiO_2 layer as well as an n-doped guard ring. During operation the depletion region covers parts of the n $^+$-layer and the entire p-layer. The p$^-$-layer below is where most of the absorption takes place. Right: The corresponding strength of the electric field inside the APD. It is highest at the p-n junction [27].

cases an avalanche will be caused that, as long as the number of extracted charge carriers is smaller than the number of newly created electron-hole pairs, is self-sustaining. For this reason SPADs are also called digital detectors [27]. This means that it can only distinguish between 1 = arriving photon(s) and 0 = no arriving photon(s), but is not able to count the number of photons that have triggered the avalanche.

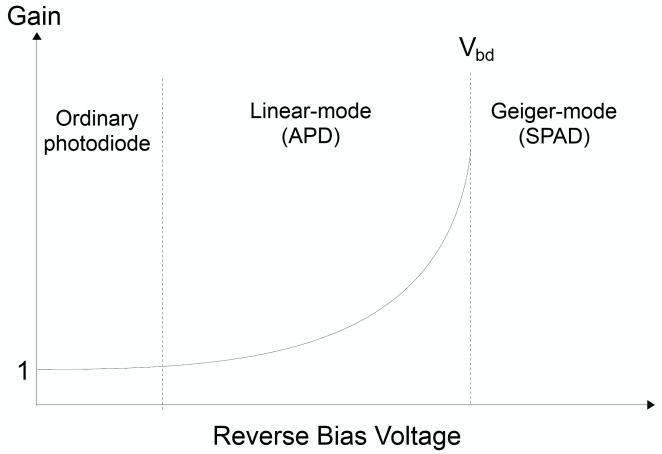

Fig. 2.11: The curve shows the gain of a photodiode as a function of reverse bias. While an 'ordinary' photodiode has no amplification (i.e. gain) the APD that is driven close to breakdown has a gain up to a few hundreds. In SPADs, that are operated above breakdown, the gain is virtually infinite [29]. The picture is remade from [27].

One possibility to stop these avalanches and allow the detection of further incoming photons is to add a high-ohmic resistor ($100\ k\Omega - 1\ M\Omega$) in series called *quenching resistor*

[18]. Another reason to include this resistor is to prevent thermal damage to the device due to the high currents.
The resistance of the quenching resistor is much higher than the resistance of the diode and induces a voltage drop that reduces the voltage on the photodiode to or slightly below the breakdown value. The avalanche will stop and after a short recharge time (~ns), in which the voltage ramps up to its original value before the avalanche, the SPAD is able to detect further incoming photons.
The dead time is a direct consequence of the quenching process. Fig. 2.12 shows an equivalent circuit diagram of a SPAD as well as a graph of the voltage and current demonstrating the quenching process.

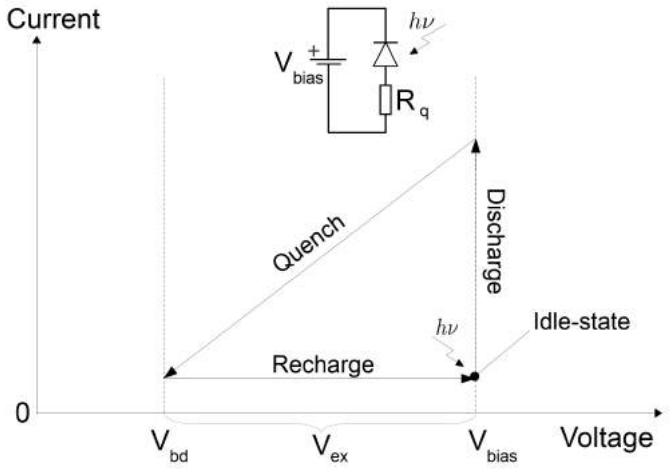

Fig. 2.12: In the upper insert, the equivalent circuit diagram of a reverse biased SPAD is shown. Below, the different steps of the passive quenching process and their current voltage dependence are depicted. After a photon has been absorbed, the SPAD discharges which results in a high current. The discharge is followed by the quenching resulting in a voltage and current drop. Once the quenching is finished, the cell can recharge and go back to its idle-state [27].

A SPAD is basically a series circuit of a resistor and a diode. The diode can be simplified as a capacitance because of its p-n junction. After the avalanche is stopped and the voltage has dropped, the capacitance has to recharge before photons can be detected again. The time constant of the recharge process τ_r can be calculated using [18]:

$$\tau_r = R_q \cdot C_{pix} \tag{2.8}$$

Where R_q is the quenching resistance and C_{pix} the capacitance of the diode, which is also called pixel capacitance. Typical values for C_{pix} are in the range of femtofarad and it is dependent on the pixel size as well as the doping concentration. A rough approximation of the pixel capacitance can be made using the formula of a parallel plate capacitor [30]:

$$C_{pix} \approx \epsilon_0 \epsilon_r \cdot \frac{A}{d} \tag{2.9}$$

where ϵ_0 is the vacuum permittivity, ϵ_r the dielectric constant of the pixel material, A the pixel area and d the active sensor thickness (i.e. the depletion width). For a pixel with an area of 225 $\mu\mathrm{m}^2$ and a depletion width of 0.9 $\mu\mathrm{m}$ this gives a value of 25.89 fF. This value is bigger than the values determined for the SiPMs in this thesis. However, this can be explained because the pixel capacitance is influenced by backplane and inter-pixel contributions [31] and the latter are ignored within this approximation. Additionally, the non-uniform doping of the pixels is also neglected in this formula.
The APD shown in Fig. 2.10 is built on a p-type substrate. For that design the depletion region covers the entire p-region and parts of the n^+-region. Below the p-region a lightly doped p-layer is used that helps increasing the absorption efficiency. At wavelengths of about 400 nm (blue light) the absorption length in silicon is about 0.1 $\mu\mathrm{m}$. Moreover, at wavelengths of about 750 nm (red light) the absorption length is about 8 $\mu\mathrm{m}$ (see Fig. 2.13). With the most upper layers of the devices being in the range of several hundred nm, a lot of photons would just pass through it and be lost for detection. Since most of the absorptions take place in the lightly doped p-layer, this region is called *absorption region* [27].

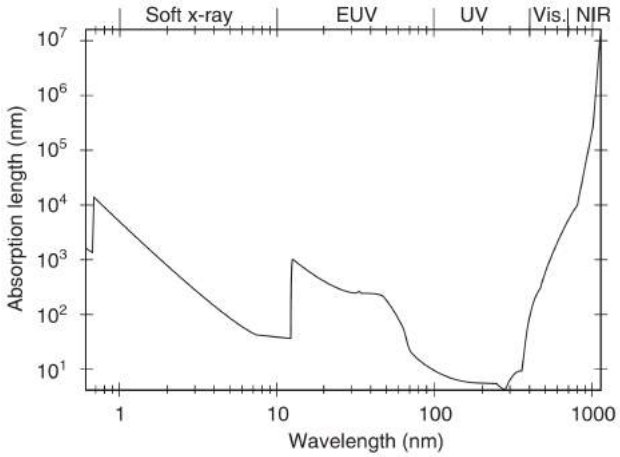

Fig. 2.13: Photon absorption length in silicon as a function of the photon wavelength. In the range of visible photons the absorption length is several $\mu\mathrm{m}$ [32].

Electrons produced in the absorption region will be driven towards and pass the p-n junction, where they start the multiplication process. Of course the creation of new electron-hole pairs via impact ionization can happen along the entire path the electron is taking, but about 95 % of the multiplication process will happen in this highly doped region, that thus is called *multiplication zone*. That the multiplication takes place mainly in this region is due to the fact that the electric field is highest in this region and that the multiplication gain is dependent on the electric field [33]. The remaining area, where much less multiplication takes place, is called *drift region* [21].
It is also possible to invert the doping scheme, i.e. to swap the n- and the p-doped zones. Which design is the right to choose depends on the wavelength of the photons that are

ought to be detected. If photons of blue or ultraviolet light ($\lambda < 475$ nm) should be detected one uses a p-on-n device because those photons will be mainly absorbed close to the surface. They need to be accelerated towards the multiplication zone in the opposite direction than photons of red or even infrared light ($\lambda > 650$ nm), which will in general be absorbed in the bulk of the sensor. For the latter case, an n-on-p device would be the right choice (see Fig. 2.14).

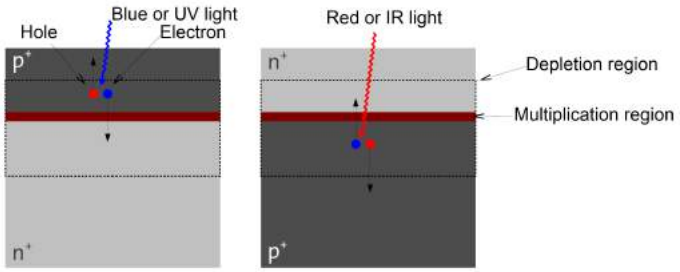

Fig. 2.14: Two different layouts for a SPADs doping profile. The p-on-n design is suited best for the detection of blue or UV light whereas the n-on-p design is most efficient for the detection of red or IR light [27].

2.6 Silicon Photomultipliers

Silicon Photomultipliers (SiPMs) offer a way to combine the advantages of an APD with the ones from a SPAD, namely a signal proportional to the intensity of light i.e. the number of incoming photons, and the ability to detect single photons. In a SiPM multiple SPADs (also called pixels) are connected in parallel to generate a common output. Depending on the producer SiPMs are sometimes also labeled as Multi-Pixel-Photon-Counters (MPPC), Solid State Photomultipliers (SSPM) or Multi-Pixel Avalanche Photodiode (MPAD). In the following such a device will be called SiPM.
Although the name suggests it, SiPMs do not work like vacuum photomultiplier tubes (PMTs). The detector does not multiply photons but electrons from a primary photoelectron generated by a photon interaction. The following section will discuss the working principle and underlying physics of SiPMs.

2.6.1 SiPM Working Principle

In a SiPM a matrix of SPADs is created by connecting hundreds or thousands of pixels in parallel. Fig. 2.15 shows the corresponding equivalent circuit diagram of a SiPM.
Since the SiPMs investigated in the course of this thesis were built by KETEK, the standard design of KETEK SiPMs is shown in Fig. 2.16. They are based on a p-on-n structure with a shallow, highly doped p-region on top and a low n-doped body below. The basic

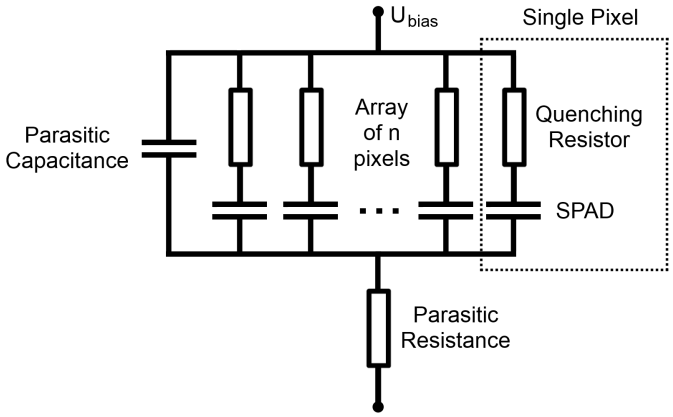

Fig. 2.15: The equivalent circuit diagram of a SiPM. n pixels consisting of a quenching resistor and a SPAD are connected in parallel. Also parasitic contributions from the electric connection are added. Remade from [34] and [5].

working principle of a SiPM is the same as that of a SPAD. Equation (2.8) for calculating the time constant of the pixel recharging is also valid for the SiPM.

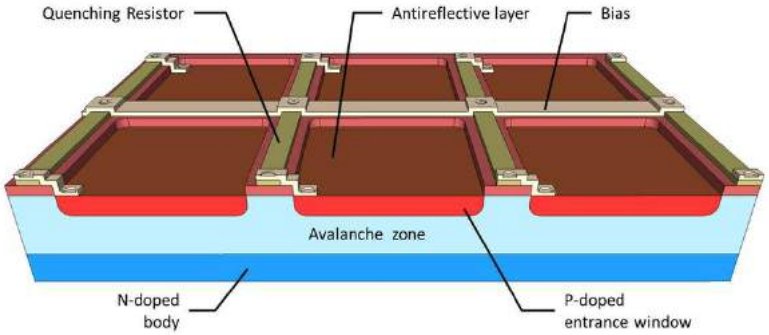

Fig. 2.16: Cross section of a SiPM processed in KETEK standard technology. The SiPM is based on a p-on-n structure [35].

2.6.2 Breakdown Voltage

An important quantity to characterize a SiPM and determine its working point is the breakdown voltage. SiPMs are operated above breakdown and the difference between the breakdown voltage and the operating voltage is called *excess voltage* V_{ex}. Several quantities like the photon detection efficiency, the dark count rate or cross-talk probability are functions of the excess voltage. They will be described in detail in the following chapters.

The breakdown voltage is depending on the doping profile of the p-n junction of the pixels and the temperature. As discussed in chapter 2.4, the doping profile determines the strength and distribution of the electric field. The breakdown voltage can be estimated

using the following equation [21]:

$$V_{bd} \approx \frac{\epsilon_{Si} \cdot E_m^2}{2q_o \cdot N_{eff}} \tag{2.10}$$

Where ϵ_{Si} is the dielectric constant of the material (silicon), E_m the maximal electric field at the junction, q_0 the elementary charge and N_{eff} the doping concentration on the side of the junction with lower doping. The formula holds for simple one-side abrupt junctions. This is the case for the KETEK SiPMs used in the course of this thesis. For such junctions the characteristic of the device is determined by the less-doped side. However, in general the breakdown voltage of a single pixel even with different structure is inverse proportional to the doping concentration [27].
The breakdown voltage is also dependent on the temperature of the device, the reason for this lies in the ionization rate of the charge carriers and the vibrations of the crystal lattice. With rising temperature lattice vibrations will increase and charge carriers will lose more energy due to scattering with the crystal lattice and emitting phonons. This decreases the mean free path (average distance a charge carrier can move without scattering) and the mobility of the charge carriers. The mean free path λ can be approximated by [36]:

$$\lambda \approx \lambda(T_0) \cdot tanh\left(\frac{E_{r,Si}(T_0)}{2k_B \cdot T}\right), \tag{2.11}$$

where $E_{r,Si}$ is the energy of the scattering phonons, $\lambda(T_0)$ and $E_{r,Si}(T_0)$ are the values for λ and $E_{r,Si}$ at $T_0 = 0\,\mathrm{K}$, k_B is the Boltzmann constant and T the temperature.
Due to the smaller mean free path, a higher electric field is needed to accelerate the charge carriers strong enough to cause impact ionizations. To obtain a higher electric field a higher bias voltage is necessary. Consequently, V_{bd} increases with increasing temperature as a result of the lower charge carrier mobility. Fig. 2.17 shows how temperature influences the breakdown voltage in silicon junctions with different doping.

2.6.3 Dark Counts

As already pointed out, SiPMs show a higher dark count rate than PMTs. These dark counts lead to an unwanted amount of false registered events that are not triggered by impinging photons.
A dark count corresponds to a Geiger discharge of a pixel without incoming and detected photons but caused by thermal excitations or tunneling effects. The signals thus created are the same as the ones created by a photon induced discharge and cannot be distinguished from regular photon detections. Like the name suggests these counts may also appear in complete darkness. The rate at which these dark counts appear is called dark count rate (DCR).

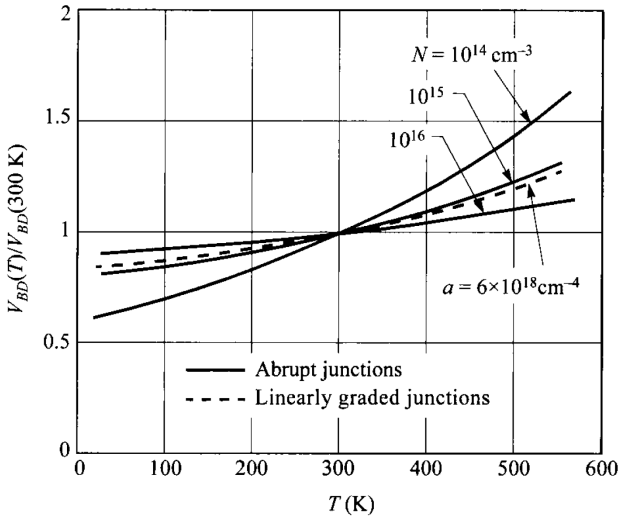

Fig. 2.17: Normalized temperature dependence of the breakdown voltage in silicon for different doping profiles and densities [21].

Since the avalanche triggering probability is a function of the applied excess voltage, the DCR increases with increasing excess voltage [37]. Fig. 2.18 shows the two main processes responsible for the dark counts, both as a direct and an indirect process assisted by intermediate trap levels and the band structure at the p-n junction of a single pixel.

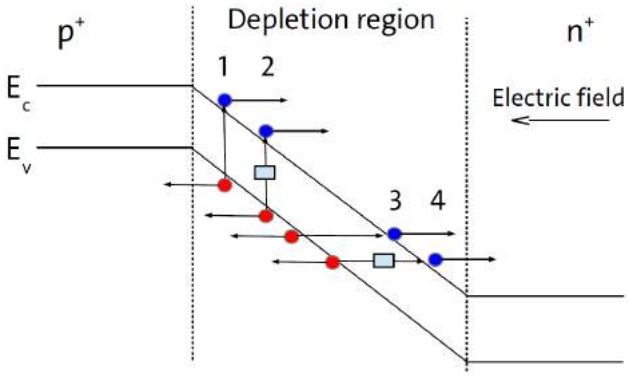

Fig. 2.18: Band structure schematic of a single pixel showing the main sources of dark counts. 1: Direct thermal transition of an electron from the valence band to the conduction band. 2: Trap assisted thermal transition. 3: Direct tunneling effect. 4: Indirect tunneling effect assisted by a trap level [27].

A consequence of the traps assisting the dark count generation is that the DCR per pixel is also a function of the pixel size. Assuming the same production procedure for pixels of different sizes, all of them will have the same density of impurities. It follows that larger pixels will have more impurities in total leading to a higher probability of trap-assisted transitions causing a higher DCR. For instance, KETEK SiPMs typically have a DCR of below 1 MHz/mm^2 [35].

Thermal Generation

At room temperature and for low electric fields at the junction, the main contribution to the dark counts are thermally generated free charge carriers [27].
As silicon is an indirect semiconductor, direct transitions of electrons from the valence to the conduction bands are really rare. However, the probability of transitions is increased by trap levels in the band gap. Those intermediate levels are created by crystal impurities and increase the rate of thermal generation. The Shockley-Read-Hall (SRH) model is used to describe this phenomena and its temperature dependence. The effective SRH rate is given by the following formula [38]:

$$R^{SRH} = \frac{n \cdot p - n_i^2}{\tau_p \cdot (n + n_1) + \tau_n \cdot (p + p_1)} \tag{2.12}$$

The variables n_1 and p_1 are defined by:

$$n_1 = N_C \cdot exp\left(\frac{E_T - E_C}{k_B \cdot T}\right) \tag{2.13}$$

$$p_1 = N_V \cdot exp\left(\frac{-E_T + E_V}{k_B \cdot T}\right) \tag{2.14}$$

n and p denote the charge carrier concentrations, n_i the intrinsic charge carrier density, τ_p and τ_n are the recombination lifetimes of the carriers, E_T is the trap energy level, E_C the energy of the valence band and E_V the energy of the valance band. N_C and N_V are the carriers effective densities of states.
For a trap level with an energy in the middle of the bandgap, the recombination rate reaches its maximum. In addition to the variables n_1 and p_1 also the τ_p and τ_n depend on the temperature. Thus it becomes clear that the temperature is an important factor for the DCR. For temperatures around and above room temperature, when the thermal generation is dominating, the DCR increases by a factor of two for each increase of the temperature by roughly 8 K.

Band-to-Band Tunneling

At temperatures below room temperature or for strong electric fields at the p-n junction, tunneling effects become the main contribution to the dark counts in a reversely biased SiPM [27]. Under these conditions, electrons may tunnel through the band gap and jump from the valence to the conduction band. The probability of this tunneling effect rises with increasing electric field and becomes a major noise source when the electric field reaches values of 10^6 V/cm or even higher [21].
In addition to this, trap levels between the conduction and the valence band can also

boost tunneling effects because they effectively decrease the potential barrier between the two bands.
Fig. 2.19 shows the rate for band-to-band tunneling in silicon and also a comparison of direct tunneling with defect-assisted tunneling. It can be seen that for smaller electric fields the defect-assisted contribution dominates. In the case of strong electric fields, the rate depends on the lattice relaxation energy ϵ_r of the defect and in the case of lower values for ϵ_r the rate is comparable to the rate of direct band-to-band tunneling.

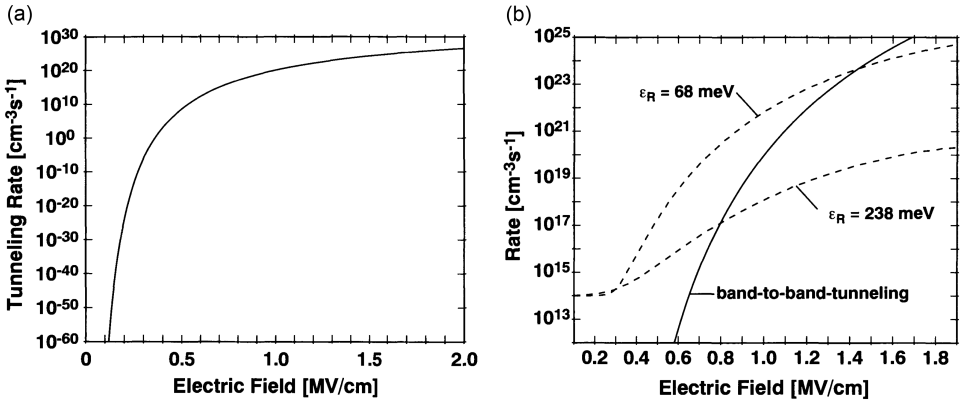

Fig. 2.19: (a) Calculated band-to-band tunneling rate in silicon. (b) Comparison of the band-to-band tunneling rate for direct band-to-band tunneling (continuous line) and defect-assisted tunneling (dashed-lines). In the latter case the rate depends on the lattice relaxation energy ϵ_r of the defect [39].

2.6.4 Cross-Talk

Besides electrical cross-talk that is common in all multi-element arrays and caused by lateral diffusion and drift of charge carriers, SiPMs also show optical cross-talk [1]:
Photons created within a pixel during breakdown can penetrate into neighboring cells and cause further avalanches. This might happen either directly or via reflection at the passivation layer or the border of the bulk (see Fig. 2.20). A possible way to prevent this from happening, is to include a trench between the single pixels, which can also be seen in the figure. This trench is filled with light-absorbing material and stops the additionally created photons from directly entering the next pixel.

Previous research indicated that the additional photons are produced by either Bremsstrahlung with charged impurity centers involved or recombination of free electrons and holes in the avalanche region. Nowadays studies refuted these two processes and introduced direct and phonon-assisted intra-conduction-band transitions as an explanation for the observed emission of hot charge carriers into the avalanche region [1].
In a single avalanche breakdown many infrared photons may be produced (around 10^{-5} photons/electron) which nevertheless will mainly be absorbed in the vicinity of the

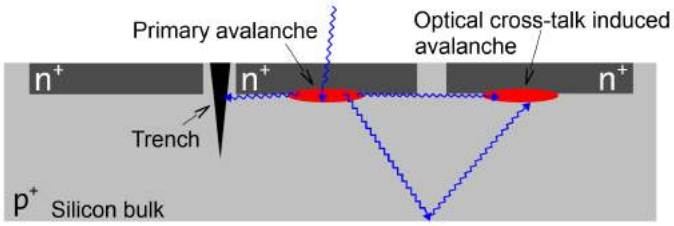

Fig. 2.20: The two possible ways a secondary photon created during an avalanche can take to cause further avalanches: The photon can either propagate directly to the neighboring pixel or be reflected from the backside of the silicon bulk and then enter the neighboring pixel. Adding an opaque trench between neighboring pixels can prevent direct propagations [27].

pixel in which this avalanche was triggered. As a result, the number of excited adjacent pixels due to cross-talk should be rather small [40].
Since the avalanche triggering probability is a function of excess voltage [41], the cross-talk probability is as well depending on the excess voltage. This is due to the fact that a higher excess voltage results in a higher electric field inside the SiPM. As a consequence, emitted photons have a greater chance to cause an additional avalanche. Furthermore, the number of photons emitted in an avalanche increases with the gain, which is also a function of the excess voltage [27].
Additionally to the previously described (prompt) cross-talk, that occurs within the photon time of flight (a few picoseconds [37]) there is a second type of cross-talk, called *delayed cross-talk*. It is caused by absorption in the substrate. A minority carrier generated beneath the p-n junction can diffuse into the active region of a neighboring pixel thus creating a delayed avalanche. This process is delayed with respect to the first pixel firing because of the diffusion involved, as it can be seen in Fig. 2.21. Unlike afterpulses, which are going to be described in the following section, prompt and delayed cross-talk generate a pulse with unit amplitude. However, delayed cross-talk and afterpulses can show similar time constants in the two-digit nanosecond range [37].

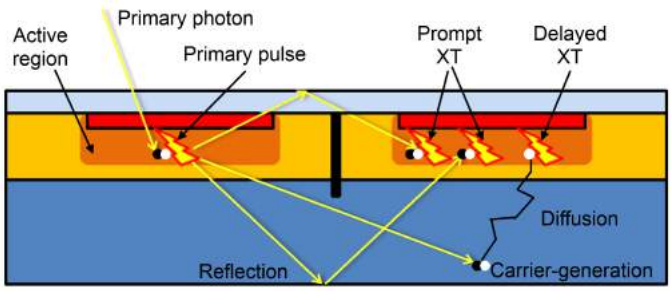

Fig. 2.21: The two different possibilities for cross-talk: prompt and delayed cross-talk. Since the minority carrier diffuses into the active region, the secondary pulse is delayed [37].

2.6.5 Afterpulses

Another effect increasing the amount of false signals in a SiPM is afterpulsing. During an avalanche charge carriers may be trapped in crystal defects inside the pixel. These defects are mostly deep levels (i.e. located close to the middle of the band gap). The captured carriers get released with a time constant ranging from tens of nanoseconds to tens of microseconds and may trigger further avalanches in the same pixel. The exponential release can be described by the following formula [37]:

$$f_{release}(t) = \frac{1}{\tau_{AP}} \cdot exp\left(-\frac{t}{\tau_{AP}}\right) \tag{2.15}$$

Where t denotes the release time and τ_{AP} the release time constant of the trapped carriers. As already mentioned in the previous section, delayed cross-talk that happens in an adjacent pixel creates a pulse of the same amplitude as the original avalanche. This is different for afterpulses, because when the afterpulse happens before the pixel is completely recharged, the resulting signal will be smaller than the original one. How this looks in general is shown in Fig. 2.22. The picture was taken with an oscilloscope and depicts an initial discharge of a SiPM pixel with a certain amplitude followed by a smaller second peak that could origin from an afterpulse.

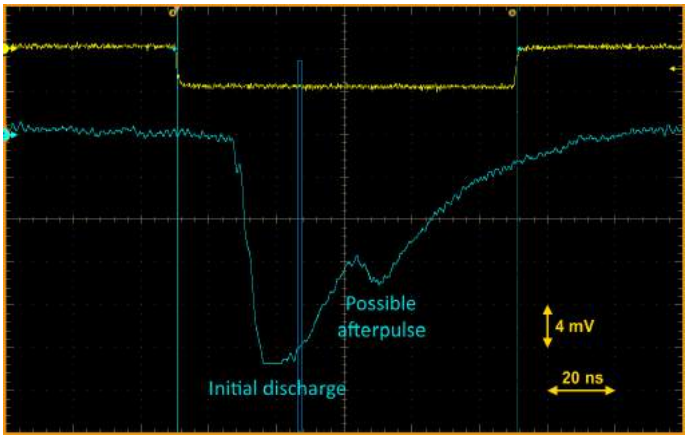

Fig. 2.22: Oscillogram showing the signal of an initial Geiger discharge followed by a second peak with smaller amplitude. This could be an afterpulse caused by a charge carrier that was detrapped before the pixel was completely recharged.

However, the earlier a carrier is released the less probable an afterpulse becomes. There are two parameters that influence the overall probability of afterpulsing.
First, the excess voltage: Traps inside the silicon are sparsely populated and their population increases linearly with the charge that flows during the avalanche pulse which increases with the excess voltage. Moreover, likely to what was written in the section before, the avalanche trigger probability and the gain as well as the amount of created free charge carriers that can be trapped increase with the excess voltage. As a result, in order

to reduce the amount of afterpulses, the SiPM should be operated at low excess voltages [42].
The second important parameter is the temperature: The trap release process is highly dependent on the temperature and becomes much slower at low temperatures. This leads to charge carriers being released later and increases the number of them who can trigger an afterpulse (see equation 2.15).
In addition to this, there is another possible source of afterpulses. When photons created during an avalanche knock off an electron within the silicon substrate they might also cause afterpulses. Because then, one of the charge carriers produced in this way may travel back to the pixel and trigger a second avalanche. However compared, the fraction of the afterpulses created in this way is really small [43].

2.7 Radiation Damages in Silicon and Semiconductor Devices

The goal of this thesis is to analyze the impact of neutron irradiation on the performance of SiPMs. Semiconductor detectors are often used near the target or collision point of accelerator experiments. As a result, they are exposed to high doses of both particle and electromagnetic radiation. In general, radiation can cause two types of damages in a semiconductor detector: *surface damage* and *bulk damage* [44].
Surface damage is responsible for creating traps and fixed positive oxide charges at the Si/SiO_2 interface of a SiPM pixel. These can lead to a higher leakage current. The physical mechanism of the creation of surface damages is the ionizing energy loss (IEL) of charged particles and photons. A possible source of surface damage are X-rays.
Particle irradiation mainly induces bulk damage which is also the main concern for the use of SiPMs in high energy physics [45]. As a consequence, the following chapter will focus on the physics of bulk damages and especially their impact on silicon.
The mechanism behind bulk damage is the non-ionizing energy loss (NIEL) of photons and particles like electrons or neutrons. When colliding with lattice ions, these particles can damage the crystal lattice and cause displacements of atoms [10].

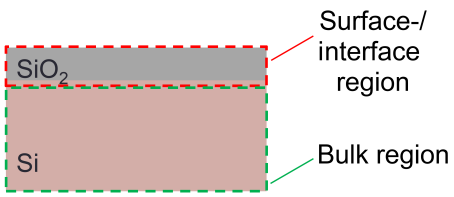

Fig. 2.23: Different regions of a pixel where radiation damaging takes place. The red dashed line indicates the surface/interface region where IEL-damages dominate and the green dashed line indicates the bulk are where NIEL-damages dominate.

2.7.1 Generation of Defects

Not all interactions of neutrons with a silicon lattice will result in defects or displacements. The incoming particles have to have an energy higher than the displacement threshold energy, in order to knock out a single silicon atom from its lattice position. The energy needed to knock a silicon atom out of the lattice with a probability of more than 50% is about 25 eV [44]. The result of such a collision is the creation of a *Frenkel pair*, namely an *interstitial* (I) and a *vacancy* (V). At room temperature, they are both mobile. This is also the reason why a significant amount of these defects is not stable and is undone by recombination. The displaced silicon atom is called *primary knock-on atom* (PKA).

If the PKA is given enough energy through the collision, it can knock out further silicon atoms and form a defect cascade. At the end of the path of the knocked off atoms the density of vacancies and interstitials is very high. As a result a so-called *cluster* is formed. As an example: A PKA with a recoil-energy of $E_R \approx 50$ keV can create up to 1000 Frenkel pairs. In Fig. 2.24 a simulation of the damage done by a PKA with $E_R = 50$ keV is shown. The clusters shown in the picture can reach areas of up to $10 \cdot 200\ \mathrm{nm}^2$ along the path of the PKA.

While the main collision processes for charged particles like electrons, pions or protons are Coulomb-scattering at nuclei, neutrons, which have no charge, scatter elastically or inelastically.

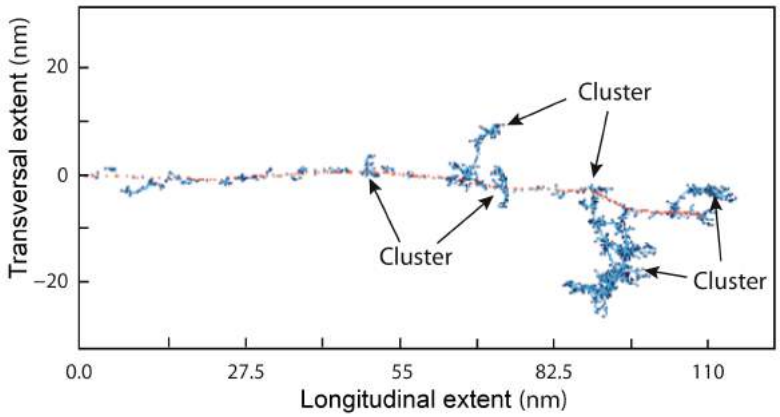

Fig. 2.24: Simulation of the damage done to a crystal lattice induced by a knocked off atom with 50 keV at position (0,0) [44].

As a convention, the bulk damages caused by particle radiation is converted to the damage impact of neutrons with an energy of 1 MeV. The fluence ϕ_{eq}, which denotes the number of particles that passed through 1 cm^2 of a material is then given in n_{eq}/cm^2 (i.e. neutron equivalent). At the Large Hadron Collider (LHC) fluences of $10^{13}\ \mathrm{n_{eq}/cm^2}$ are expected at the outer calorimeter, where SiPMs are installed, after an operation time of

10 years. For the high luminosity upgrade, fluences ten times higher are predicted [44]. In silicon, the NIEL-hypothesis is used to describe the damage done by radiation. The hypothesis states that all the radiation damage caused by particles can be described with point and cluster defects and their rate of occurrence. This also allows the conversion of different irradiations (e.g. neutrons, protons or electrons) and their effects into each other. In Fig. 2.25 the different kinds of defects are depicted.

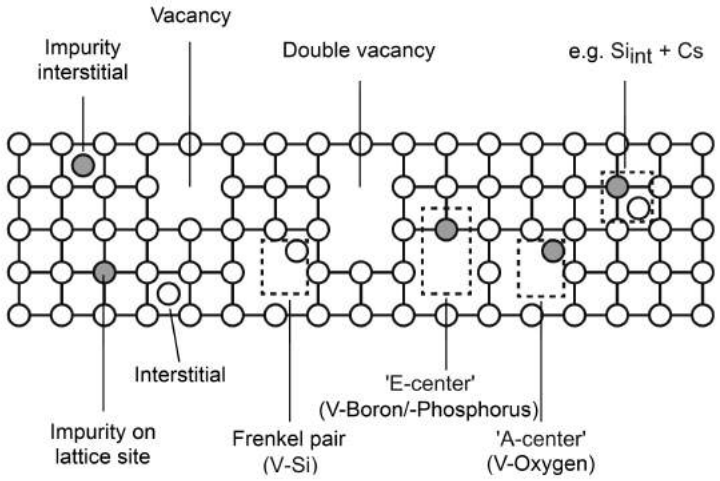

Fig. 2.25: The different kinds of radiation induced bulk damage: Impurities are shown as gray colored circles, more complex defects are depicted with dash-lined rectangles. Si$_{int}$ stands for a silicon atom at an interstitial site [44].

2.7.2 Effect of Radiation Damages in Silicon Photomultipliers

Bulk damage can manifest in new electrically active energy levels in the energy gap of silicon. Free charge carriers can be generated or absorbed due to transitions into the conduction or valence band. Additionally, they can also be trapped in intermediate levels. Fig. 2.26 shows the energy levels of three different kind of defects with respect to the conduction and valence band.

Charged Defects

If the radiation induced defects are charged, they can act as acceptors or donors. This results in a change of the effective doping concentration $N_{eff} = N_D - N_A$, which in return affects the charge of the depletion region. In extreme cases the changing of the effective doping can be drastic enough to cause a type inversion from n- to p-type. Consequently, the voltage needed to cause complete depletion changes. In some SiPM designs a change of the breakdown voltage has been observed due to this [46].
Due to irradiation, original acceptor or donor atoms may be neutralized either because

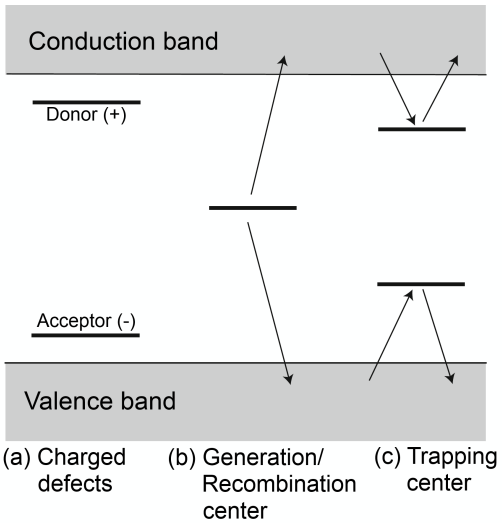

Fig. 2.26: Energy levels of radiation induced bulk damage and their relative energies in the bandgap of silicon [44].

they are removed from the lattice or because they react with mobile defects and become electrically neutral. If charged defects energetically lie in the middle of the band gap (deep level defects), they contribute to charge generation and increase the leakage current.

Generation/Recombination Centers

Defects (charged and uncharged) with energy levels in the middle of the bandgap act as generation or recombination centers. They facilitate thermal generation of electron-hole pairs via intermediate energy levels. Also electrons and holes from the corresponding bands can use these energy levels to recombine. The probability for defect assisted generation/recombination is highest for defects in the middle of the bandgap. Energy levels closer to one of the bands will have less influence.
The effect of generation/recombination centers is a change in the charge carrier density as well as an increase of the leakage current. This increase is proportional to the fluence:

$$\Delta I_{leak} = \alpha \cdot \phi_{eq} \cdot V \tag{2.16}$$

Where α is the damage rate, ϕ_{eq} the neutron equivalent fluence and V, in case of a SiPM, the volume of a pixel. Additionally, the increasing leakage current can also heat up the detector, hence influencing its performance.

Trapping Centers

As the name implies, trapping centers are able to trap electrons or holes and release them after a certain amount of time. This influences the mean free path of charge carriers and can lead to a decrease of the signal. This corresponds to a decrease of the *charge collection efficiency* (CCE). The CCE is the ratio between the detected charge Q_{det} and the charge caused by ionization Q_{ion} [44].

$$CCE = \frac{Q_{det}}{Q_{ion}} \tag{2.17}$$

However, in silicon even at high irradiation fluences up to 10^{15} n_{eq}/cm^2 the CCE barely changes due to increased trapping.
There are studies whether an accretion of trapping centers in a SiPM pixel might also increase the probability of afterpulses or delayed cross-talk, since both mechanism rely on the presence of trap levels. However, the increased dark current after irradiation causes serious problems in disentangling the afterpulse contribution from the noise [47].

2.7.3 Annealing of Defects

As already mentioned, a lot of defects are mobile at room temperature and may recombine. So heating up an irradiated detector can repair the damage done. This process is called *annealing* [44].
Depending on the defect, different temperatures are needed for the annealing. Simple defects like single vacancies or interstitials are removed much easier than more complex defects like double vacancies or an A-center. The first are mobile at 20 °C and a vacancy is very likely neutralized by another impurity or an interstitial. The latter defects become mobile at temperatures between 250 °C and 300 °C [45]. If the annealing temperature is higher than the binding energy of the defects, they can be separated into their components and easily repaired. However, annealing at such high temperatures can also have a negative impact, because the defects can combine into more complex defects that have a higher thermal stability. This effect is called *reverse annealing*.
When directly investigating the effects of irradiation on detectors, it is essential to store the detectors in a cold environment. For example, the detectors investigated for this thesis were stored in a fridge at -20 °C between the measurements.

2.7.4 Methods to Improve Radiation Hardness

The goal of studying the impact of neutron irradiation on SiPMs is not only to investigate the physical effects but also to improve the radiation hardness of the detectors. There are

already some established methods to do so:

- High doping concentration is beneficial, since it lowers the relative change in the effective doping and can also delay the type inversion.

- It is advisable to use guard rings for the pixels. After neutron irradiation, a higher voltage is needed for complete depletion and a guard ring supports the potential decrease towards the edge of the pixel.

- Decreasing the pixel size. Assuming the same effective doping, smaller pixels have a smaller capacitance and thus a faster recharge time. After irradiation the DCR is expected to go up and if the pixels have a faster recharge time, dark counts disable the pixels for a shorter time.

- Enriching the silicon with oxygen. Irradiating oxygen enriched silicon leads to the creation and complex interaction of acceptor and donor like defects that cancel each other out. Furthermore, instead of deep levels more shallow intermediate levels are introduced that have a smaller probability to cause leakage current [44]

- Operating the detector at low temperatures. This reduces the dark current and increases the signal to noise ratio. Also it freezes reverse annealing processes that can outbalance the positive effects of annealing [12].

3 Characterization Methods

In this chapter, the measurements used to characterize the SiPMs are described. Three types of measurements were performed for this purpose. Their setup, the experimental conditions and the corresponding analysis methods used to extract information about the SiPMs and their performance are explained.
The chapter begins with general information about the KETEK SiPMs studied for this thesis.
Section 2.2 is about current-voltage measurements and section 2.3 about capacitance-voltage-frequency measurements. These measurements are used to determine technical SiPM parameters like the quenching resistance, pixel capacitance and breakdown voltage. Since both kinds of measurements were done using the same setup, the setup itself are only be explained in section 2.2.
In section 2.4 the charge-voltage measurements are explained. From these measurements it is possible to determine performance characteristics of the SiPMs, namely the gain, the cross-talk and afterpulse probability and the dark count rate.

3.1 KETEK SiPMs

In the course of this thesis, 20 silicon photomultipliers produced by KETEK are investigated. The SiPMs are divided into two groups of ten, with each group being built on a different silicon wafer, named wafer 1 (W1) and wafer 6 (W6). Additionally, for each group a reference sample is chosen, which has not been irradiated. The reference samples are W1-B3-S1 and W6-B3-S1. All SiPMs are designed and produced in the same way, with the only difference being that the W6 SiPMs have an additional epitaxial layer on top. For time reasons, the investigation focuses on the W1 SiPMs. Nevertheless, both were measured before irradiation and the irradiated W6 samples are planned to be measured in the future as well.
Fig. 3.1 is a schematic of the investigated KETEK structures. As it can be seen there are several SiPMs mounted on them. In total there are six different circular SiPMs with a diameter of 1 mm and eight square SiPMs with a side length of 300 μm. The circular SiPMs consist of 4384 pixels and the square ones of 400. In both cases a single pixel has an area of 15x15 $\mu\mathrm{m}^2$. The difference between the individual designs/versions (indicated with V) are for example the use of a guard ring or a different quenching resistor. For this thesis the circular SiPM MP15V9 of each structure was investigated.
The nomenclature for the different samples is the following: Each sample has its name given based on the wafer Wx it was made of, the batch Bx it belongs to (different batches

correspond to different dates of arrival at the institute) and a sample number Sx. The fifth sample of the second batch from wafer one for example is labeled: W1-B2-S5.

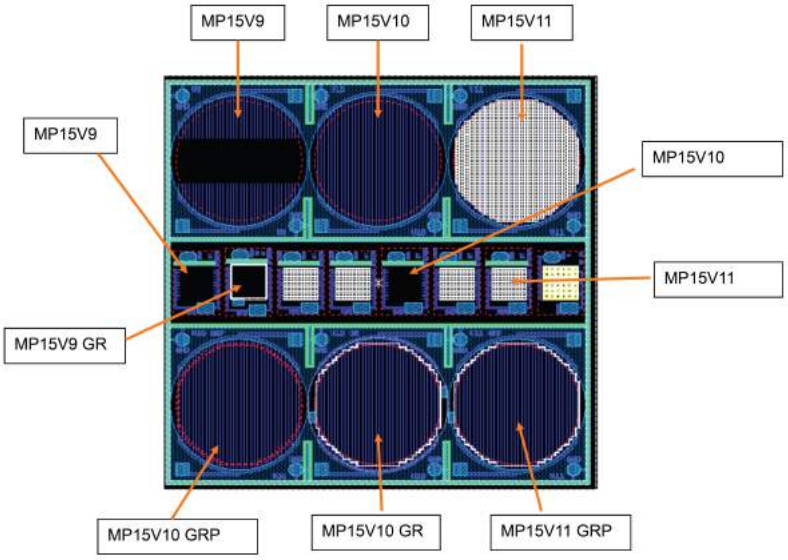

Fig. 3.1: Schematic of the KETEK structures investigated. On each sample six round and eight squared SiPMs with different designs are mounted. V stands for the version of the different designs. The labels GR and GRP indicate that the corresponding SiPM has a guard ring incorporated.

For measuring purposes the structures were glued onto ceramic substrates with gold contacts on them. A bonding machine was then used to connect the single SiPMs electric connections with the gold contacts via aluminum wire bonds. This simplified the IV/CV-f measurements, because without the bonds a microscope would have been needed to contact the SiPM electric connections directly with needles. Furthermore, this would not have been possible for the charge-voltage measurements because the climate chamber used did not provide enough space for a microscope.
Between the measurements the SiPMs were stored in little plastic containers. In order to prevent annealing after the neutron irradiation, the SiPMs were then stored in a fridge at -20 °C and their duration outside of the fridge was protocoled. One of the KETEK devices, the ceramic substrate it is glued on and the plastic container can all be seen in Fig. 3.2.

In Fig. 3.3 a picture of one of the investigated SiPMs taken with a laser microscope as well as a zoomed in picture of several pixels can be seen. The same structures as in Fig. 2.16 are visible, namely the quenching resistor, the entrance window and the biasing line made of aluminum. The quenching resistor is made of a doped polysilicon strip line that is embedded in an insulating matrix [35]. The black shadows in the left picture are the aluminum wire bonds used to contact the SiPM. The upper one is going to the ground contact, the lower one to the biasing contact. In the upper part of the picture, there is some blurring observable. This is caused by the image reconstruction software of

Fig. 3.2: One of the investigated KETEK devices glued onto a ceramic and contacted via aluminum wire bonds to its gold contacts. It is stored inside a little plastic container to protect it from environmental influences like dust or humidity.

the laser microscope. The picture is composed of several single images put together and at the transition of two images the software encountered some problems.

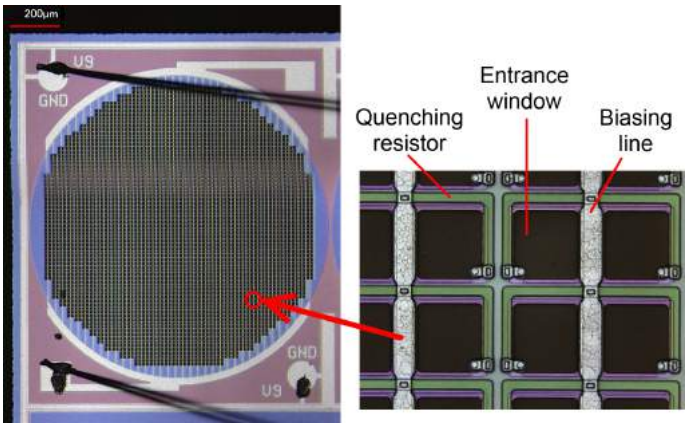

Fig. 3.3: Laser microscope pictures of a KETEK SiPM investigated for this thesis. Left: overview of the whole sensor. Right: zoomed-in picture of a few pixels.

Fig. 3.4 shows the cross-section of a single pixel from a KETEK SiPM as well as the process of a photon getting absorbed and creating an ehp. It can also be seen that each pixel is connected to a quenching resistor to stop the avalanche process.

3.2 Current-Voltage Measurements

A method often applied to characterize SiPMs are current-voltage (IV) measurements. They are done by applying a voltage to the SiPM and measure the resulting current. For the measurements done for this thesis, the applied voltage ranged from 2 V in forward direction to 40 V or 45 V respectively, in reverse direction.

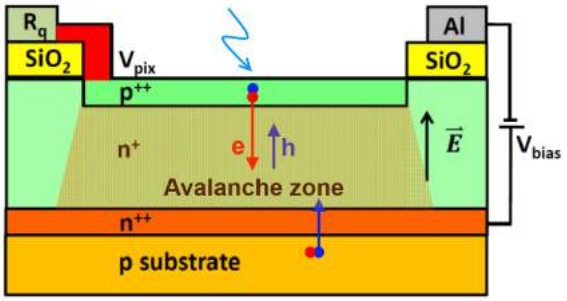

Fig. 3.4: Schematic cross-section of a single pixel of the investigated KETEK SiPMs. Also depicted is the avalanche zone and the creation of electron-hole pairs caused by incoming photons [48].

To investigate if the measurements are stable or the SiPMs show hysteresis features, each measurement is done in two steps: One time ramping the voltage up from 2 V in forward direction to 40 V in reverse direction. Afterwards ramping the voltage down from 40 V in reverse bias to 2 V in forward bias.
The highest values for the reverse biasing correspond to an excess voltage of about 12 V at room temperature. The measured currents range from a few hundred fA at low reverse voltages to 10 mA at the highest forward and highest reverse voltages in the case of higher irradiation fluences. Theoretically, even higher currents and in the case of low temperature measurements also lower currents could occur. However, the setups voltage source has an internal current limit that prevents higher currents and additionally, accuracy of the current meters is not high enough to be able to reliably measure currents below a few hundred fA.

3.2.1 Measurement Setup

The setup for IV as well as CV-f measurements can be seen in Fig. 3.5. The SiPM is placed in a light tight probe station, inside which there is a temperature sensor as well as a humidity sensor. Moreover, an LED is placed inside the probe station to allow illumination of the SiPMs. The LED, that emits light with a wavelength of 470 nm, is driven with an Agilent E3631A DC power supply [49] that permits, in varying the supply voltage, to control the brightness of the LED.
However, the setup does not include any possibility to measure the absolute intensity of the LED light. Additionally, there is no way to fix the position of the SiPMs in the setup and also before irradiation they were not always glued on the same spot on the ceramics. As a result, the position of the SiPM relative to the LED is different for every measurement and the LED intensities hav to be defined differently. Two definitions are used: Low light intensity and high light intensity. In the first case, an excess voltage of 4 V (which corresponds to 31 V for wafer 1 and 39 V for wafer 6 at 20 ° C) is applied and the supply

voltage for the LED is set so that the ratio of the currents without/with LED illumination is 1:10. In the second case, the LEDs voltage is adjusted to a value so that the ratio of 1:10 is achieved at a voltage of 10 V in reverse.
The temperature and the humidity sensors of the setup are connected to the DAQ computer on which a LabVIEW program is installed, in order to control the measurements and store the data taken. To ensure a stable temperature and a dry atmosphere, the setup features a dry-air supply system and cooling system from ATT [50]. The decoupling circuit provides a switch to allow selecting between IV and CV-f measurements without having to disconnect the SiPM or one of the instruments. Nevertheless, to reduce the noise from additional connections in case of the IV measurements, this circuit is not used and instead the cables are connected directly to the current meter. This mainly improved the measurement of low current values. The current meter with included voltage source is a Keithley 6517B [51] and an Agilent E4980A precision LCR meter [52] serves for measuring the capacitance and conductivity for different frequencies.

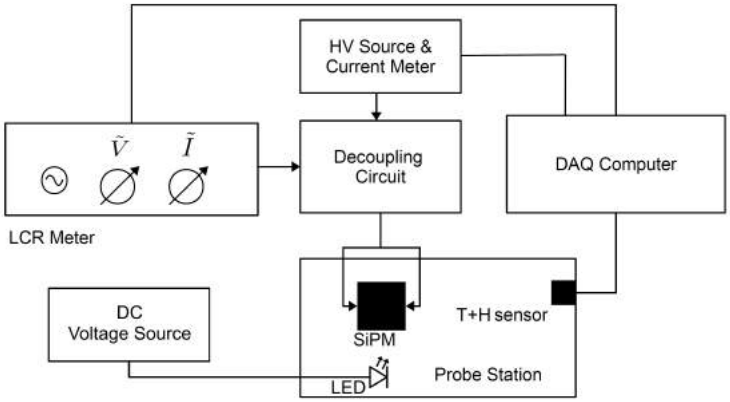

Fig. 3.5: Schematics of the setup used for IV and CV-f measurements [27].

3.2.2 Forward Bias Characteristic

If a negative voltage is applied to the n-doped region of a SiPM and a positive voltage to the p-doped region the detector is forward biased. The forward IV curve can be described using the following formula [26]:

$$I \simeq I_{d0} \cdot (e^{\frac{q_0 \cdot V_d}{k_B \cdot T}} - 1) + I_{r0} \cdot (e^{\frac{q_0 \cdot V_d}{2k_B \cdot T}} - 1) \tag{3.1}$$

Where q_0 is the elementary charge, k_B the Boltzmann constant, T the temperature at which the measurement was taken, I_{d0} and I_{r0} are the constants characterizing the diffusion and the recombination current, and V_d is the voltage drop over the diode:

$$V_d = V - R_s \cdot I = V - (\frac{R_q}{N_{pix}}) \cdot I \tag{3.2}$$

With V as the voltage applied to the SiPM, R_s the series resistance of the SiPM, N_{pix} the number of pixels and R_q as the quenching resistance. As it can be seen, the quenching resistance can be determined using the formula:

$$R_q = R_s \cdot N_{pix} \tag{3.3}$$

Fig. 3.6 shows the forward part of an IV curve. The IV measurement was taken at room temperature with a SiPM before neutron irradiation, with three different light settings. What stands out is that all three curves lie on top of each other. This is not surprising, since a forward biased SiPM does not work as a light detector. Hence, illuminating it does not change the shape of the curves. Within the measurement uncertainties the three measurements are exactly the same.

Determination of the Quenching Resistance

Looking at Fig. 3.6, one can see that for voltages below 0.8 V the SiPM exhibits a non-linear behavior. This can be explained with equations (3.1) and (3.2):
Assuming that:

$$I = I_0 \cdot (e^{\alpha \cdot V_d} - 1) \approx I_0 \cdot e^{\alpha \cdot V_d}\,, \tag{3.4}$$

inserting $V_d = V - R \cdot I$ and rewriting the equation gives:

$$V(I) = R \cdot I + \frac{1}{\alpha} \cdot \ln \frac{I}{I_0} \quad with\ \alpha = \frac{q_o}{k_B \cdot T} \tag{3.5}$$

Below 0.8 V, there is a strong influence of the non-linear part $\frac{1}{\alpha} \cdot \ln \frac{I}{I_0}$. For higher voltages, the linear part $R \cdot I$ begins to dominate and the SiPM behaves similar to a resistor. In this region the diode behavior can be approximated by:

$$V \simeq V_d + I \cdot R_s \tag{3.6}$$

As a result, it is possible to determine the series resistance R_s from the inverse slope of the linear range. Therefore, knowing the number of pixels, the quenching resistance can be calculated using equation (3.3). This calculation nevertheless does not give the exact result, since the inverse slope is not a constant, but decreases with increasing voltage. This can be seen in Fig. 3.7, where the inverse slope is plotted as a function of the forward voltage. The inverse slope is not constant and has a slight tendency to go to lower values for higher voltages. The reason for this can be seen, when the derivative of equation (3.5) with respect to the current is taken:

$$\frac{\mathrm{d}V}{\mathrm{d}I} = R + \frac{k_b \cdot T}{q_0} \cdot \frac{1}{I} \tag{3.7}$$

The decrease originates from the rear part of the equation. For higher voltages, which corresponds to higher currents, the influence of this part will decrease but it still changes the slope of the curve.

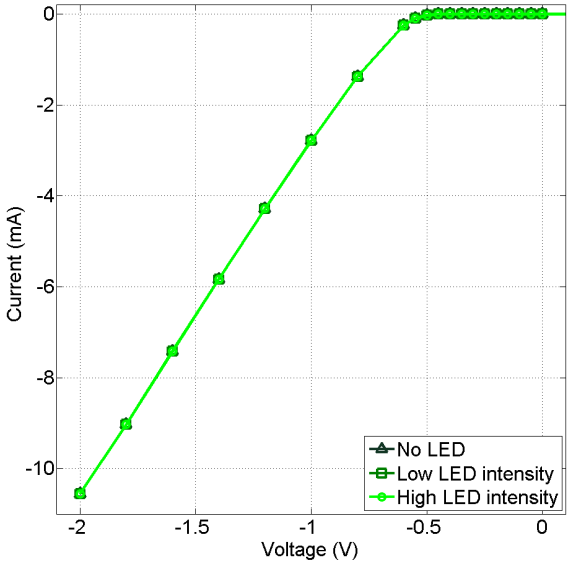

Fig. 3.6: The forward biased range of an IV measurement for a SiPM. The three curves are all from the same unirradiated SiPM and have been taken with different light settings.

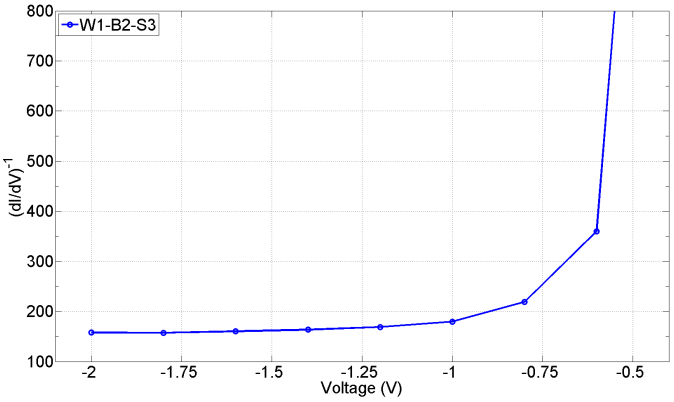

Fig. 3.7: The inverse slope of the forward biased range of an IV measurement. For higher voltages the values show a decreasing tendency.

3.2.3 Reverse Bias Characteristic

If the polarity of the voltages applied to the SiPM is switched, that is to say, a positive voltage is applied to the n-doped region and a negative voltage to the p-doped region, the SiPM is reverse biased.
The reverse biased range of the measurements is plotted in Fig. 3.8. In the case of reverse biasing, the different curves for the light settings do not lie on top of each other. Since

the SiPM now acts as a light detector, the curves with LED illumination show a higher current. Furthermore, a higher light intensity results in more photons being emitted by the LED, more photons reaching the SiPM and consequently, in more pixels experiencing an avalanche breakdown. As a result the IV curve of the higher LED intensity reaches higher current values than the one with low LED intensity.

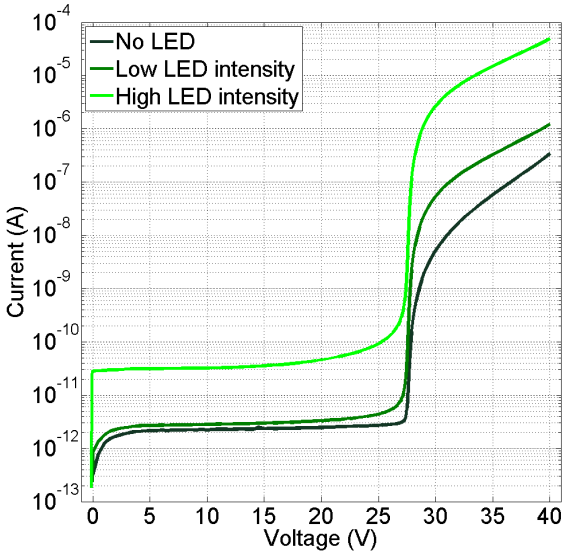

Fig. 3.8: The reverse biased range of an IV measurement for a SiPM with different LED settings, showing the partially depleted, the fully depleted and the breakdown range.

Independent of the light setting chosen, the reverse bias curve can be divided into three different ranges: the partially depleted, the fully depleted and the breakdown region.
In the low voltage range, the depletion zone extends with increasing voltage, resulting in an increase in the amount of electron-hole pairs that contribute to the generation current. Therefore, the total current rises too. For the low LED intensity and the measurement without LED, the increase of the current has a non-steady slope until approximately 5 V, corresponding to the extension of the depletion zone.
At voltages above 5 V the IV curves show a more flat shape. This is an indicator that the SiPM pixels are fully depleted and that the volume of the depletion zone does not increase anymore. However, above this value the current still rises with increasing voltage. This is caused by an increase in surface currents and also at this voltages the creation of additional electron-hole pairs due to impact ionization without causing avalanche breakdowns is already possible.
As soon as the electric field is strong enough to accelerate charge carriers in a way to create avalanche breakdowns, we see a steep rise in current. Over a range of a few Volts the current exceeds multiple orders of magnitude going from picoampere to nanoampere and reaching microampere if the voltage is ramped up to values of 12 V excess voltage[1].

[1] In section 4.3.1, the existence of two excess voltages is discussed. In the case of IV measurements the value

When no light is arriving at the SiPM surface, the electron-hole pairs causing the breakdown are created either by thermal excitation or field induced tunneling (see section 2.3). From the sharp rise at the breakdown of the measurement without LED, it is possible to deduce, that only a fraction of the dark current's electron-hole pairs pass the multiplication zone. In other words, the main contribution are surface currents that do not get amplified before breakdown [48].
However, if the LED is turned on during the measurement, the curves show a less abrupt rise at the breakdown. From this observation, one can assume, that the main contribution to the current comes from electron-hole pairs created by the photoelectric effect in the multiplication zone. A possibility to make this difference even clearer, is to subtract the values of the dark current measurements from the values of the measurements with LED illumination. This has been done in Fig. 3.9 where the difference in the rise before breakdown is clearly visible. What is also visible in Fig. 3.9 is that above breakdown, the dark current curve is steeper than the two other curves. This indicates that the Geiger discharge probability for the dark current increases faster than for the LED photons [53]. This additional contribution in the case of the dark current originates from electron-hole pairs outside the amplification region that reach the amplification region and then cause an avalanche breakdown.
Additionally, the two curves from the LED measurements are parallel at the region of the breakdown and above, which shows that the efficiency of the SiPM to detect light is not a function of the light intensity and that the underlying mechanisms do not differ.

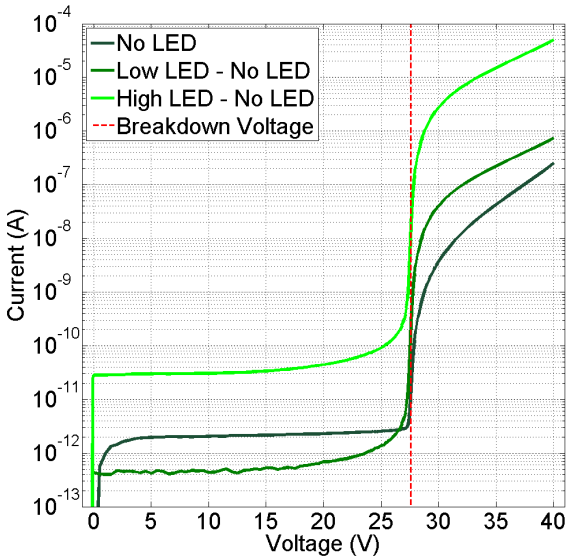

Fig. 3.9: The reverse biased range of an IV measurement for a SiPM with different LED settings. The dark current has been subtracted from the measurements with LED. The breakdown voltage is indicated with the red dashed line

of V_{bd}^{IV} is used as reference. In the case of QDC measurements the value of V_{bd}^{G} is considered.

Determination of the Breakdown Voltage

The breakdown voltage is an important characteristic of SiPMs because they are usually operated at a certain excess voltage. In order to apply the right excess voltage, the breakdown voltage has to be known.
In [47] and [54] a method to determine the breakdown voltage has been introduced: the *inverse logarithmic derivative* (ILD) of the SiPMs current. It can be calculated the following way:

$$ILD(V) = \left(\frac{\mathrm{d}\ln[I(V)]}{\mathrm{d}V}\right)^{-1} = \left[\frac{1}{I}\cdot\frac{\mathrm{d}I(V)}{\mathrm{d}V}\right]^{-1} \tag{3.8}$$

The usefulness of this method comes from the fact that if the SiPM current depends on a constant A, like for example the number of incoming photons N_{Ph} as well as further voltage dependent factors, the constant just cancels out.

$$I(V) = A\cdot(V-V_0)^n \rightarrow ILD = (V-V_0)/n \tag{3.9}$$

The current of a SiPM above breakdown is the product of N_{Ph}, the SiPMs gain G, its photon detection efficiency PDE and a correction factor XT for the cross-talk and afterpulsing. Furthermore, since all these parameter depend on the excess voltage $V - V_{bd}$, the current is also proportional to the excess voltage.

$$I = N_{Ph}\cdot G\cdot PDE\cdot(1+XT) \propto (V-V_{bd})^n \tag{3.10}$$

Where the factor n is related to the gain, PDE and cross-talk voltage dependence. In particular, the gain is proportional to the excess voltage and the pixel capacitance C_{pix}.

$$G \propto C_{pix}\cdot(V-V_{bd})^1 \tag{3.11}$$

It follows:

$$\text{for}\quad I\propto(V-V_{bd})^n \rightarrow ILD(V) = \frac{V-V_{bd}}{n} \tag{3.12}$$

Equation (3.12) can be used to determine the breakdown voltage by simply applying a linear fit. The linear fit can be applied either for $\mathrm{V} > \mathrm{V_{bd}}$ or for $\mathrm{V} < \mathrm{V_{bd}}$ which then results in $\mathrm{n} > 0$ or $\mathrm{n} < 0$ respectively. On top of this there are additional possibilities to extract the breakdown voltage from the ILD:
One can fit a parabola $(V-V_{bd})^2$ through the minimum of the ILD curve in the breakdown region.
Furthermore, the fitting range can be extended to a higher voltage range. For higher voltage the ILD shows a parabolic shape and can be described by:

$$ILD(V) = \frac{V-V_{bd}}{n} + b\cdot(V-V_{bd})^2 \tag{3.13}$$

Fitting this formula to the ILD above breakdown allows to extract the breakdown voltage.
All of these methods have been previously studied and give good results for non-irradiated SiPMs [48]. Also it was proven that the best results were obtained using the ILD of the measurements with the LED turned on and subtracting the dark current, because they are more stable.
Figures 3.10 to 3.12 show the ILD as a function of voltage for a non-irradiated SiPM with different LED settings as well as the single fitting procedures and their ranges used to extract the breakdown voltage. The jump of the current that appears at 30 V is a feature of the voltage source switching ranges. In Fig. 3.10 it can be seen that the ILD for the LED measurements lie on top of each other if the dark current is subtracted. This corresponds to the IV curves for the different light settings being parallel to each other and that the detection mechanisms are independent of the light intensity.

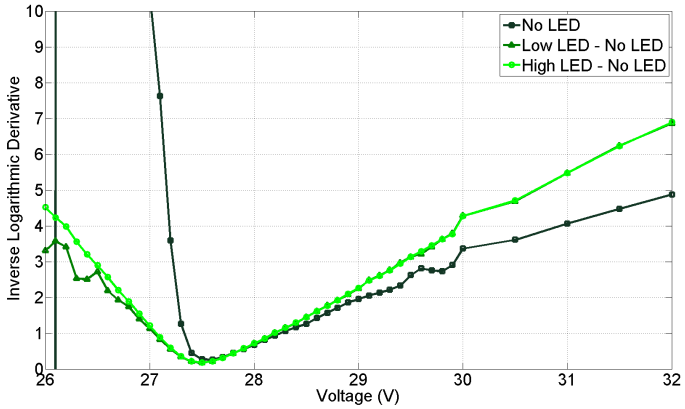

Fig. 3.10: The inverse logarithmic derivative in the breakdown region of a SiPM measured with different light settings.

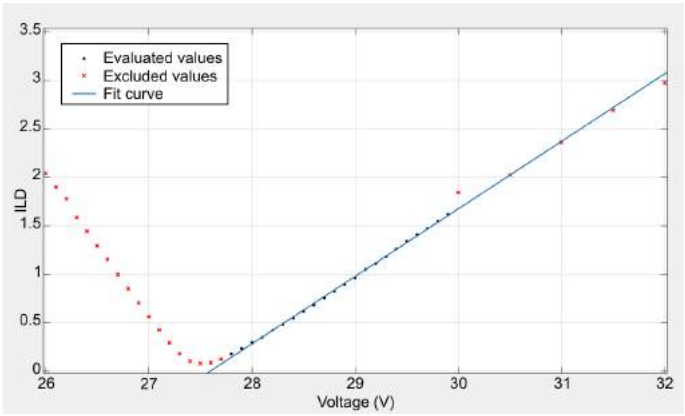

Fig. 3.11: The inverse logarithmic derivative in the breakdown region as a function of voltage. The blue line shows the linear fit according to equation (3.12), the black points the values used for the fit (27.8 V to 29.9 V) and the red crosses the values excluded for the fit.

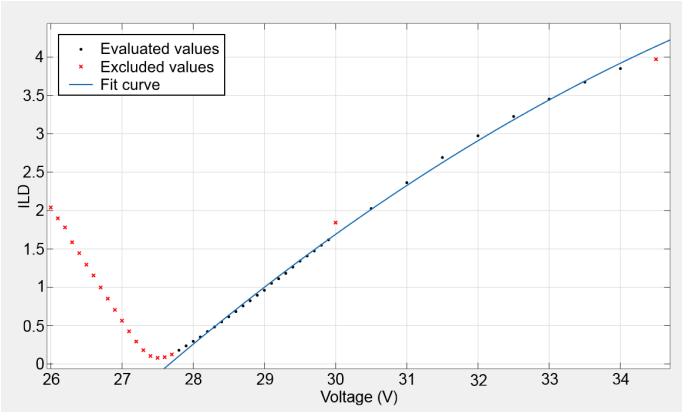

Fig. 3.12: The inverse logarithmic derivative in the breakdown region as a function of voltage. The blue line shows the quadratic fit according to equation (3.13), that covers a wider range of measurement values compared to the linear fit (27.8 V to 34 V).

Evaluating the Goodness of the Fit

The fits and the analysis of the CV-f and IV curves presented in this thesis are done using MATLAB. To evaluate the goodness of the fit and to choose the proper fitting range, the in-built evaluation functions of the MATLAB curve fitting tool are used. This tool provides four parameters to judge the proper use of the fit [55]:

The Sum of Squares Due to Error (SSE)

The SSE measures the total deviation of the fit values $\hat{y}_i$ to the data points y_i. It is also called the summed square of residuals and can be calculated by:

$$SSE = \sum_{i=1}^{n} w_i \cdot (y_i - \hat{y}_i)^2 \,, \tag{3.14}$$

where w_i are weighting factors. A value of the SSE close to 0 indicates that the random error component is small and that the fit provides a good description of the data.

R-Square

R-square measures how successful the fit is in explaining the variation of the data. It can have values between 0 and 1, where a value close to 1 indicates that the fit gives a good description of the variation. A value of 0.9 for example means that the fit explains 90 % of the total variation in the data about the average $\bar{y}$. R-square (R^2) can be calculated using the following formula:

$$R^2 = \frac{SSR}{SST} = 1 - \frac{SSE}{SST} \,, \tag{3.15}$$

where SSR is the sum of squares of the regression and SST is the total sum of squares.

They are given by:

$$SSR = \sum_{i=1}^{n} w_i \cdot (\hat{y}_i - \bar{y})^2 \tag{3.16}$$

$$SST = \sum_{i=1}^{n} w_i \cdot (y_i - \bar{y})^2 \tag{3.17}$$

A drawback of the R-square is that increasing the number of fitted coefficients in the model will increase R-square, although the fit may not improve. In order to avoid this, the adjusted R-square is introduced.

Adjusted R-Square

The adjusted R-square uses the R-square statistics but adjusts them, based on the residual degree of freedom. The residual degree of freedom ν is given by the number n of data points minus the number m of fitted coefficients. $\nu = n - m$ thus corresponds to the number of independent pieces of information including the n data points that are required to calculate the sum of squares. The adjusted R-square can be calculated using:

$$\mathrm{R}^2_{\mathrm{ad}} = 1 - \frac{SSE(n-1)}{SST(\nu)}\,, \tag{3.18}$$

The adjusted R-square can take on any value less than or equal to 1, with a value close to 1 indicating a good fit. Negative values appear, if the fit model contains terms that do not help to predict the data.

Root Mean Squared Error (RMSE)

The root means squared error is an estimate of the standard deviation of the random component in the data. It is given by:

$$RMSE = \sqrt{MSE} = \sqrt{\frac{SSE}{\nu}}\,, \tag{3.19}$$

where MSE is the mean square error. A value close to 0 indicates that the fit gives a good prediction of the data.

Example

The quadratic fit in Fig. 3.12 gives the following values:
$V_{bd} = 27.59 \pm 0.05\ V$, $b = -0.02643 \pm 0,00485$, $n = 1.252 \pm 0.046$.
The goodness of the fit is evaluated as the following:
$SSE = 0.03556$, $R^2 = 0.999$, $R^2_{ad} = 0.9989$, $RMSE = 0.03629$.

The linear fit in Fig. 3.11 provides the following results:
$V_{bd} = 27.50 \pm 0.03\ V$, $n = 1.419 \pm 0.021$.
The goodness of the fit is evaluated as the following:
$SSE = 0.004174$, $R^2 = 0.9991$, $R^2_{ad} = 0.999$, $RMSE = 0.01445$.

The method of the parabola minimum for the same device results in the following values: $V_{bd} = 27.41 \pm 0.07$, $SSE = 0.0001197$, $R^2 = 0.9062$, $R^2_{ad} = 0.8593$, $RMSE = 0.007737$. It can be seen that the SSE and the $RMSE$ are better than those of the other fits, but on the other hand the values for R^2 and the R^2_{ad} are not as good.

The optimal fitting range is determined from the curves before neutron irradiation. After irradiation the same range is used but extreme outliers are excluded. Varying the points used to fit the ILD mostly led to a deterioration of the goodness of the fit.

3.3 Capacitance-Voltage-Frequency Measurements

Another method to investigate SiPMs or semiconductor devices is taking capacitance-voltage-frequency measurements. The measurement procedure is similar to measuring IV curves, which also manifests in the fact that IV and CV-f measurements can be done using the same setup (see Fig. 3.5). Like for IV measurements a DC voltage is applied to the SiPM and the resulting current is measured. However, the difference is that the measurements are only done with reverse biasing and that in addition to the DC voltage, an AC voltage of 500 mV peak-to-peak with a varying frequency f is applied. In total 25 different frequencies are applied for each voltage step, ranging from 100 Hz to 2 MHz. Since the measured current is an alternating current, it has a phase shift with respect to the voltage, that is measured too. To be more precise, the installed LCR meter measures the complex impedance $|Z|e^{i\theta}$ and calculates the capacitance C_p and the conductance G_p of the circuit using the following formula:

$$Y = \frac{1}{Z} = \frac{\tilde{I}}{\tilde{V}} = G_p + j\omega C_p \tag{3.20}$$

The index p stands for parallel, because the formula corresponds to a resistor in parallel to a capacitor. Above breakdown, an AC voltage would cause large variations in the measured current, as a consequence only voltages below breakdown are applied. The DC voltage is increased in steps of 500 mV from 0 V to 27 V in the case of wafer 1 SiPMs.

3.3.1 CV-f Curve Characteristics

As already mentioned, a single pixel can be approximated by a parallel plate capacitor. Consequently, it is expected that its capacitance increases with decreasing distance of the two plates which corresponds to an increase of the depletion zone. For a parallel plate capacitor the capacitance is given by:

$$C = \epsilon_0 \epsilon_r \cdot \frac{A}{d} \tag{3.21}$$

with A being the area of the plates and d their distance. Assuming this simplified model, one would expect that the CV-f curve of a SiPM shows an inverse proportional behavior. This can be seen in Fig. 3.14, where the parallel capacitance as well as the series resistance of a SiPM for different AC frequencies are plotted as a function of voltage. The series resistance R_s has been chosen for plotting, because it is unlike the conductance G_p a parameter used to extract parameters of the SiPM (see section 3.3.2). R_s can be calculated by transforming the equivalent parallel circuit into the corresponding series circuit (see

Fig. 3.13) using the following equation:

$$R_s = \frac{G_p}{G_p^2 + (2\pi f \cdot C_p)^2} \tag{3.22}$$

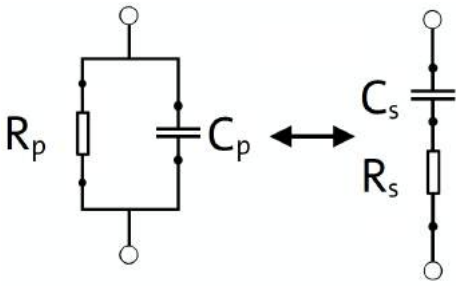

Fig. 3.13: The equivalent parallel (left) and series (right) circuit representation of the SiPM. For calculations it is useful to switch between the two representations [27].

The behavior of the series resistance can also be predicted: Assuming the resistor R_s in Fig. 3.13 behaves like an ohmic resistor, its resistance should not change with voltage or frequency, so all changes can be attributed to the capacitor. The impedance Z_{cap} of a capacitor can be calculated using [23]:

$$Z_{cap} = \frac{1}{j\omega C} \tag{3.23}$$

Based on this equation, the series resistance should decrease with increasing frequency. However, since the capacitance decreases with increasing voltage, the series resistance should rise as a function of voltage. Going to higher frequencies, this rise should decrease because the capacitor can then be interpreted as a short circuit. All of these features can be seen in Fig. 3.14.
In the following section it is explained how one can extract SiPM parameters from the plots discussed above.

3.3.2 Determination of SiPM Parameters

In order to extract observables from CV-f measurements, it is necessary to analyze the equivalent circuit diagram for the reverse biased SiPM as it is shown in Fig. 3.15.

R_{par} and C_{par} are parasitic contributions from leakage currents, biasing lines and the readout electronics, R_L is the load resistance of the readout, C_{pix} the pixel capacitance, R_q and C_q are the quenching resistance and capacitance. Moreover, there are also some switches drawn in the circuit. They simulate the avalanche breakdown:
The switch S_{CV} connects the SiPM to the CV-f/IV measurement device and also to the AC-voltage. S_{op} is the connection to the DC voltage source and the opened S_{bd} represents

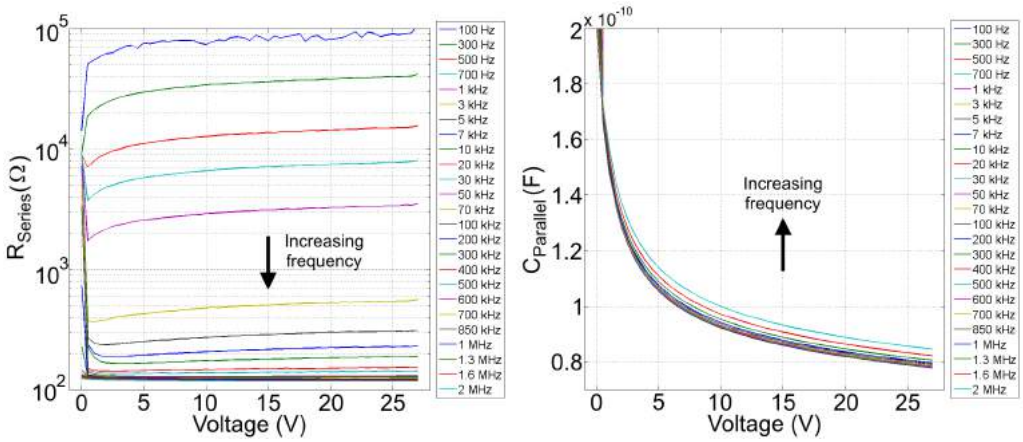

Fig. 3.14: Left: The measured parallel capacitance of a SiPM as a function of voltage for different frequencies. Right: The series resistance of a SiPM transformed from the measured parallel conductance as a function of voltage for different frequencies.

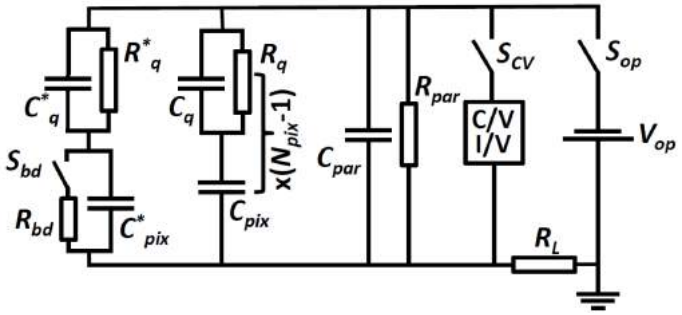

Fig. 3.15: The equivalent circuit diagram for a reverse biased SiPM. Depicted in the figure are from left to right: A single pixel about to experience a breakdown, the remaining $N_{pix} - 1$ pixels, the parasitic contributions from leakage currents, biasing lines and the readout electronics, the CV/IV measurement devices, the voltage source [11].

the depletion region without a breakdown.

When the S_{op} and S_{CV} are closed, the closing of S_{bd} starts the discharge of the pixel. It will discharge until the voltage drops from V_{op} to V_{bd}. Afterwards, when the current is quenched, the switch S_{bd} is opened again and the pixel can recharge.

Using the equivalent circuit diagram of Fig. 3.15, the complex resistance Z of a SiPM with N_{pix} pixels can be calculated from:

$$Z = \left(\frac{1}{R_{par}} + j\omega C_{par} + N_{pix} \cdot \left(\frac{1}{j\omega C_{pix}} + \frac{R_q}{1 + j\omega C_q R_q} \right)^{-1} \right)^{-1} \tag{3.24}$$

For different frequencies and voltages as well as for different representations of the SiPM equivalent circuit (series/parallel circuit, see Fig. 3.13), different terms in equation (3.24) will dominate. From analyzing the different cases it is possible, to determine several

SiPM parameters like the pixel capacitance or the quenching resistance. These two parameters are especially important because the recharge or dead time τ_r of a single pixel and the gain G of the SiPM (see Eq. (3.11)) depend on them.

Determination of the Quenching Resistance

Starting with the limit of high frequencies: In this case, the influence of the parasitic resistance R_{par} becomes so small that it can be ignored. Also the contribution of the capacitor to the series resistance is minimal and consequently, the series resistance can be used to calculate the quenching resistance in the following way:

$$R_q = R_s \cdot N_{pix}. \tag{3.25}$$

Where R_s is calculated using equation (3.22).
Fig. 3.16 shows the series resistance at 1 V below breakdown as a function of frequency [2]. Going to a lower voltage, e.g. 1.5 V below breakdown, results in values that differ by less than 0.01 % (several $\mathrm{m}\Omega$).
As it can be seen, the series resistance decreases with frequency until it stays constant for frequencies higher than 100 kHz. To extract the values it is possible to either apply a linear fit (as implied in the picture) or since the values hardly differ (below 0.1 %) at a certain region, to directly extract the value from a single point. The latter option was chosen for the analysis in this thesis.

Determination of the Pixel Capacitance

To be able to determine the pixel capacitance, the influence of the parasitic and the quenching capacitance have to be comparatively small so that they can be ignored. This is true for voltages above the depletion voltage and further increasing the voltage improves the quality of this approximation. Thus, values for voltages just below breakdown are used for the calculation:

$$C_{pix} = \frac{C_p}{N_{pix}} \tag{3.26}$$

Fig. 3.17 shows the measured parallel capacitance at 1 V below breakdown as a function of frequency. Going to a lower voltage, e.g. 1.5 V below breakdown, results in values that are approximately 0.3 % larger (≈ 250 fF).
For frequencies below 1 kHz the values decrease with increasing frequency. Up to

[2] The divergent data points at 1.3 and 1.6 MHz are caused by a problem of the LabVIEW program. The interpreter cut off the digits behind the dot which resulted in a repetition of the measurement at 1 MHz. Nevertheless, the measurement was then attributed to the data point of 1.3 or 1.6 MHz respectively. For the analysis these points are excluded. The same applies for Fig. 3.17

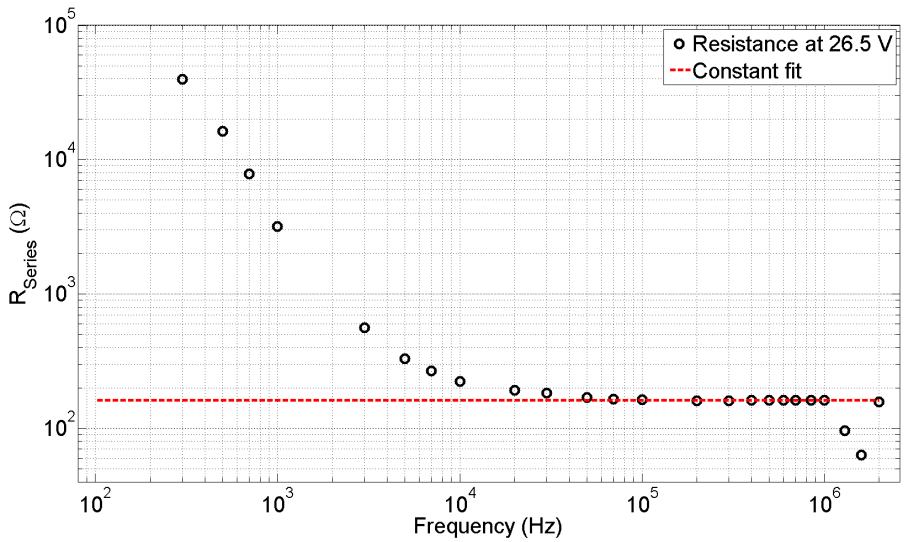

Fig. 3.16: Series resistance as a function of frequency for a SiPM operated at 26.5 V in reverse, which corresponds to one volt below the breakdown voltage. The fit can be used to extract values for the determination of the quenching resistance.

200 kHz the capacitance stays constant, above 200 kHz it increases again. Again there are two possibilities to extract the value for C_p: Either with a linear fit in the constant region as shown in the figure or by directly taking a single value without further calculations. Since the values of the capacitance around 10 kHz do not vary by more than 0.1 %, the value is directly taken without any fitting.

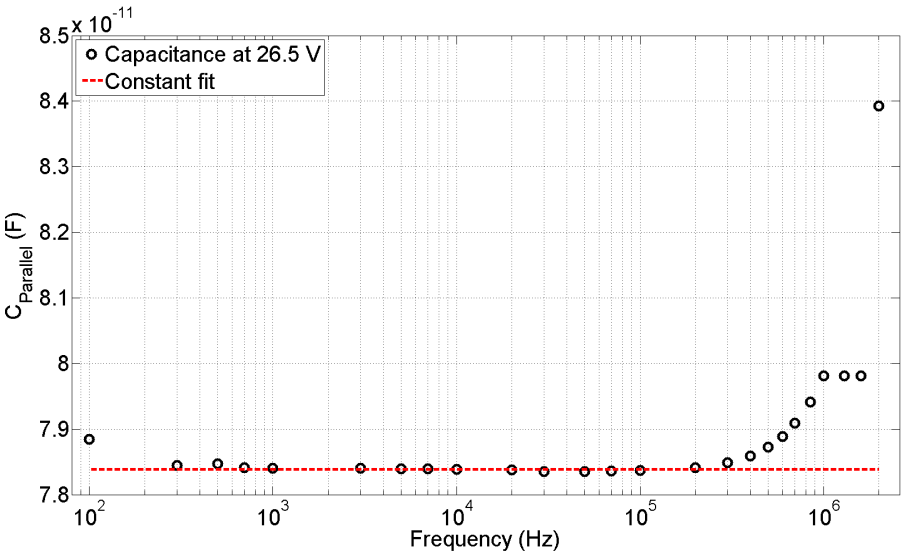

Fig. 3.17: Parallel capacitance as a function of frequency for a SiPM operated at 26.5 V in reverse, which corresponds to one volt below the breakdown voltage. The fit can be used to extract values for the determination of the pixel capacitance.

Other Parameters obtained from CV-f Measurements

Next to the pixel capacitance and quenching resistance, various other parameters that are not investigated in the course of this thesis can be extracted from a CV-f measurement. For example the effective doping concentration N_{eff}, the electric field E or the depletion voltage V_{dep} [26].
Additionally, the equivalent circuit diagram in Fig. 3.15 includes more than just R_q and C_{pix}. There are also a quenching capacitance and a parasitic contribution depicted. The additional quenching capacitance has proven to be very small and negligible (i.e. < 5 fF) [48]. The parasitic resistance can be calculated from the parallel resistance ($R_p = G_p^{-1}$) of the CV-f measurements at low frequencies and high voltages [48].
Furthermore, in order to explain the rise of the parallel capacitance at high frequencies, an inductance connected in series to the pixels is introduced (see Fig. 3.18). Fig. 3.19 shows a comparison of the circuit models with and without the series inductance. Without the series inductance the values of C_p are expected to go down for frequencies higher than 100 kHz. However, this is not observed in the measured data (black markers), instead the parallel capacity rises for high frequencies.

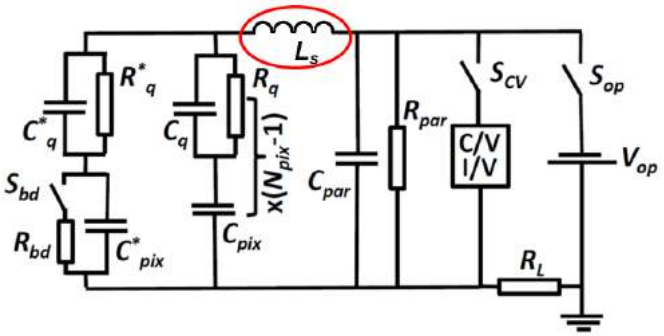

Fig. 3.18: Enhanced equivalent circuit of a reverse biased SiPM with an additional inductance in series in order to describe the rise of C_p at high frequencies.

With the additional series inductance equation (3.24) becomes:

$$Z = \left(\frac{1}{R_{par}} + j\omega C_{par} + \frac{1}{j\omega L_s + \frac{1}{N_{pix}} \cdot \left(\frac{R_q}{1+j\omega C_q R_q} + \frac{1}{j\omega C_{pix}} \right)} \right)^{-1} \tag{3.27}$$

This origin of the inductance is not yet understood, but there are two possible explanations: First, an inductance is equivalent to a *negative capacitance*, because a negative capacitance has the same phase relationship between voltage and current as a positive inductance. This is something that has been observed in many semiconductor devices [56].
Second, the fact that such a negative capacitance occurs at high frequencies can also be an indicator of a parasitic inductance of the external circuit [56].

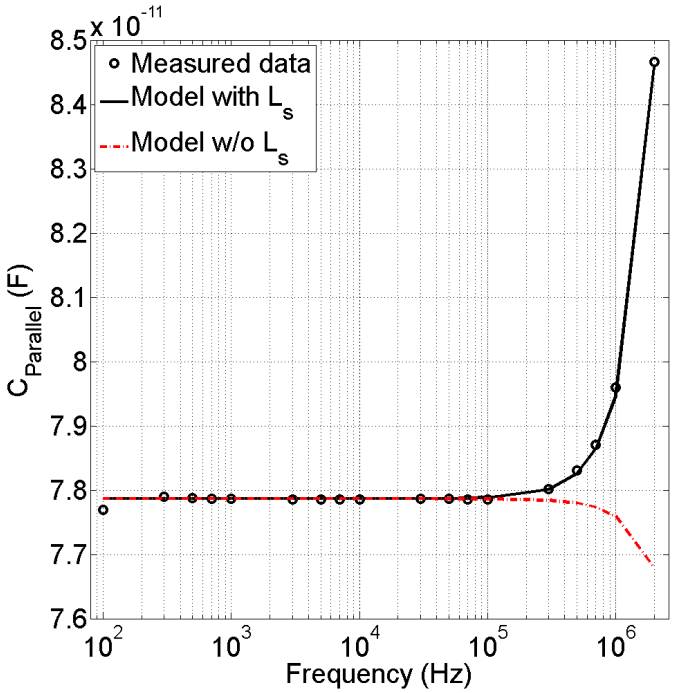

Fig. 3.19: Comparison of the models for the SiPM circuit with and without the series inductance included.

Nevertheless, this parameter is not thought to be crucial for the SiPM characterization or its performance. Its values are determined in chapter 4 but without further investigation (Future studies of this trait are not ruled out). The series inductance can be determined from the parallel capacitance C_p at the highest frequency (2 MHz), because for this frequency the parasitic contributions can be ignored. For the other parameters, the extracted values for R_q and C_{pix} are inserted into equation (3.27) and C_q is fixed to $C_q = 0$.

3.4 Charge-Voltage Measurements

The IV and CV-f measurements are used to determine static electrical parameters of the SiPMs. They provide information about the minimum voltage needed to operate the device or how fast the single pixels recharge.
However, it is also important to know under which operational conditions the SiPM works best. The main concern is the proper excess voltage because it influences the gain of the SiPM but also the dark count rate as well as the probability of fake signals caused by cross-talk or afterpulses. In general, the values of these parameters increase with increasing excess voltage. While it is useful to obtain a high gain, the DCR and the XT/AP probability should be as small as possible. So the goal is to find the best trade-off between those quantities.
All of these parameters can be extracted from charge-voltage or QDC-measurements. For

these measurements, which are explained in the following section, the charge generated by a reverse biased SiPM illuminated with a pulsed LED is integrated over a certain time duration (*integration gate*).

3.4.1 Measurement Setup

In Fig. 3.20 the setup for the charge-voltage measurements is outlined. The equivalent circuit diagram of the decoupling circuit used for the readout is depicted in Fig. 3.21.

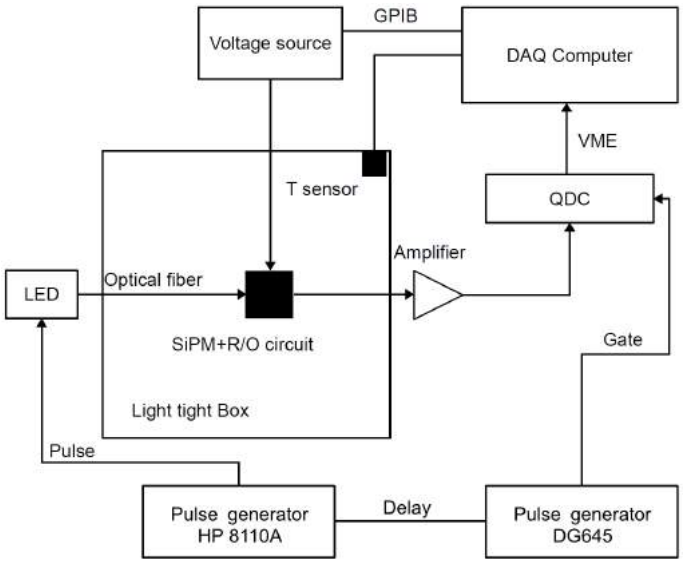

Fig. 3.20: Schematic of the complete setup that is used to perform the charge-voltage measurements [27].

The investigated SiPM is kept at room temperature in a light tight box with included air conditioning system by ESPEC [57]. To allow illumination with a pulsed LED, an optical fiber is guided into the box via a cable duct, which is also used to insert the cables for the voltage supply and readout. An Agilent HP 8110A pulse generator [58] is used to drive the LED, which emits pulses with a wavelength of 470 nm and a pulse duration of 4 ns. In addition, a digital pulse generator DG645 from Stanford Research Enterprise [59] sets the integration gate length of 100 ns and the delay between the start of the gate and the LED pulse[3]. Following the recommendation of the producer, the delay is set to 15 ns. The voltage source for the SiPM is a Keithley 6487 [60] and to measure the integrated current (i.e. charge) a CAEN charge-to-digital converter (QDC V965) [61] is used. Before measuring the signal, the current is amplified by a factor of 50 using a Phillips Scientific Amplifier Model 6954 [62]. A DAQ computer, which is also used for controlling the entire setup via root routines, stores the histograms (also called pulse height spectra) taken. The

[3] In previous studies the DG645 was used for both purposes: controlling the pulses and the gate. However, it was observed that the pulses created by the HP8110A are more stable thus it was introduced to control the pulses.

overall uncertainty of the charge measurements is estimated to be around 10 %. Additionally, an oscilloscope from Tektronix (DPO7254 [63]) is included in the setup. It can be used to record waveforms and to check for example the right timing of the gate with respect to the LED pulse.

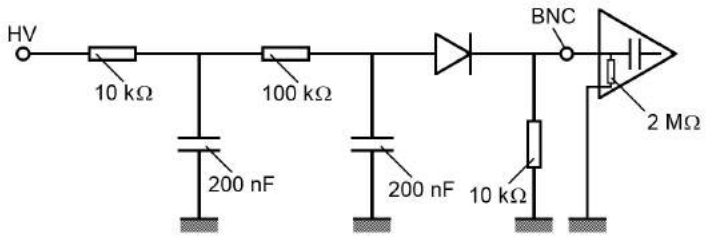

Fig. 3.21: Equivalent circuit diagram of the decoupling circuit used for the QDC setup.

The length of the integration gate is chosen so that entire SiPM signal is contained inside. This is verified with so called *delay scans*. For a delay scan, the signal of the SiPM is measured with a certain gate length while varying the delay between the LED pulse and the beginning of the gate in steps of 2 to 20 ns. Fig. 3.22 depicts oscillograms of three different steps of a gate scan: One where the pulse starts to enter the gate, one where it is in the middle of the gate and one where the pulse has nearly left the gate.

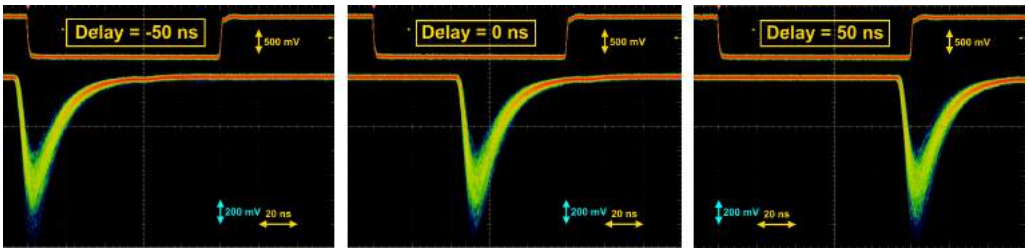

Fig. 3.22: Oscillograms of different steps of a delay scan to determine the optimum gate length to investigate the SiPMs signal. The gate length is 100 ns and the SiPM is illuminated with an LED with high light intensity.

A gate scan results in *delay curves* like the ones shown in Fig. 3.23. Plotted are the mean values of the integrated signal as a function of the delay. From this plot the proper gate length can be determined. The first gate lengths up to 50 ns are too short. They don't reach the plateau region the other gates exhibit, which means that not the entire SiPM signal is contained within the gate. The gate with 75 ns length reaches the plateau region but the integrated signal decreases directly after the maximum value is reached. For the SiPM used for this measurement this gate length would be suitable. However, for SiPMs with a longer recharge time, this gate might cut off part of the pulse signal. So in order to have a bit of tolerance, the next gate length (100 ns) is used for the QDC measurements. Even longer gates are not considered because by using them an increasing contribution of noise would be integrated. This can be seen in the fact that the plateau region is not stable, but steadily reaches higher values with increasing delay and gate length.

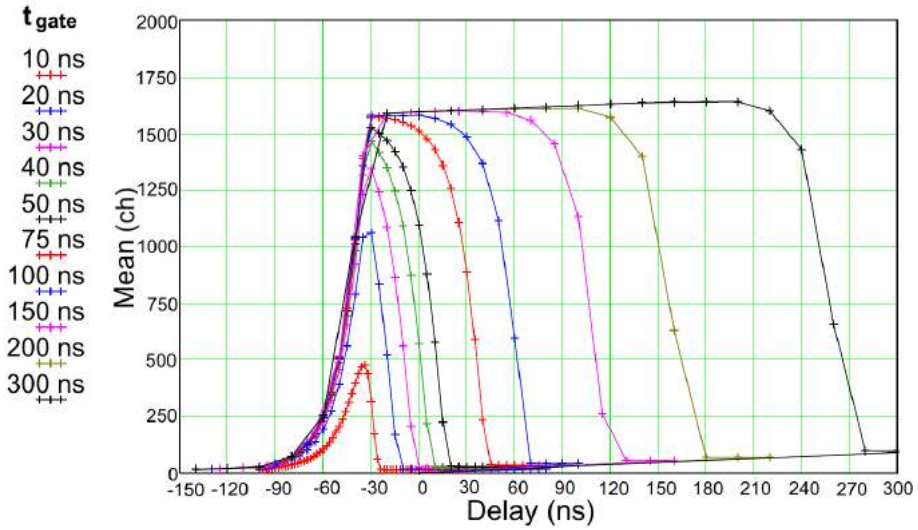

Fig. 3.23: Delay curves of a SiPM for different gate lengths measured with the QDC. The SiPM is operated above breakdown and illuminated with high light intensity. In Fig. 3.22 three of the delay positions are shown.

3.4.2 Charge-Voltage Histograms

For the charge-voltage measurements the SiPM is biased in reverse and above the breakdown voltage. If the resulting current is recorded as a function of time, for example with an oscilloscope (see Fig. 3.24), the number of pixels experiencing a breakdown due to incoming photons can be seen as pulses of different amplitude. The flat line corresponds to the signal of no pixels discharging, the first and smallest pulse corresponds to one pixel discharging, the second to two pixels discharging and so on.

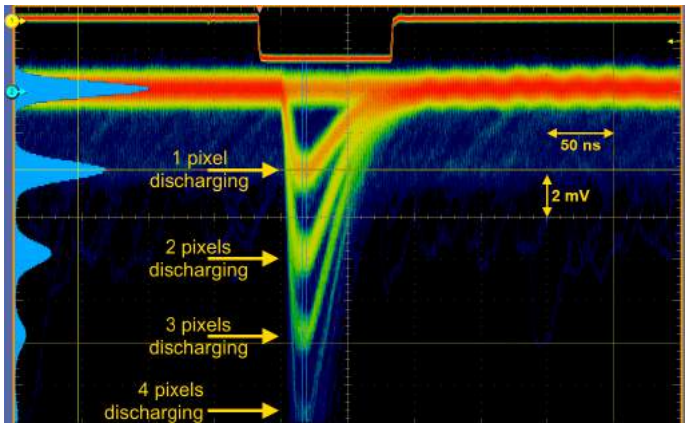

Fig. 3.24: Oscillogram showing signals from a SiPM operated above breakdown and illuminated by a pulsed LED. The pulses with different amplitudes refer to a different number of pixels discharging.

What can also be estimated from the waveforms of the oscilloscope is the pulse shape of the SiPM (see Fig. 3.25). It provides a good way of checking if the values determined

from the CV-f measurements for τ_r are compatible. And in fact, it turned out that the values for τ_r agree with the values obtained from the pulse shape.

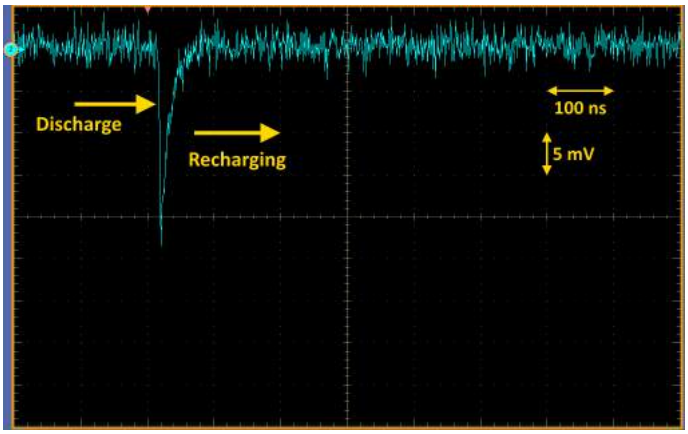

Fig. 3.25: Oscillogram showing a single pulse from a SiPM operated above breakdown and illuminated by a pulsed LED. The pulse is characterized by its fast discharge and the slower recharge process (~12 ns).

For the work of this thesis, the charge-voltage measurements are not done with the oscilloscope but with the QDC. The QDC measures the integrated current at different voltages and the measurements are saved as number of events as a function of channels. One channel corresponds to a certain charge, depending on the QDC setting. The QDC has a dual input range with either 200 fC per channel or 25 fC per channel [61]. This allows to avoid saturation with big charge pulses while increasing the resolution with smaller ones.
Similar to the IV measurements, the QDC measurements are performed with two different light settings and for each of the settings a different input range was chosen. Since the QDC setup also does not provide a possibility to determine the absolute intensity of the LED, the amount of light has to be defined differently.
Firstly, the low LED setting: The waveform of the illuminated LED is checked with the oscilloscope and the LED voltage is set so that at 3 V excess voltage the ratio of zero pixels discharging versus one pixel firing is about 1:1. This is done using the fast acquisition mode of the oscilloscope, where multiple signals are shown at the same time and the color coded intensity of the resulting curve represents the frequency of occurrence. The resulting LED voltages are between 3 V and 4 V and the smaller input range (25 fC/channel) of the QDC is used.
Secondly, the high light setting: For this setting the LED voltage is set to a fixed value of 8 V for every measurement, because it has been observed that for voltages in that range the histogram behavior does not change significantly (e.g. the number of peaks displayed does not change). In this case because of the higher currents due to more pixels firing the higher input range (200 fC/channel) of the QDC has to be used.

The measurement process can be divided into three parts:

The first part is to measure the pedestal i.e. the signal caused by electric noise of the setup itself. For this measurement, the LED is turned off and a small reverse voltage (10 V) is applied to the SiPM. The pedestal acts as a zero level and its mean value has to be subtracted from the measured values in the analysis. In Fig. 3.26 the pedestal measurements for the two input ranges are shown. Their basic shape is the same, but since each setting corresponds to a different ratio of charge per channel, different values are reached and the number of channels covered differs.

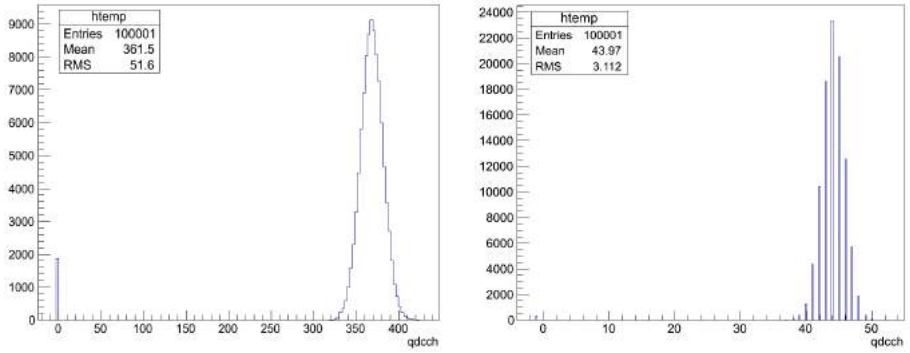

Fig. 3.26: Histograms of the pedestal measurements in the cases of low input range (left) and high input range (right). The peak at -1 is not of physical nature, but an artifact caused by errors during the data taking. The points are excluded in the analysis.

The second part is to measure the dark spectrum. In this case the LED remains turned off, but for each successive measurement, the voltage is ramped up from an excess voltage of 3 V to 8 V in steps of 0.5 V. The goal of this measurement is to determine the DCR as well as the XT and AP probability, which will be explained in section 3.4.4.
An example of how the histograms of such measurements for the two input ranges look like is shown in Fig. 3.27. Each peak corresponds to a different number of pixels discharging, with the first peak being the pedestal, so the signal of no pixels discharging. Just like before the basic shape of the histograms is the same and the main difference lies in the values and number of channels covered.

The third and final part is measuring the response of the SiPM to light. The same voltage steps as for the DCR measurement are used, but this time the LED is turned on. The histograms for two different excess voltages in the case of low LED intensity are shown in Fig. 3.28 and in the case of high LED intensity in Fig. 3.29.
What can be seen is that as a result of the illumination, more pixels experience a breakdown and thus more peaks are observed in the histograms. Additionally, the peaks are much better separated than in Fig. 3.27, because comparatively less entries contribute to the pedestal. Another influence in the dark spectrum measurements are pulses that are taking place outside or at the end of the gate. These pulses are only partially integrated and result in entries between the peaks. It can also be seen that for higher voltages (right

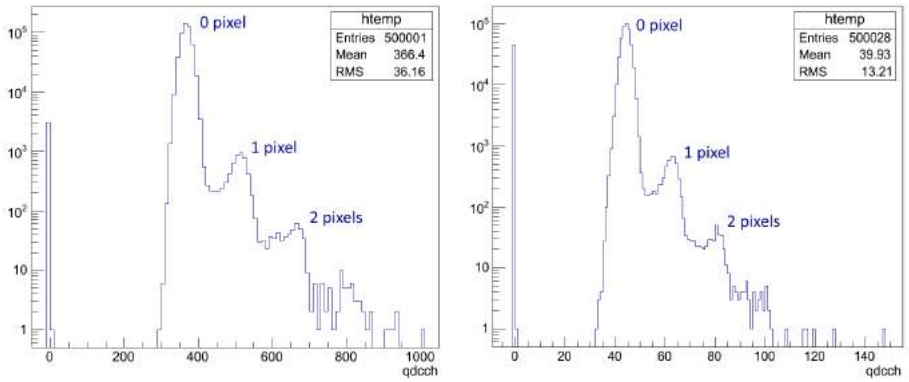

Fig. 3.27: Histograms of the DCR measurements at 5.5 V excess voltage in case of the low input range (left) and the high input range (right). Each peak corresponds to a different number of pixels firing.

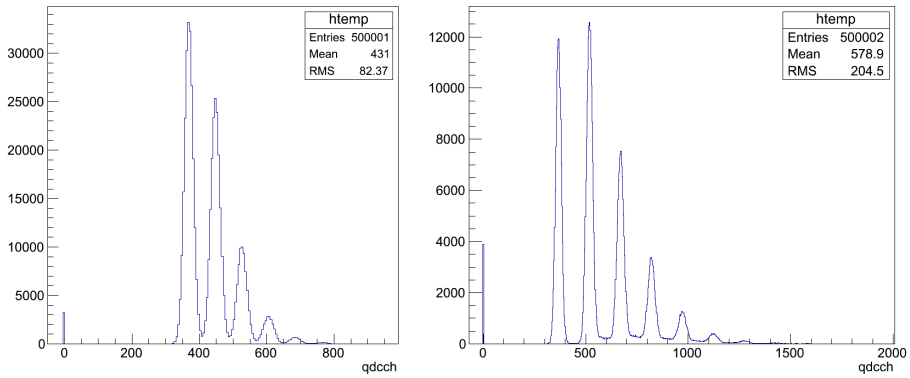

Fig. 3.28: Histograms of charge voltage measurements with low LED intensity at 3 V excess voltage (left) and at 5.5 V excess voltage (right). The QDC is operated at the low input range.

histograms) more peaks occur and again the contribution of the pedestal to the whole number of entries diminishes. This is due to the fact, that the avalanche breakdown probability increases with increasing voltage.

For the higher LED illumination, more pixels are expected to be discharging, since more photons arrive at the SiPM. And indeed it can be seen that while in Fig. 3.28 the furthest peak is the one of six pixels firing, the furthest peak for the high illumination in Fig. 3.29 corresponds to 16 pixels firing.

Since the SiPM has over 4000 pixels in total, the occurring of a photon induced avalanche in these pixels is a rare event and the process can be described with Poisson statistics. On the other hand, the single peaks have, up to a certain degree, a Gaussian shape. The width of the first peak σ_0 corresponds to the fluctuation of the electronic noise [27]. The spread in the subsequent single peaks is caused by two effects:

First, the production-based differences in the capacitances of the single pixels. In the case of each pixel storing the exact same amount of charge, one would expect all the peaks to have the same width and the same distance from each other, because two pixels firing

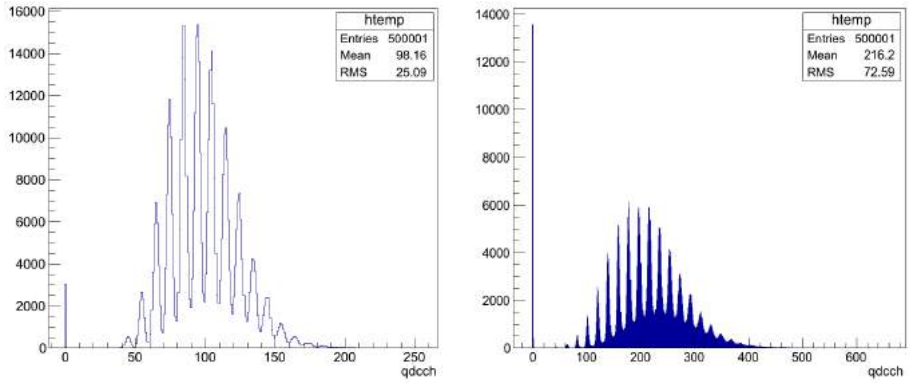

Fig. 3.29: Histograms of charge voltage measurements with high LED intensity at 3 V excess voltage (left) and at 5.5 V excess voltage (right). The QDC is operated at the high input range.

would just produce the same signal as one pixel firing times two. In reality this is not true and the succeeding peaks become more and more broadened.
Second, the Geiger discharge and also the avalanche quenching are statistical processes, as a result not always the same amount of charge is produced and not always the exact same voltage is reached after quenching.
The spread in the widths for subsequent peaks σ_N can be estimated using the propagation of uncertainty and is given for the N-th peak by [27]:

$$\sigma_n^2 = N \cdot \sigma_G^2 + \sigma_0^2 \quad where\ \sigma_G^2 = \sigma_1^2 - \sigma_0^2, \ \ and\ N = 1, 2, 3... \tag{3.28}$$

Deviations of the single peaks from a pure Gaussian shape are caused by afterpulses and delayed cross-talk. Both shift the entries to higher channel numbers and thereby cause additional entries between the peaks.
From the LED measurements it is possible to extract the gain and the breakdown voltage of the SiPM. This will be explained in the subsequent section.

3.4.3 Determination of the Gain and Breakdown Voltage

In order to be able to correctly analyze the output of a SiPM, it is of great importance to know its gain G. Consequently, a reliable method to determine G is crucial to characterize a SiPM. As shown in equation (3.11), G is linearly dependent on the excess voltage, so it is important to precisely determine the breakdown voltage. The QDC measurements with pulsed LED illumination offer possibilities to determine the gain, its dependence on the voltage dG/dV and the breakdown voltage V_{bd}.
To extract the gain from the QDC histograms, the peak position of each single peak is extracted with a Gaussian fit. As already explained, each pixel should ideally have the same capacitance and thus the same gain. Now it is possible to plot the mean charge of

the peaks as a function peak position/number of pixels discharging. Afterwards, a linear fit is applied to these values, as it is shown in Fig. 3.30 and the gain can be calculated by [27]:

$$G(V) = \frac{1}{q_0} \cdot \frac{dQ_m}{dn_{pix}} = C_{pix} \cdot \frac{V - V_{bd}}{q_0}\,, \tag{3.29}$$

where q_0 is the elementary charge, Q_m the integrated charge, n_{pix} the number of discharging pixels, C_{pix} the pixel capacitance, V the voltage applied and V_{bd} the breakdown voltage. The gain corresponds to the distance between the single peaks.

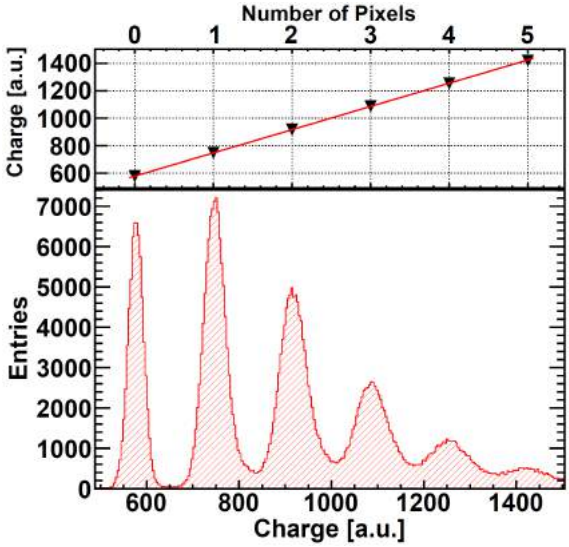

Fig. 3.30: Pulse height spectrum of an illuminated SiPM with an additional plot of the charge as a function of the number of discharging pixels on top. A linear fit is applied through the mean values of each peak to determine the SiPMs gain [27].

The result of the gain calculation $G[ch]$ is given in units of channels and to calculate the absolute gain G_{abs}, the charge per channel of the input range $IR(\frac{q}{ch})$ and the gain of the amplifier G_{Amp} have to be taken into account:

$$G_{abs} = \frac{G[ch]}{q_0 \cdot G_{Amp}} \cdot IR(\frac{q}{ch}) \tag{3.30}$$

According to the right part of equation (3.29), the gain should be equal to zero (which is of course purely theoretical) at the breakdown voltage. Hence, if the gain is plotted as a function of voltage V, the breakdown voltage V_{bd} is determined by extrapolating the curve, in order to determine the intercept of the straight line with the x-axis, as it is implied in Fig. 3.31.

Beyond that, it should be mentioned that for this analysis only the low LED intensity measurements are evaluated, because the smaller input range allows a more precise determination of the peak positions. As it can be seen in Fig.+3.29 the peaks of the high intensity measurements are not clearly separated due to the worse sensitivity and the

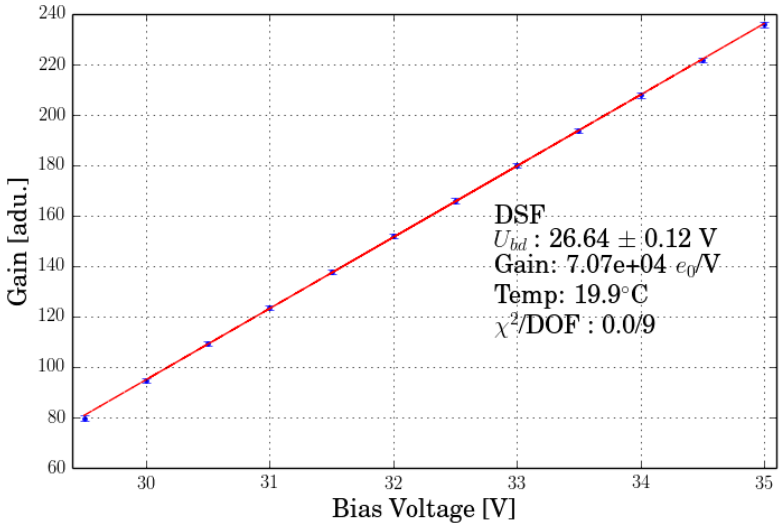

Fig. 3.31: The gain of an illuminated SiPM as a function of voltage. A linear curve is fitted through the points and extrapolated to zero in order to determine the breakdown voltage, that is calculated to be around 26.6 V.

spread caused by the differing pixel capacitances. This spread is augmented by the fact that there are more peaks than for the low light measurement, so that the spread propagates even further (see Eq. (3.28)). The automatized Gaussian fitting procedure used for the low light setting does not work in this case.
A proper analysis method for the high light measurements has not yet been established. The main motivation for taking measurements with this light setting was the expected increase in the dark current after neutron irradiation. The single photon resolution of the SiPMs was expected to be lost for the irradiation fluences above 10^{11} n/cm^2 and in the worst case also for the fluences below. The histograms are thought to be dominated by the dark current. With higher LED intensity the photon induced avalanches are expected to be the dominant contribution to the total current thus giving the possibility to extract the gain from the histograms.

3.4.4 Determination of the Dark Count Rate

The dark count rate (DCR), cross-talk (XT) and afterpulsing (AP) influence the SiPMs performance in a negative way and should be minimized. Since they are all dependent on the excess voltage, it is of high interest how they behave as a function of voltage and if there is an optimal voltage range for the SiPM operation. DCR, the XT and AP probability can all be determined from the QDC measurements with the LED turned off. The determination of the DCR is covered in this chapter, the determination of the XT and AP probability in the next one. The occurrence of dark counts is a Poisson process and an

exponential distribution can be used to describe its occurrence probability. The probability $P_0(\Delta t)$ of no dark count occurring within the time interval Δt can be calculated by [11]:

$$P_0(\Delta t) = exp(-DCR \cdot \Delta t) \tag{3.31}$$

The DCR is defined as being every signal that is observed above the 0.5 pixel threshold (see Fig. 3.32) per second. Every signal registered below the threshold is accounted for electronic noise from the readout. Although this may exclude some events from the peak of 1 pixel firing because of the peaks spread. For Δt the integration gate length of 100 ns is used. Knowing the number of dark counts and the integration gate length, the DCR can be calculated for each voltage using equation (3.31).

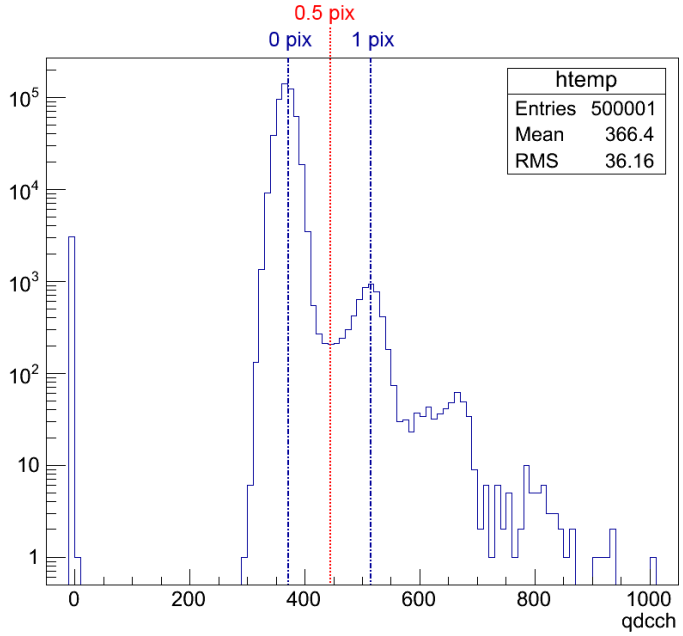

Fig. 3.32: Histogram of a charge voltage measurement of a SiPM measured with the LED turned off. All entries above the 0.5 pixel threshold are considered to be dark counts. The excess voltage is about 5.5 V.

Fig. 3.33 shows the resulting curves of this analysis. The DCR is given in counts per second (cps). Another common unit for the DCR is Hertz. It can be seen that the DCR increases with voltage and shows no indication of a saturation for higher voltages. So applying a higher voltage increases the SiPMs gain but at the same time results in a higher DCR. The increase can be explained by the increased avalanche triggering probability due to the higher voltage and the increase in tunneling effects, that generate free charge carriers, due to the higher electric field.

The values plotted at 29.5 V are not correct and show a wrong behavior. The sample W1-B2-S2 for example shows a decrease of the DCR from 29.5 V to 30 V. The discrepancy can be explained by looking at the DCR histograms of the lowest voltage. One of them

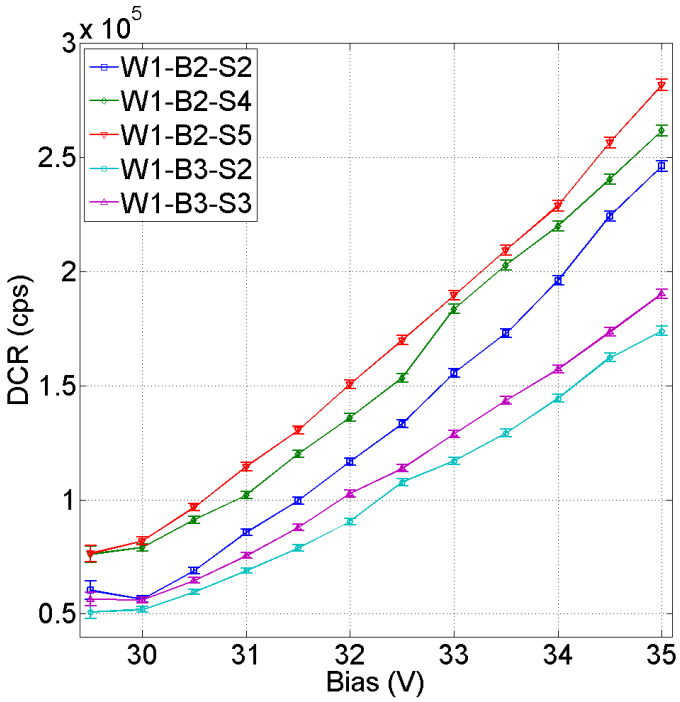

Fig. 3.33: The DCR in counts per seconds of several KETEK SiPMs as a function of voltage. The devices breakdown voltages determined from the QDC measurements are around 26.6 V.

is shown in Fig. 3.34: The applied reverse voltage is 29.5 V, which corresponds to an excess voltage of 3 V. In this case, the first peak and the pedestal are not clearly separated, Consequently, the 0.5 pixel threshold cuts off a considerable part of the pedestal and leads to a calculated value of the DCR that is higher than it should be.

3.4.5 Determination of the Cross-Talk and Afterpulse Probability

Geiger avalanches caused by cross-talk or afterpulses are registered in the histograms as events at channels above the first peak, since they involve two or more separate pixels firing or one pixel firing twice within the integration gate length. Because of their correlation to previous events, cross-talk and afterpulses are sometimes labeled as *correlated noise* and the probability of them to occur is called *correlated noise probability* (CNP) [27]. To determine the CNP, a second threshold at a 1.5 pixel level is introduced (see Fig. 3.35). Again, the spread of the peak is taken into consideration for this choice. The cross-talk and afterpulse probability is then calculated by the fraction of events that have more than one pixel fired:

$$P_{XT/AP} = \frac{N_{>1.5pix}}{N_{>0.5pix}} \times 100\% \tag{3.32}$$

Of course it is possible that two pixels fire at the same time and for higher voltages and increasing DCR this probability increases. This effect has to be taken into account when

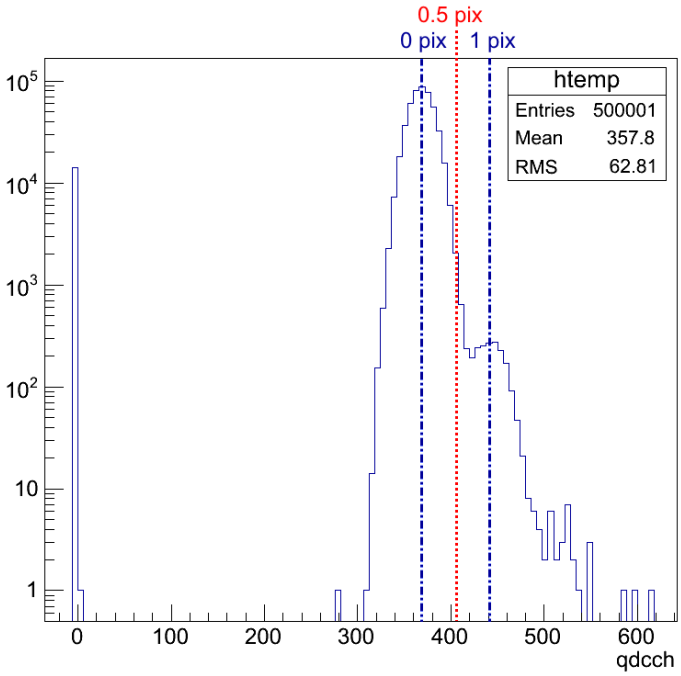

Fig. 3.34: Histogram of a charge voltage measurement of a SiPM measured with the LED turned off. The excess voltage is only 1.9 V and the peaks merge into each other and the 0.5 pixel threshold cuts off part of the pedestal. This results in wrong values for the calculated DCR.

calculating the uncertainties of the cross-talk and afterpulse probability.

In Fig. 3.36 the cross-talk/afterpulse probabilities of two SiPMs, calculated with equation (3.32), are plotted. For clarity, only two curves are shown, because unlike for the DCR the SiPMs hardly differ in terms of the XT/AP probability. The increase of the XT and AP has two reasons:
Firstly, the already mentioned increase of the avalanche trigger probability due to the higher voltage that also applies for de-trapped charge carriers. Secondly, a higher voltage leads to a higher gain, which again leads to more charge carriers, created within a discharge. Thus also the number of photons created increases, that can reach adjacent pixels.
Looking at the error bars on the first data points and comparing them with the ones on the last points, it can also be seen that the last bars are larger. This is because of the previously mentioned influence of the increasing DCR. However, it should be kept in mind that the values for the lowest voltages have a larger systematic error because similar to the DCR determination, the single peaks in the DCR spectrum are not clearly separated. Additionally, if one looks at Fig. 3.34, one sees that the peak, corresponding to two pixels discharging, is not even clearly distinguishable. Hence, the 0.5 pixel and 1.5 pixel thresholds don't provide a reliable basis for the calculation of the DCR at low excess voltages.

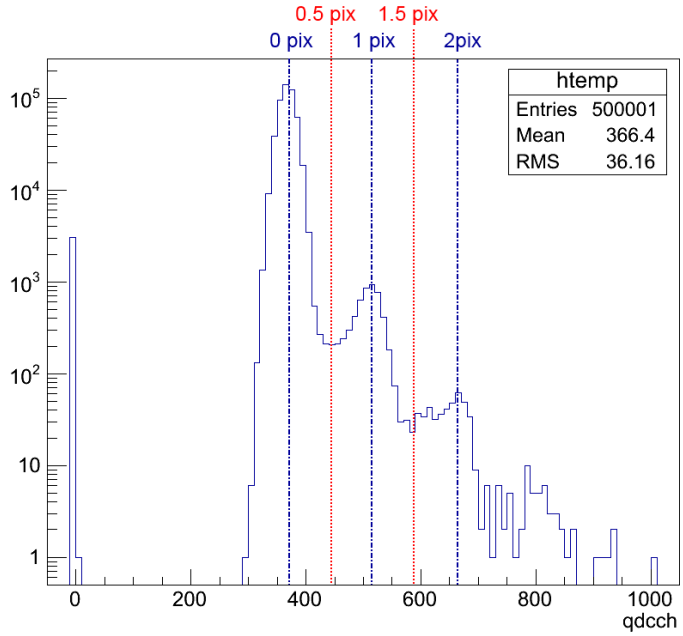

Fig. 3.35: Histogram of a charge-voltage measurement of a SiPM measured at 5.4 V excess voltage with the LED turned off. The 0.5 pixel threshold separates the dark counts from the pedestal and the 1.5 pixel threshold the XT or AP induced counts from the dark counts.

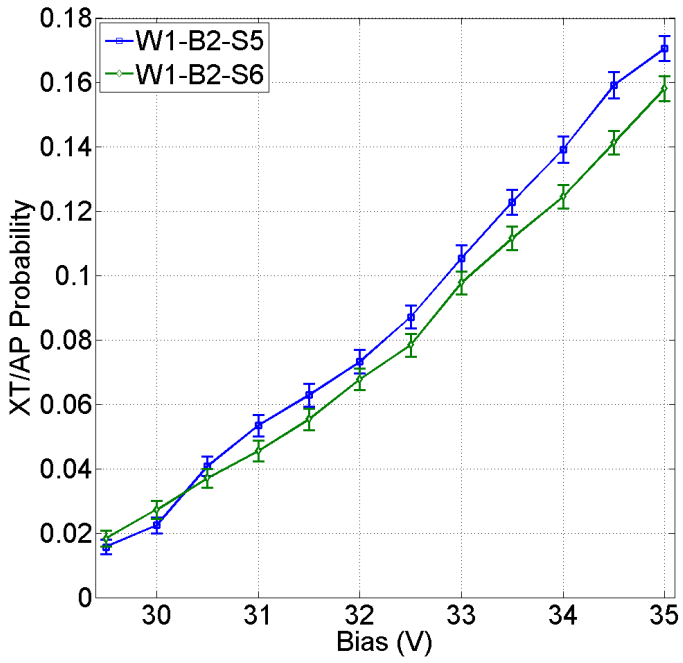

Fig. 3.36: The cross-talk/afterpulse probability of two KETEK SiPMs as a function of voltage. The devices breakdown voltages determined from the QDC measurements are around 26.6 V.

4 Analysis Results

In this chapter, the characterization methods explained in section 3 are used to compare the performance of the SiPMs before and after irradiation. The goal is to show how the neutron irradiation influences different parameters of the SiPMs. The SiPMs were irradiated at five different fluences at the TRIGA Mark II reactor in Ljubljana [64]. Namely 10^9, 10^{10}, 10^{11}, $5 \cdot 10^{11}$ and 10^{12} $\mathrm{n/cm^2}$. Since there are ten SiPMs from each wafer, two samples from each wafer were irradiated at the same fluence. The amount of radiation a SiPM receives is controlled by the duration of its stay near the reactor core. In this way deviations of up to 10 % occur. The neutron irradiations were done at room temperature and without applied bias. After irradiation and between the measurements the SiPMs were stored at -20 °C in order to avoid annealing.
Section 4.1 is about the IV measurements. The behavior of the quenching resistance, the breakdown voltage, the ILD and the different contributions to the current are discussed. In section 4.2 the CV-f measurements are discussed. From them several SiPM parameters like the quenching resistance, the pixel capacitance and the parasitic resistance are extracted. Their values before and after irradiation are evaluated and compared. In addition, the values for the quenching resistance gained from the CV-f measurements are compared to the values extracted from the IV measurements.
Section 4.3 gives an overview of the analyzed QDC measurements before and after irradiation. Parameters extracted from the QDC measurements are the gain, the dark count rate (DCR), the cross-talk (XT) and afterpulse (AP) probability and the breakdown voltage. An explanation for the difference of breakdown voltage determined from IV and QDC measurements is given. Also the section features an explanation why the methods applied before irradiation cease to work after irradiation.

4.1 Current-Voltage Measurements

The SiPM current-voltage characteristic has been investigated. In this section the general behavior of the curves, the breakdown voltage and the quenching resistance of the SiPMs are studied. All the IV curves shown, were taken at 20 °C. Further studies with different temperatures are planned and some IV measurements at lower temperatures were taken in the course of this thesis. Their results are published in [53].

Tab. 4.1: Mean values and standard deviations of the currents at different voltages for the non-irradiated wafer 1 SiPMs measured at 20 °C.

Voltage	-1.8 V	10 V	31 V	40 V
<I>	8.673 mA	2.814 pA	7.890 nA	272.051 nA
STD	1.072 mA	0.975 pA	1.389 nA	56.287 nA
STD	12.36 %	34.65 %	17.60 %	20.69 %

4.1.1 IV Curve Characteristics before Neutron Irradiation

To begin with, the IV curves of the non-irradiated samples are investigated. They are shown in Fig. 4.1. As it can be seen, the general behavior of the different sensors is the same. The samples W1-B2-S5, W1-B2-S6 and W1-B3-S5 show the greatest deviation in terms of the current. Their forward current is smaller and their reverse current is larger compared to the others. Tab. 4.1 shows the mean values of the current $< I >$ at different voltages and their standard deviation in ampere as well as in percent. It can be seen that, despite the fact that all the SiPMs are from the same wafer and the same production process, they differ up to 35 % in their current characteristics. Above breakdown, this spread reduces to a value of around 20 %. However, the spread of the breakdown voltage is very small. The absolute values are discussed in section 4.1.3.

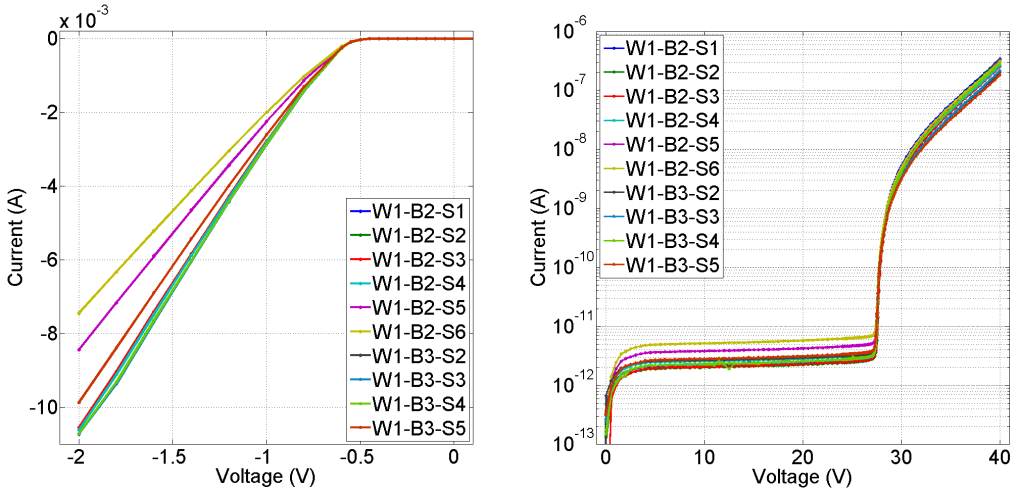

Fig. 4.1: Forward (left) and reverse (right) IV curves of the non-irradiated KETEK SiPMs without LED illumination.

To investigate possible systematic behaviors in the current measurement, hysteresis measurements have been performed, where the voltage was first ramped up from zero to its maximum value of 40 V and then down again to zero. Fig. 4.2 shows the ratios of the currents of the up-ramping and the down-ramping part of the IV measurement $\frac{I_{up}}{I_{down}}$ as a function of voltage. The sample investigated is W1-B3-S5, but all other SiPMs show a

comparable behavior.

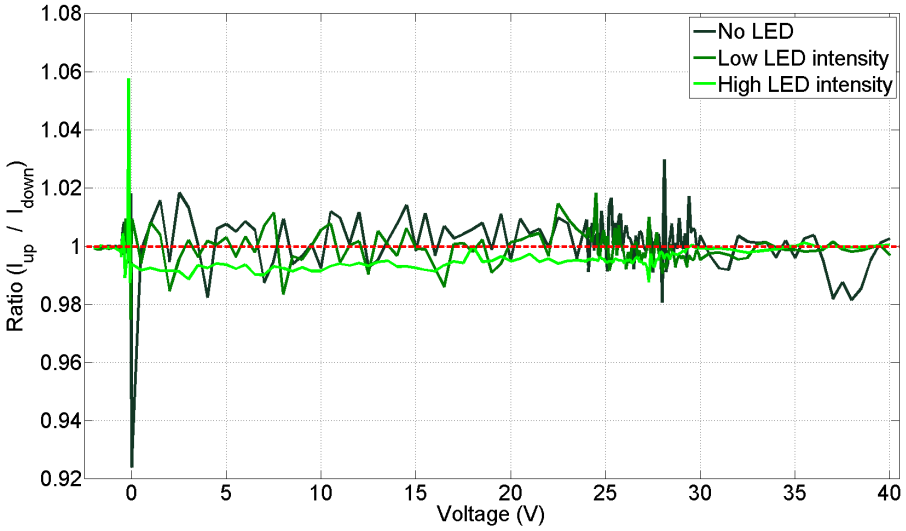

Fig. 4.2: Ratio of the up-ramping and the down-ramping IV measurements of a non-irradiated SiPM for the different light settings. The deviations mostly stay within 2 % and are biggest at 0 V and in the breakdown region.

The deviations of the ratios between up- and down-ramping are mostly smaller than 2 % and do not show a clear trend but vary randomly around 1. Bigger deviations up to 7 % are observed at 0 V, where they are expected due to the really small currents (tens of femtoampere, which is in the range of the setups noise). In the breakdown region bigger variations are also expected and observed: The voltage source is not perfect and a small deviation of the applied voltage causes a significant change due to the fast increase of the current.

What can also be seen is that for measurements with the low LED intensity the deviations become smaller. This has two explanations both connected to the higher current: Firstly, higher currents are easier to measure and thus the measurement device is more precise. Secondly, in the region below breakdown the measured currents are so small (several picoampere) that even people passing by could influence the measurement of the ammeter. With a higher measured current due to the LED illumination the influence of this effect diminished.

For the measurement with high LED intensity, the peak values of the deviations also decrease. However, a systematic shift is observable. Between 0 V and 35 V the ratio is always lower than 1, that is to say when the voltage is ramped down, the measured currents were constantly up to 1 % larger than the ones from ramping the voltage up.

This can not be explained by the SiPM heating up, since its temperature is ensured to stay constant via the cooling system. There is at least one factor changing throughout the measurement, the humidity. The measurements are done for humidities below 5 %, but because dry air is steadily pumped into the system, the humidity decreases slowly to values of around 0.5-1 %. In the bachelor thesis of Sonja Jaster-Merz [65] it has been ob-

served that for KETEK SiPMs the current in reverse direction decreases with decreasing humidity. More recent measurements on the other hand, show a different outcome: It has been observed that the current rises as the humidity declines. This behavior is still under investigation and the results will be included in the bachelor thesis of Svenja Sonder. The heating-up of the LED over time can be excluded as a possible explanation for the rising current, because heating up an LED lowers its brightness [66].
Nonetheless, the deviations of the currents are less than 1 % and comparable to the deviations from the measurements with no LED and low LED intensity. In order to investigate the hysteresis behavior, IV measurements with a simple high-ohmic resistor were done. These measurements also showed a hysteresis behavior for the resistor. However, it could be shown that by simply changing the settings of the ammeter, the hysteresis could be influenced. One setting caused the current measured while ramping up to be bigger than the current measured while ramping down and a different setting inverted this relation. Hence, a part of these small differences could be caused by the ammeter, although in that case they would be expected to occur for all measurements and not just the ones with high LED intensity. As a result, the behavior shown in Fig. 4.2 is not thought to be a hysteresis effect of the SiPM itself.

4.1.2 IV Curve Characteristics after Neutron Irradiation

Fig. 4.3 depicts the IV curves in forward and reverse direction of the irradiated sensors measured without LED illumination. For clarity, only one sample per fluence is shown. In Fig. 4.4 the IV curves with different LED settings for a SiPM irradiated at the lowest and for a SiPM irradiated at the highest fluence are shown.

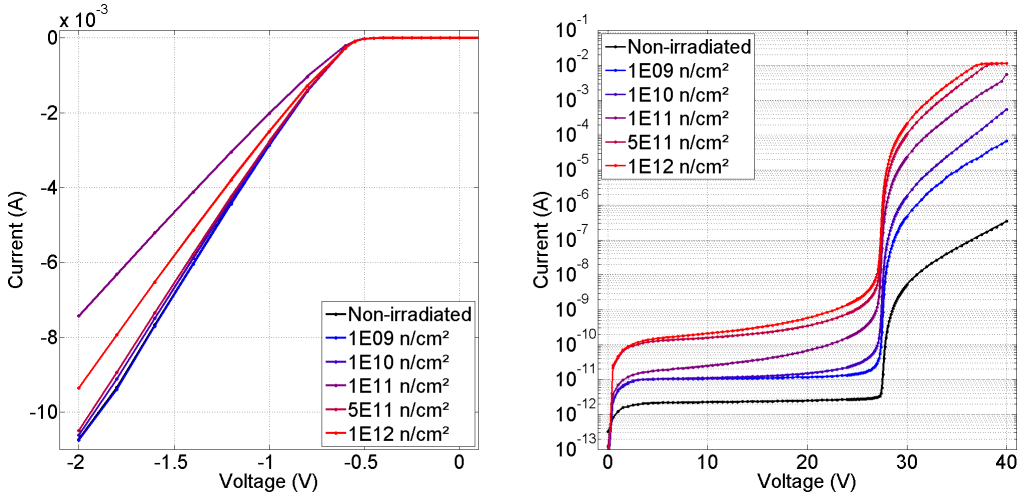

Fig. 4.3: Forward (left) and reverse (right) IV curves of the irradiated KETEK SiPMs without LED illumination. For each fluence one sample is shown. The non-irradiated sample is the same as the one of 1E09 n/cm^2.

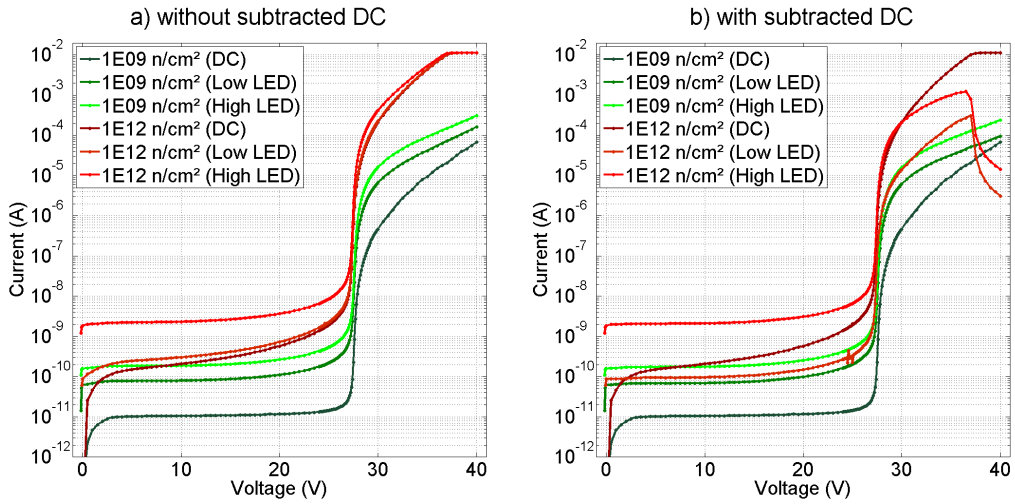

Fig. 4.4: Reverse IV curves for two SiPMs: one irradiated at the lowest and one irradiated at the highest fluence. The measurements of the three different light settings are plotted a) without subtracted dark current (DC) and b) with subtracted dark current.

Forward IV Curves

From the forward curves in Fig. 4.3, a fluence dependent change can not easily be extracted. The original behavior of the SiPMs dominates over the possible radiation induced changes. That is why in Fig. 4.5 three different samples that were irradiated with three different fluences are shown.

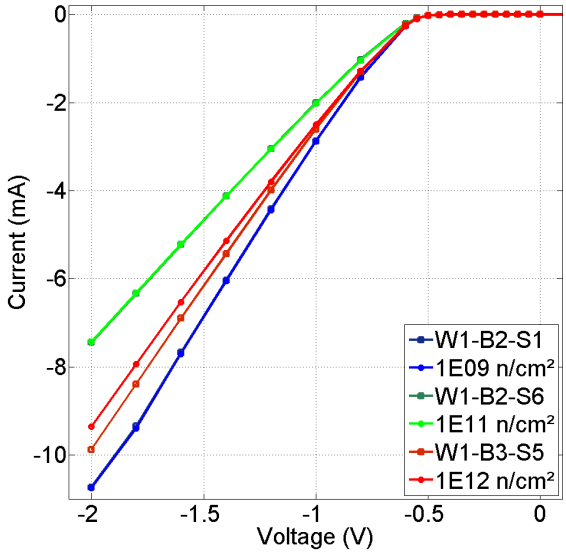

Fig. 4.5: Forward IV curves of three different KETEK SiPMs before (curves labeled with sample name) and after irradiation at three different fluences. For the highest fluence a change in the behavior of the current is observable.

It can be seen that for the lower fluences (10^9 and 10^{11} n/cm^2) the curves lie on top of each

Tab. 4.2: Ratios of the dark current at different voltages after and before neutron irradiation at different fluences. The measurements were taken at 20 °C. The breakdown voltages of the devices determined from the IV measurements is around 27.5 V (see Tab. 4.5).

Fluence	$\mathbf{10^9}$ **n/cm²**	$\mathbf{10^{10}}$ **n/cm²**	$\mathbf{10^{11}}$ **n/cm²**	$\mathbf{5 \cdot 10^{11}}$ **n/cm²**	$\mathbf{10^{12}}$ **n/cm²**
$\mathbf{I_\phi / I_0\,(10\ V)}$	4.7	4.9	11.1	70.2	92.6
$\mathbf{I_\phi / I_0\,(25\ V)}$	5.3	10.2	80.9	385.8	746.7
$\mathbf{I_\phi / I_0\,(31\ V)}$	99.9	396.2	5,117.9	23,062.4	45,718.5

other, that is to say, that there are no radiation induced changes. However, for the highest fluence (and also for the fluences of $5 \cdot 10^{11}$ n/cm^2 that is not shown in the picture) the current in forward direction decreases after irradiation. This might hint to a change of the effective doping and thus of the potential in the space charge region due to bulk damage. A second explanation might be a change of the depletion voltage for higher fluences. A change of the forward current can also be caused by a change of the quenching resistance. If this is the case, is investigated in section 4.1.3.

Reverse IV Curves

In the case of reverse biasing, a fluence dependent change can clearly be seen in Fig. 4.3. The non-irradiated sample shows the lowest current and with increasing fluence the measured current increases. In Tab. 4.2 the factors of increase for several voltages are shown.

For the highest irradiation steps, the current reaches values at which the limit of the voltage source is reached. As a consequence, the curves for $5 \cdot 10^{11}$ and 10^{12} n/cm^2 have a plateau at highest voltages. In the plot with subtracted dark current, this saturation leads to an unphysical drop for voltages above 36.5 V. An explanation for the increase of the dark current is the generation of charged defects and recombination centers due to the neutron irradiation. A higher fluence results in more of these defects, causing a higher current. Due to this high dark current, in the case of the highest fluence, the current ratio of 1:10 above breakdown aimed for when setting the LED voltage was not realizable. Still the LED voltage was increased compared to the measurements before irradiation, namely from values in the range of 2.3 V to values of about 2.5 V.
What can also be seen in Fig. 4.3 is, that for increasing fluences, the rise at the breakdown becomes less and less abrupt and that also for low reverse voltages the curve already starts to rise. However, judging from the curves the breakdown still seems to appear at the same voltage (for exact values see section 4.1.4). As stated in section 3.2.3, the abrupt rise of the curve indicates that the main contribution of the dark current does not pass

the avalanche zone. After irradiation this changes: The defects causing the increase of the leakage current are distributed throughout the whole pixel and thus the dark current also experiences multiplication.
Although the dark current increases by several orders of magnitude, the basic parameters of the SiPM like the pixel capacitance, quenching resistance, gain or PDE are not expected to be affected by neutron irradiation. This expectation is confirmed by Fig. 4.6. It shows the ratios of IV measurements with LED illumination after and before neutron irradiation with 10^{12} n/cm^2 normalized to 1 at 7.5 V.

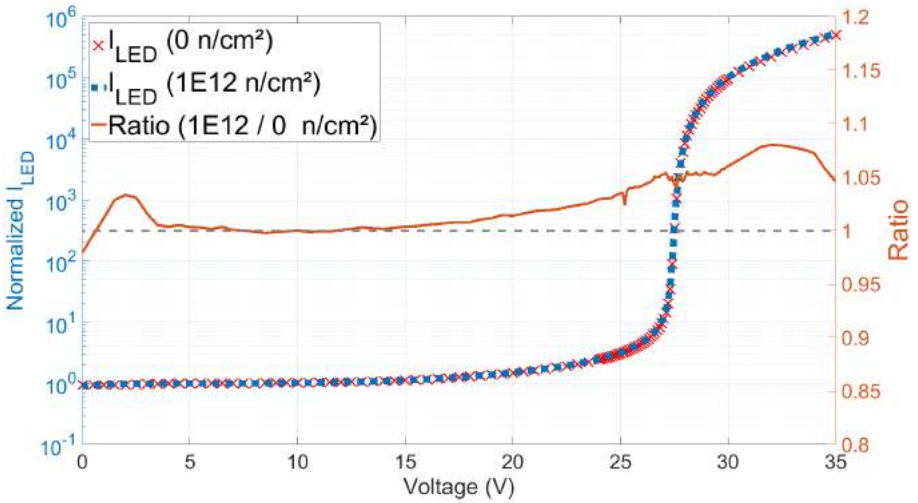

Fig. 4.6: IV curves of the measurements with LED for a SiPM before and after neutron irradiation (left scale). The values are normalized to 1 at 7.5 V. The ratio of the currents is also plotted (right scale). The values after irradiation are divided by the values before.

While the current rises by six orders of magnitude, the ratio of the currents varies by less than 7 %. It can be assumed that the number of photons generated by the LED as well as the number of photons generating electron-hole pairs n_γ above 7.5 V are constant [53]. Also for a low voltage like 7.5 V, which is 20 V lower than the breakdown voltage, the multiplication factor m is expected to be around 1. Under this assumption, normalizing the LED current to 1 at 7.5 V leads to the normalized LED current being equal to the multiplication factor for voltages below breakdown. Above breakdown, the normalized current is the product of the Geiger discharge probability P_{Gd}, the gain G and the correlated noise probability CNP. As a result of the curves very similar behavior, it can be said that, even for the highest fluence, the behavior of the LED current and thus the detection efficiency for photons barely changes due to neutron irradiation. For lower fluences, the changes are even smaller.
Fig. 4.7 shows the ratios $\frac{I_{dark}}{q_0 \cdot I_{LED,norm}}$ of the dark currents I_{dark} and the normalized LED currents $I_{LED,norm}$, where q_0 is the the elementary charge. For each fluence, the curve of one sample is shown. Above the breakdown voltage the ratio contains information about

the DCR, which is based on the assumption that the currents can be estimated by:

$$I_{dark} = q_0 \cdot DCR \cdot G_{dark} \cdot (1 + CNP) \qquad \text{for } V < V_{bd} \tag{4.1}$$

$$I_{LED} = q_0 \cdot n_\gamma \cdot m \qquad \text{for } V < V_{bd} \tag{4.2}$$

$$I_{LED} = q_0 \cdot n_\gamma \cdot P_{Gd,LED} \cdot G_{LED} \cdot (1 + CNP) \qquad \text{for } V > V_{bd} \tag{4.3}$$

$$I_{LED,norm} = \frac{I_{LED}}{I_{LED}(V_0)} = P_{Gd,LED} \cdot G_{LED} \cdot (1 + CNP) \qquad \text{for } V > V_{bd}\,, \tag{4.4}$$

where $V_0 = 7.5\,V \ll V_{bd}$ and $m(V_0) \approx 1$. Calculating the ratios of the dark current and the normalized LED current results in many factors canceling out:

$$\frac{I_{dark}}{I_{LED,norm}} = \frac{q_0 \cdot DCR \cdot G \cdot (1 + CNP)}{P_{Gd} \cdot G \cdot (1 + CNP)} = q_o \cdot \frac{DCR}{P_{Gd}} \tag{4.5}$$

The quantity of DCR^{IV} is now introduced as the following:

$$DCR^{IV} = \frac{I_{dark}}{I_{LED,norm} \cdot q_0} = \frac{DCR}{P_{Gd}} \tag{4.6}$$

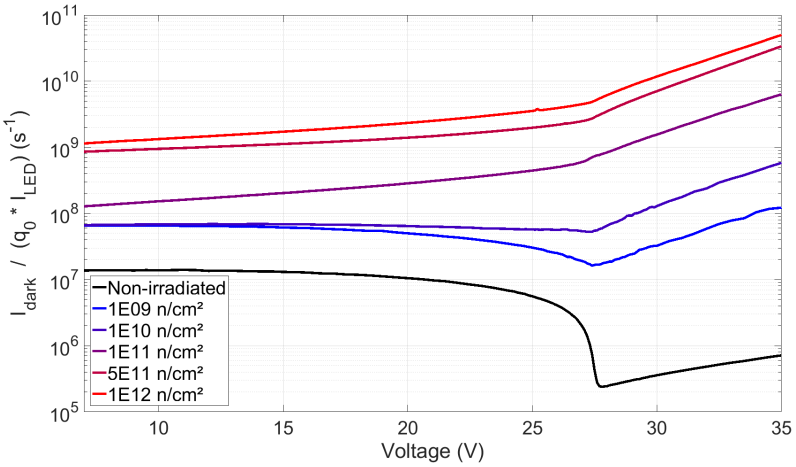

Fig. 4.7: The dark current divided by the LED current normalized at 7.5 V for SiPM irradiated at different fluences. Above breakdown the ratio is a measure of the SiPMs DCR and its Geiger discharge probability.

Compared to the QDC measurements, this method has the advantage that it also works for rates above $10^7 s^{-1}$ [53], where the standard method, of extracting the DCR from pulseheight spectra, fails. However, it should be kept in mind, that the value of DCR^{IV} still contains the Geiger discharge probability.

Nonetheless, the depicted behavior of the DCR matches the expectations. Firstly, the DCR increases with voltage and secondly, with increasing fluence the DCR reaches higher values. The values of DCR^{IV} start from 10^5 cps for the non-irradiated sensor, going up to values of 10^{10} cps for the highest irradiated sensor.

The values calculated for DCR^{IV} for three different excess voltages are noted in Tab. 4.3.

Tab. 4.3: Mean values of the dark count rates DCR^{IV} estimated from the IV curves of non-irradiated and irradiated SiPMs.

$\mathbf{\Phi(n/cm^2)}$	$\mathbf{DCR^{IV}@29.5V(cps)}$	$\mathbf{DCR^{IV}@32V(cps)}$	$\mathbf{DCR^{IV}@35V(cps)}$
0	$(246 \pm 5) \cdot 10^3$	$(376 \pm 8) \cdot 10^3$	$(568 \pm 11) \cdot 10^3$
10^9	$(191 \pm 4) \cdot 10^5$	$(395 \pm 8) \cdot 10^5$	$(851 \pm 17) \cdot 10^5$
10^{10}	$(134 \pm 3) \cdot 10^6$	$(288 \pm 6) \cdot 10^6$	$(677 \pm 14) \cdot 10^6$
10^{11}	$(128 \pm 3) \cdot 10^7$	$(271 \pm 5) \cdot 10^7$	$(606 \pm 12) \cdot 10^7$
$5 \cdot 10^{11}$	$(580 \pm 12) \cdot 10^7$	$(125 \pm 2) \cdot 10^8$	$(317 \pm 6) \cdot 10^8$
10^{12}	$(111 \pm 2) \cdot 10^8$	$(234 \pm 5) \cdot 10^8$	$(575 \pm 12) \cdot 10^8$

In the case of the non-irradiated SiPMs, the average of all the devices is noted. In the case of the irradiated SiPMs, the mean values of the two SiPMs irradiated at the same fluence are averaged[4].

For the lowest fluence, an increase by two orders of magnitude is observable. For higher fluences, the increase goes up to five orders of magnitude. However, the precision of this method is not yet verified. Compared to the QDC measurements, the values for single devices differ up to a factor of 5.5. This difference is contributed to the influence of the Geiger discharge probability P_{Gd}. Consequently, if one does not know P_{Gd}, this method rather provides a first estimation and it might be useful for rates above several MHz. The results will be compared to the ones of the QDC measurements in section 4.3.1.

4.1.3 Investigation of the Quenching Resistance

In Tab. 4.4 the different values of the quenching resistance, determined from the forward IV curves, are presented. The table presents the values R_{q0} before and $R_{q,i}$ after neutron irradiation at different fluences Φ. The ratios $\frac{R_{q,i}}{R_{q0}}$ of the extracted values are shown in Fig. 4.8. The errors are estimated, varying the voltage range of the fit.

While seven out of the ten SiPMs have quenching resistances of about 550 $\mathrm{k}\Omega$, three samples deviate from this value. W1-B2-S5, W1-B2-S6 and W1-B3-S5 all show values larger than the others. And comparing this to the results from section 4.1.1, these are also the SiPMs with deviating IV curves.
The table and the figure seem to confirm the suspicion that R_q has changed after irradiation. However, there are three leads that the change is not as drastic as depicted: Firstly, the large error bars indicate that the method is not very accurate. Secondly, the inverse slopes in the cases of the non-irradiated and the irradiated SiPMs are not constant, as it

[4]The SiPMs W1-B2-S5 and W1-B3-S6 were excluded because of their second breakdowns in the dark current measurement (see Fig 4.15).

Tab. 4.4: Quenching resistances of the SiPMs before R_{q0}^{IV} and after $R_{q,i}^{IV}$ neutron irradiation determined from the forward IV curves taken at 20 °C.

Sample	$\mathbf{\Phi(n/cm^2)}$	$\mathbf{R_{q0}^{IV}(k\Omega)}$	$\mathbf{R_{q,i}^{IV}(k\Omega)}$
W1-B2-S1	10^9	551.06 ± 12.57	548.45 ± 12.51
W1-B2-S2	10^9	551.88 ± 12.59	585.29 ± 13.35
W1-B2-S3	10^{10}	570.87 ± 13.02	569.85 ± 13.00
W1-B2-S4	10^{10}	565.42 ± 12.90	599.75 ± 13.68
W1-B2-S5	10^{11}	724.03 ± 16.52	725.56 ± 16.55
W1-B2-S6	10^{11}	823.70 ± 18.79	828.22 ± 18.89
W1-B3-S2	$5 \cdot 10^{11}$	552.61 ± 12.61	580.25 ± 13.24
W1-B3-S3	$5 \cdot 10^{11}$	550.59 ± 12.56	579.26 ± 13.21
W1-B3-S4	10^{12}	552.71 ± 12.61	596.35 ± 13.60
W1-B3-S5	10^{12}	616.26 ± 14.06	656.41 ± 14.97
Mean	/	609.92 ± 13.82	626.96 ± 14.30
STD	/	93.69	87.16

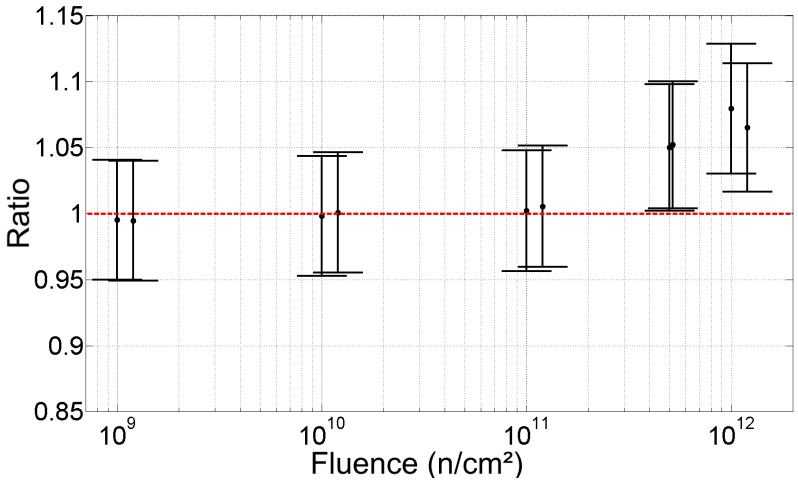

Fig. 4.8: Ratios of the quenching resistances extracted from the forward IV curve. The value after neutron irradiation is divided by the value from before.

can be seen in Fig. 4.9. Both of the curves behave similarly and both of them decrease with increasing forward bias. As already stated, the linear fit is not an optimal method to determine R_q. In addition to this, the change of R_q^{CV} determined from the CV-f measurements in section 4.2.1 is seriously smaller.

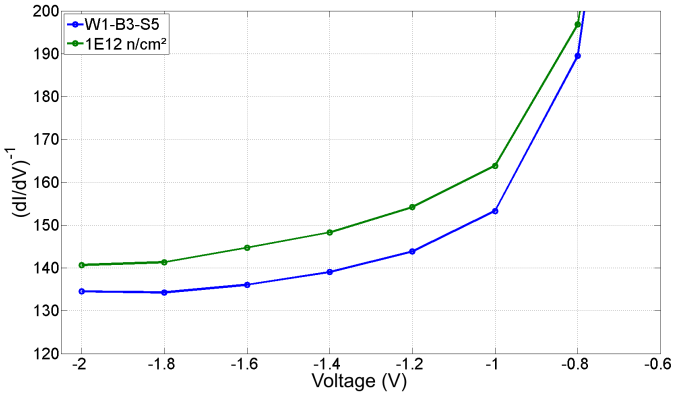

Fig. 4.9: Inverse slopes of a SiPM before and after neutron irradiation. The basic shape does not change. However, the irradiated sample shows higher values, which corresponds to a higher quenching resistance.

4.1.4 Investigation of the Breakdown Voltage

As seen in Fig. 4.3, the breakdown voltages of the SiPMs do not appear to have changed significantly after neutron irradiation. To confirm this assumption and determine possible minor changes of V_{bd}, the ILDs of the SiPMs are investigated.

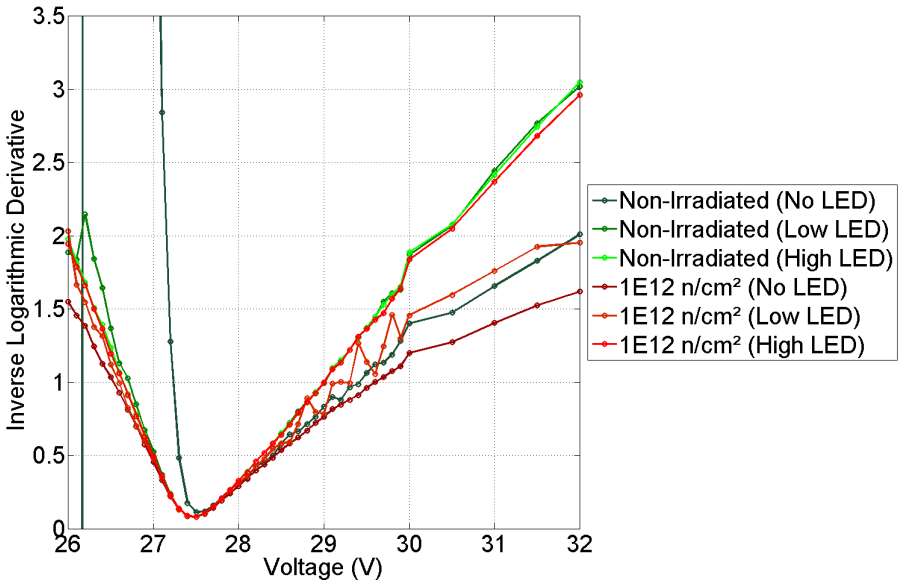

Fig. 4.10: Inverse logarithmic derivatives for three different light settings of a SiPM before and after neutron irradiation. The dark current is subtracted from the LED measurement values.

Fig. 4.10 shows the ILDs of the SiPM W1-B3-S4 for the three different light settings before and after irradiation.
Even at the highest fluence of 10^{12} n/cm^2, the ILD shows in general the same behavior as before. The curves of the irradiated sensor deviate after 0.5 V (low LED) or 1 V re-

spectively (high LED) in their slope from the non-irradiated one, but still five of the six curves share the same minimum. The only curve that has a different minimum, is the one of the non-irradiated sensor without LED and this curve is not used for determining the breakdown voltage V_{bd}. However, in the case of the irradiated samples, the curves exhibit a less stable behavior and several jumps. This increases the uncertainties of the ILD fits for the V_{bd} and factor n determination, although the most extreme jumps are excluded for the fitting procedure. Figures 4.11 to 4.13 show the results of the breakdown determination using the different methods explained in section 3.2.3. Each point in a plot represents one sample. The breakdown values after irradiation are subtracted from the values before irradiation and the errors are directly taken from the fits.

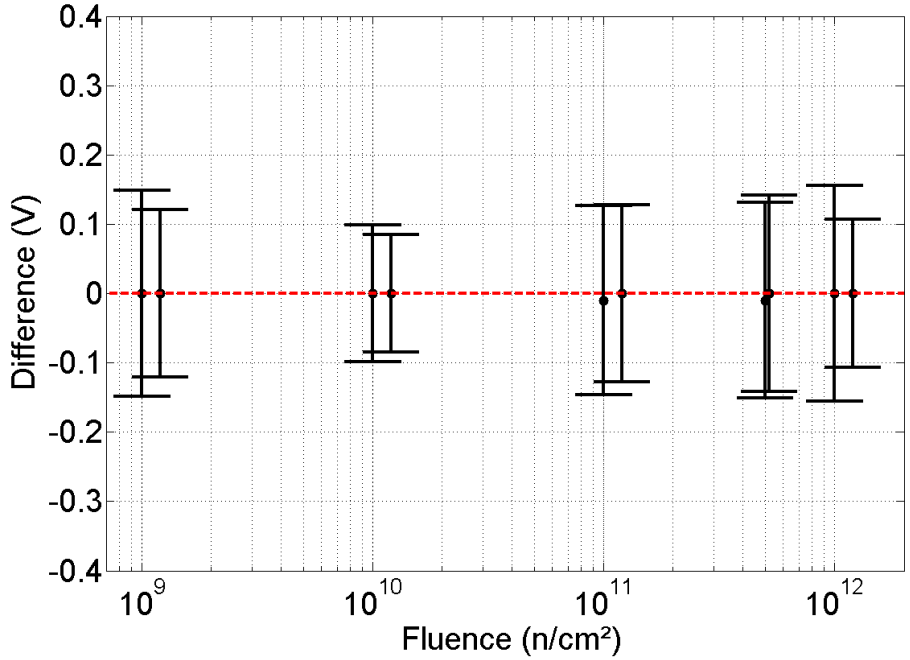

Fig. 4.11: Differences of V_{bd} for each SiPM before and after irradiation as a function of fluence. The values are calculated by determining the minimum of a parabola $(V - V_{bd})^2$ fitted through the minimum of the ILD. For clarity, the SiPMs irradiated at the same fluence are plotted offset.

All three figures show that within the uncertainties the breakdown voltage does not change. Only for the quadratic fit (Fig. 4.13) the samples irradiated at 10^{12} n/cm^2 indicate a definite increase of the breakdown voltage of about 100 mV. However, this change does neither appear for the linear fit (Fig. 4.12) nor for the fit of the ILDs parabola minimum (Fig. 4.11). Furthermore, this change is not seen in the IV curves of the SiPMs. Also the other implied changes of the SiPMs irradiated at 10^{10} n/cm^2 or 10^{11} n/cm^2 are not observed in the IV curves. As a consequence, the quadratic fit appears to be the least suitable to extract V_{bd} after neutron irradiation.
This has several reasons, the first one being the already mentioned deviations in the ILD after irradiation. Additionally, the parabolic shape of the ILD after irradiation is lost for

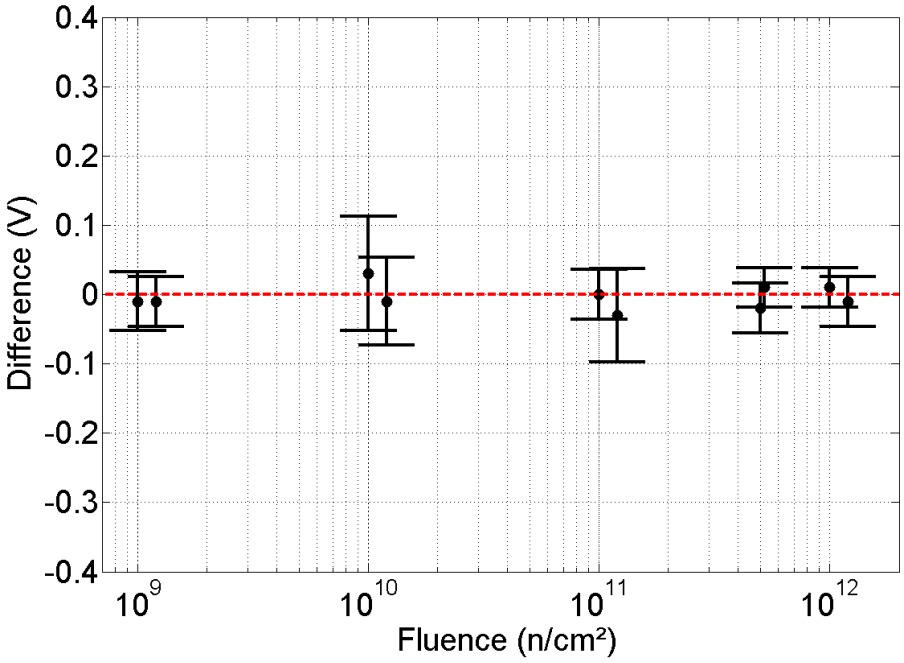

Fig. 4.12: Differences of V_{bd} for each SiPM before and after irradiation as a function of fluence. The values are calculated by applying the linear fit $ILD(V) = (V - V_{bd}/n)$ to the ILD above breakdown. For clarity, the SiPMs irradiated at the same fluence are plotted offset.

some of the samples. Lastly, some of the SiPMs exhibited a sharp rise in their current after the first breakdown, similar to a second breakdown. These rises appear predominantly in the measurements without LED but for one sample (W1-B2-S5) also in the measurements with LED. The rises are shown in Fig. 4.14.

This phenomenon is not yet understood. A possible explanation is the accumulation of conducting glue at the SiPM surface that connects some of the pixels and, due to its smaller resistance, interferes with the quenching process causing ever-firing pixels. As explained in section 3.1, the SiPMs are glued onto ceramics to simplify the measurements. In order to have them irradiated, the SiPMs needed to be taken off their ceramics. This was done by covering them in ethanol and putting them into a supersonic bath. Even though they were thoroughly cleaned (also again after the irradiation) some SiPMs showed stains on their surface afterwards. However, not all the SiPMs with stains exhibit the second breakdown behavior. Fig. 4.15 shows microscope pictures of a normally functioning SiPM (W1-B2-S1) and the three malfunctioning SiPMs. All the SiPMs show stains on their surface and contrary to expectations, the normally functioning SiPM even has the most stains. Hence, it is difficult to directly link the stains to the second breakdowns.

The abrupt rises negatively influence the shape of the ILD, because to determine V_{bd}, the dark current is subtracted from the LED measurements before taking the ILD. As a result, the calculated values for V_{bd} as well as for n for the irradiated samples have larger errors

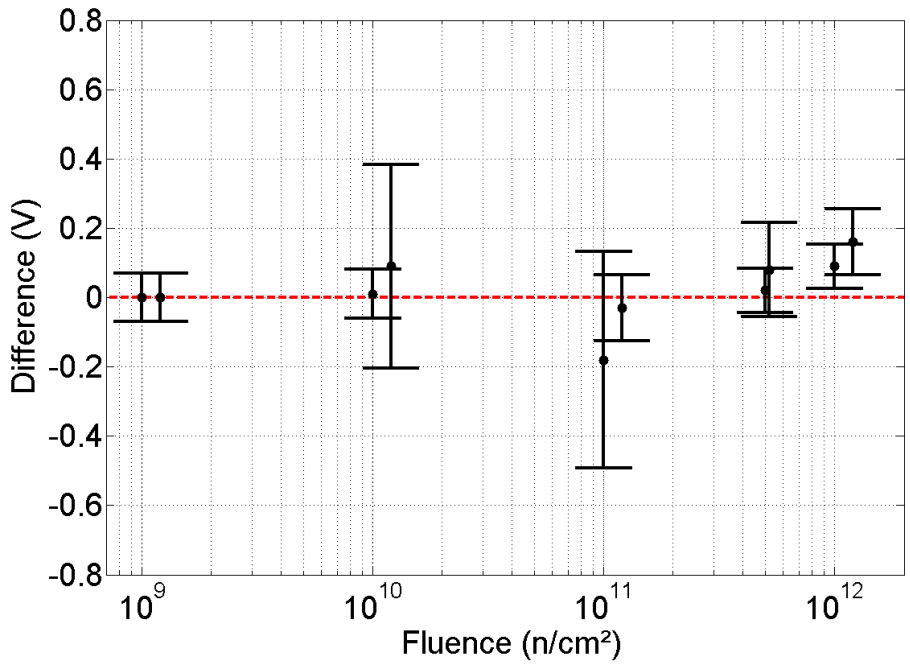

Fig. 4.13: Differences of V_{bd} for each SiPM before and after irradiation as a function of fluence. The values are calculated by applying the quadratic fit $ILD(V) = (V - V_{bd}/n) + b \cdot (V - V_{bd})^2$ to the ILD above breakdown. For clarity, the SiPMs irradiated at the same fluence are plotted offset.

than those for the non-irradiated samples.

Especially the quadratic fit ceases to work properly because of its larger fitting range. The method using the minimum of the parabola is least affected by the second breakdowns. However, the method is in itself less accurate than the linear fit of the ILD above breakdown and thus shows larger error bars. While in case of the parabola method, the errors, concerning the difference of V_{bd} before and after irradiation, range up to 200 mV, they only range up to 100 mV in the case of the linear fit method.

To sum up, the calculated breakdown voltage of the SiPMs does not change after neutron irradiation within at maximum 100 mV. The most accurate method to determine V_{bd} is the linear fit of the ILD. The method least affected by changes of the ILDs curve shape, is the parabola method and the quadratic fit ceases to work after irradiation for half of the SiPMs. Within the fit and measurement uncertainties all of the calculated values for the breakdown voltage agree.

The absolute values of V_{bd} are shown in Tab. 4.5. For reasons of space, the fluence values have been omitted. They can be read from the previous and following tables. V_{bd0} stands for the value before irradiation, $V_{bd,i}$ for the value afterwards. The different methods are marked as a superscript: min represents the method using the minimum of the parabola, lin corresponds to the linear fit and $quad$ to the quadratic fit.

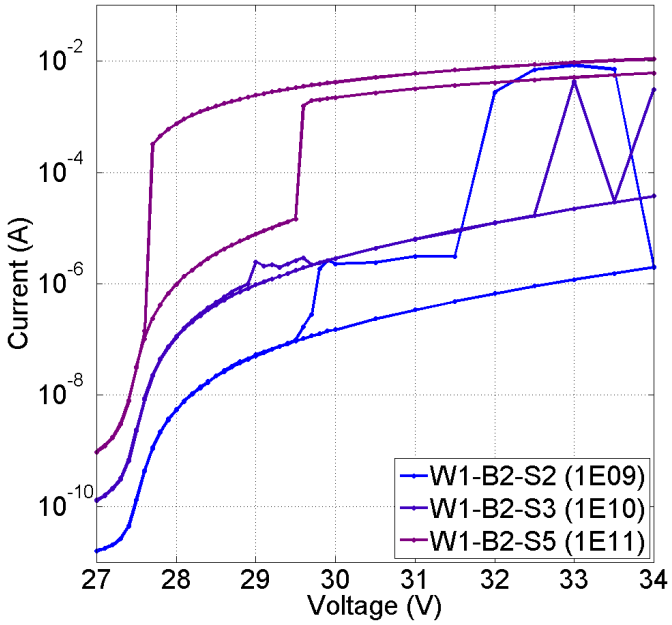

Fig. 4.14: IV curves taken withoud LED illumination of the three SiPMs that exhibit a different behavior above breakdown. In the case of sample 2 and 3, the jumps appear only when ramping the voltage up. Sample 5 shows the jumps also when ramping the voltage down.

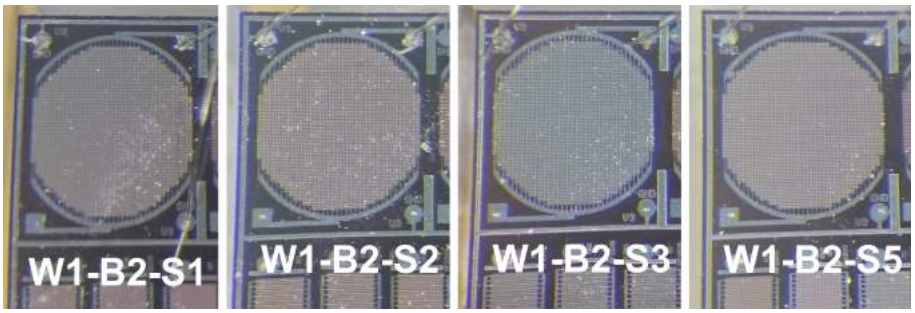

Fig. 4.15: Microscope pictures of four different SiPMs. W1-B2-S1 has the most stains on its surface, but shows no jumps in its IV measurements, unlike the three other samples that have less stains on their surface.

4.1.5 Investigation of the Factor n

The factor n, appearing in the ILD of the reverse current, contains information about the gain, PDE and the cross-talk/afterpulse probability. Therefore, it is of interest, if or how this factor changes due to neutron irradiation. If the SiPMs, despite the increase of the dark current, still function, only minor changes of n are expected. In the following two figures, the ratios $\frac{n_i}{n_0}$ of the factor before n_0 and after n_i neutron irradiated are plotted as a function of fluence. Fig. 4.16 shows the results gained from the linear fit of the ILD. Fig. 4.17 shows the results gained from the quadratic fit. Each SiPM is represented by a data point and the errors are directly taken from the fits.

Tab. 4.5: Calculated values of the breakdown voltage before V_{bd0} and after neutron irradiation $V_{bd,i}$ determined from the IV curves taken at 20 °C. Three different methods were applied to calculate the values. The errors are taken directly from the fit. Additional systematic errors result from the calibration of the voltage source (0.02 V) and changing the fitting range (0.03 V).

Sample	$\mathbf{V_{bd0}^{min}\,(V)}$	$\mathbf{V_{bd,i}^{min}\,(V)}$	$\mathbf{V_{bd0}^{lin}\,(V)}$	$\mathbf{V_{bd,i}^{lin}\,(V)}$	$\mathbf{V_{bd0}^{quad}\,(V)}$	$\mathbf{V_{bd,i}^{quad}\,(V)}$
W1-B2-S1	27.61 ± 0.11	27.61 ± 0.10	27.64 ± 0.03	27.65 ± 0.03	27.71 ± 0.05	27.71 ± 0.05
W1-B2-S2	27.55 ± 0.08	27.55 ± 0.09	27.61 ± 0.03	27.62 ± 0.02	27.69 ± 0.05	27.69 ± 0.05
W1-B2-S3	27.51 ± 0.07	27.51 ± 0.07	27.59 ± 0.02	27.56 ± 0.08	27.67 ± 0.05	27.66 ± 0.05
W1-B2-S4	27.48 ± 0.06	27.48 ± 0.06	27.57 ± 0.02	27.58 ± 0.06	27.65 ± 0.05	27.56 ± 0.29
W1-B2-S5	27.50 ± 0.11	27.51 ± 0.08	27.55 ± 0.02	27.55 ± 0.03	27.63 ± 0.04	27.81 ± 0.31
W1-B2-S6	27.45 ± 0.09	27.45 ± 0.09	27.53 ± 0.03	27.56 ± 0.06	27.60 ± 0.05	27.63 ± 0.08
W1-B3-S2	27.45 ± 0.10	27.46 ± 0.10	27.53 ± 0.02	27.55 ± 0.03	27.61 ± 0.04	27.59 ± 0.05
W1-B3-S3	27.47 ± 0.10	27.47 ± 0.10	27.54 ± 0.02	27.53 ± 0.02	27.62 ± 0.04	27.54 ± 0.13
W1-B3-S4	27.50 ± 0.11	27.50 ± 0.11	27.55 ± 0.02	27.54 ± 0.02	27.63 ± 0.05	27.54 ± 0.04
W1-B3-S5	27.41 ± 0.07	27.41 ± 0.08	27.50 ± 0.03	27.51 ± 0.02	27.59 ± 0.05	27.43 ± 0.08
Mean	27.49 ± 0.09	27.50 ± 0.09	27.56 ± 0.02	27.57 ± 0.04	27.64 ± 0.05	27.62 ± 0.11
STD	0.05	0.05	0.04	0.04	0.04	0.10

According to Fig. 4.16, there is no change of the factor within the fits uncertainties. This corresponds to the fact that the shape of the IV curves with LED illumination has not changed (see Fig. 4.6) and confirms it again. That is to say, although the dark current increases significantly due to the neutron irradiation, the performance parameters like gain, PDE, cross-talk and afterpulse probability stay the same within 7 %, even for the highest fluences. The SiPM still works as a good light detector. It might be that the parameters changes cancel each other out perfectly, but this is not expected.
On the other hand, in Fig. 4.17 four samples, two of the highest irradiation step and one of each of the two steps below, show a deviation. However, as stated in the previous section, the quadratic fit does not work properly for the irradiated samples. Consequently, these results are not as reliable at the results from the linear fit and should not be over-interpreted.
The absolute values of n are given in Tab. 4.6. The indices and superscripts follow the same convention as in Tab. 4.5, with the difference that n can not be extracted from the method using the minimum of the parabola. Like in the case of the V_{bd} determination, the values determined by the linear fit are thought to be the most precise.

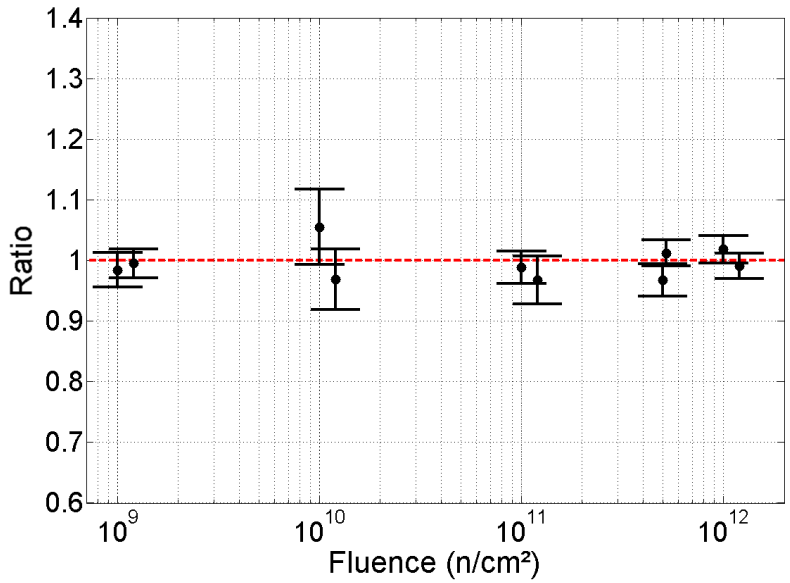

Fig. 4.16: Ratios of the factor n after/before neutron irradiation. The values for n are extracted applying $ILD(V) = (V - V_{bd}/n)$ to the ILD above breakdown. For clarity, the SiPMs irradiated at the same fluence are plotted offset.

4.2 Capacitance-Voltage-Frequency Measurements

The second main part of the analysis covers the CV-f measurements. In Fig. 4.18 the series resistances and the parallel capacitances for a non-irradiated and five irradiated SiPMs are shown. All the CV-f measurements were taken at 25 °C. In addition to the data points, the model curves, based on the equivalent circuit diagram from Fig. 3.18 including the series inductance, are plotted. Each fluence is represented once. It can be seen that the general curve shape is preserved and that the model matches the data. Only for lower frequencies there are larger deviations visible. In the case of R_s the deviations just occur for the first frequency and looking at Fig. 3.14, one can see that the series resistance measurement for the lowest frequency is also the least stable one with a lot of jumps in the curve. As a result, the deviations at 100 Hz should not be over-interpreted.
On the other hand, the measured parallel capacitances show deviations up to 1 kHz from the model curve. This can be explained with the contributions of C_{par} and C_q that both have been set to zero for the model calculations.

In the case of the series resistances, a clear trend for the different irradiation steps can be seen. Before reaching the plateau, the curves are shifted to higher values of R_s and this shift increases with fluence. Also the plateau is reached for higher frequencies with increasing fluence. The plateaus however, do not exhibit significant differences from each other due to the irradiation. The SiPM that has been irradiated to 10^{11} n/cm^2 (W1-B2-S6) shows a higher R_s than the others. However, this is not caused by radiation damages, instead the SiPM already had a higher value of R_s / R_q before the irradiation with neutrons

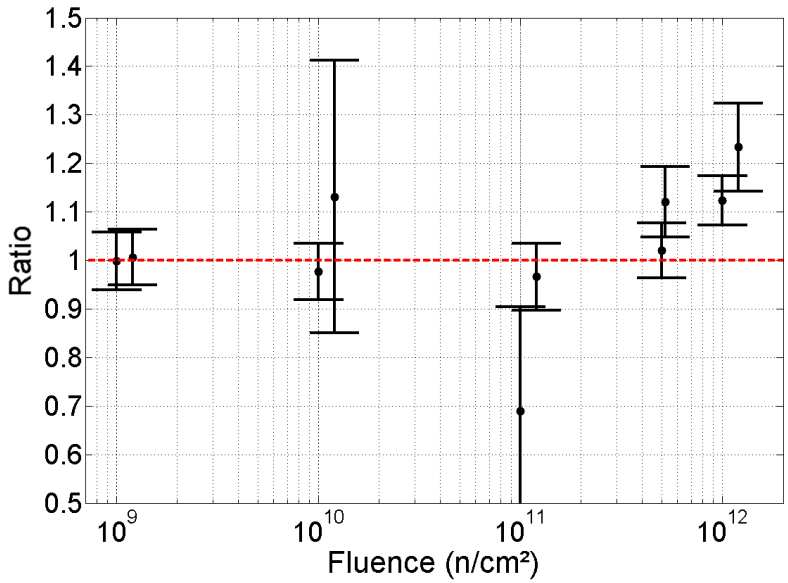

Fig. 4.17: Ratios of the factor n after/before neutron irradiation. The values for n are extracted applying the quadratic fit $ILD(V) = (V - V_{bd}/n) + b \cdot (V - V_{bd})^2$ to the ILD above breakdown. Larger errors appear due to the unstable behavior of the ILD for larger excess voltages. For clarity, the SiPMs irradiated at the same fluence are plotted offset.

(see Tab. 4.7). The increase of R_s at low frequencies can be explained with a decrease of the parasitic resistance R_{par}, which corresponds to an increase of the dark current.

4.2.1 Investigation of the Quenching Resistance and Parasitic Resistance

Fig. 4.19 shows the ratios R_i/R_0 of the parasitic and quenching resistances for each SiPM before R_0 and after R_i neutron irradiation. The absolute values for the single devices are shown in Tab. 4.7. The errors are estimated from the accuracy of the LCR meter, deviations in temperature and the difference from choosing a different value of the frequency or voltage for extraction of the value. While R_q is relatively stable, R_{par} has higher uncertainties, the biggest influence being the choice of the frequency.

It should be mentioned that, due to some miscommunication, for three of the SiPMs there were no CV-f measurements taken before irradiation and thus no values for R_{par0} and R_{q0} can be determined. The same applies for the determination of C_{pix0} and the series inductance L_{s0} in the subsequent sections.
However, before irradiation all the devices have nearly the same value of R_{par0} and differ by less than a percent. As a result of this uniformity, the missing measurement values and their errors were replaced with the mean values, in order to fill the gaps in Tab. 4.7. In Fig. 4.19, these values are represented by the blue markers. After irradiation, the mean value of $R_{par,i}$ is significantly lower and in terms of the standard deviation the SiPMs

Tab. 4.6: Calculated values for n determined from the IV curves taken at 20 °C. Two different methods were applied to calculate the values. The errors are taken directly from the fit.

Sample	$\mathbf{\Phi(n/cm^2)}$	$\mathbf{n_0^{lin}}$	$\mathbf{n_i^{lin}}$	$\mathbf{n_0^{quad}}$	$\mathbf{n_i^{quad}}$
W1-B2-S1	10^9	1.440 ± 0.028	1.417 ± 0.030	1.283 ± 0.050	1.281 ± 0.057
W1-B2-S2	10^9	1.441 ± 0.025	1.434 ± 0.024	1.272 ± 0.050	1.280 ± 0.053
W1-B2-S3	10^{10}	1.437 ± 0.022	1.516 ± 0.086	1.272 ± 0.047	1.242 ± 0.058
W1-B2-S4	10^{10}	1.437 ± 0.022	1.392 ± 0.069	1.266 ± 0.047	1.432 ± 0.352
W1-B2-S5	10^{11}	1.432 ± 0.021	1.416 ± 0.032	1.262 ± 0.045	0.870 ± 0.269
W1-B2-S6	10^{11}	1.422 ± 0.022	1.376 ± 0.052	1.268 ± 0.046	1.225 ± 0.076
W1-B3-S2	$5 \cdot 10^{11}$	1.423 ± 0.021	1.377 ± 0.032	1.258 ± 0.045	1.283 ± 0.054
W1-B3-S3	$5 \cdot 10^{11}$	1.416 ± 0.022	1.433 ± 0.020	1.252 ± 0.044	1.403 ± 0.077
W1-B3-S4	10^{12}	1.424 ± 0.023	1.450 ± 0.022	1.265 ± 0.047	1.421 ± 0.038
W1-B3-S5	10^{12}	1.419 ± 0.021	1.406 ± 0.021	1.252 ± 0.046	1.544 ± 0.099
Mean	/	1.429 ± 0.023	1.422 ± 0.039	1.265 ± 0.047	1.298 ± 0.113
STD	/	0.009	0.039	0.09	0.172

Tab. 4.7: Parasitic and quenching resistances of the SiPMs before R_{par0}^{CV}, R_{q0}^{CV} and after $R_{par,i}^{CV}$, R_{qi}^{CV} neutron irradiation determined from the CV-f measurements done at 25 °C. The applied voltage at which the data is extracted is 26.5 V. R_{par} is extracted from R_P at 700 Hz and R_q from R_s at 700 kHz.

Sample	$\mathbf{\Phi(n/cm^2)}$	$\mathbf{R_{par0}(M\Omega)}$	$\mathbf{R_{par,i}(M\Omega)}$	$\mathbf{R_{q0}^{CV}(k\Omega)}$	$\mathbf{R_{q,i}^{CV}(k\Omega)}$
W1-B2-S1	10^9	/	677.77 ± 16.95	/	528.09 ± 2.64
W1-B2-S2	10^9	/	1102.88 ± 27.58	/	529.86 ± 2.65
W1-B2-S3	10^{10}	1059.06 ± 26.78	459.48 ± 11.49	534.09 ± 2.67	540.78 ± 2.70
W1-B2-S4	10^{10}	/	581.30 ± 14.53	/	535.20 ± 2.68
W1-B2-S5	10^{11}	1072.50 ± 26.83	491.04 ± 12.28	644.40 ± 3.22	639.38 ± 3.20
W1-B2-S6	10^{11}	1070.30 ± 26.75	498.25 ± 12.46	709.54 ± 3.55	703.78 ± 3.52
W1-B3-S2	$5 \cdot 10^{11}$	1051.57 ± 26.30	185.64 ± 4.64	519.25 ± 2.60	528.79 ± 2.64
W1-B3-S3	$5 \cdot 10^{11}$	1073.60 ± 26.85	234.49 ± 5.86	529.80 ± 2.65	529.83 ± 2.65
W1-B3-S4	10^{12}	1057.67 ± 26.45	123.75 ± 3.10	521.96 ± 2.61	529.65 ± 2.65
W1-B3-S5	10^{12}	1071.09 ± 26.78	97.88 ± 2.44	572.07 ± 2.86	589.53 ± 2.95
Mean	/	1065.28 ± 26.68	445.26 ± 11.13	575.87 ± 2.88	565.49 ± 2.83
STD	/	8.75	306.62	73.65	60.80

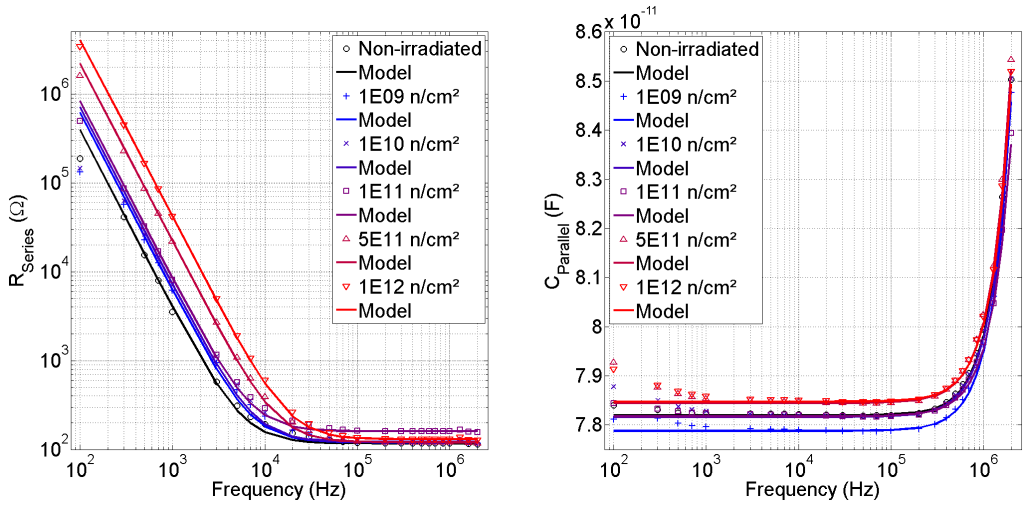

Fig. 4.18: Series resistances (left) and parallel capacitances (right) as a function of frequency for KETEK SiPMs at different irradiation steps. The applied voltage at which the data is extracted is 26.5 V.

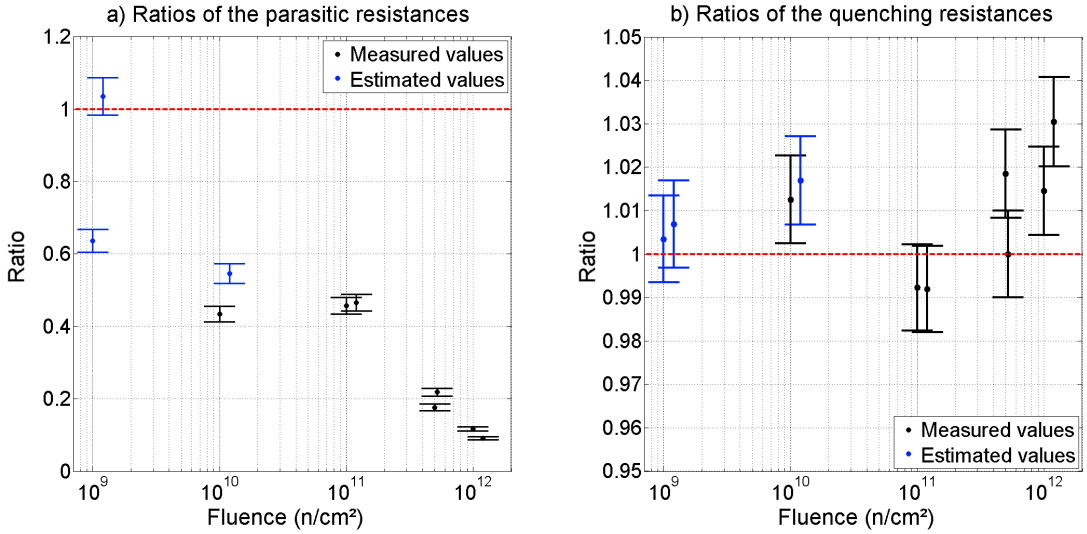

Fig. 4.19: The ratios of a) R_{par} and b) R_q after/before neutron irradiation extracted from the CV-f measurements. For clarity, the SiPMs irradiated at the same fluence are plotted offset. Blue markers are partly based on values that had to be estimated due to missing measurements.

differ by 68.86 %.

It can be seen that the parasitic resistance of the devices seriously decreases. For the highest irradiation steps, the values after irradiation are just a tenth of the original ones. Unfortunately, the missing CV-f measurements make it hard to completely interpret the results. The second sample at 10^9 n/cm^2 could be an outlier, because for the higher fluences, R_{par} steadily decreases. Maybe this sample showed a much higher value for R_{par} before irradiation, although this is not expected. Nevertheless, the predicted decrease of the parasitic resistance with increasing fluence, that showed in the increase of the dark

current in the IV measurements, could be confirmed with the CV-f measurements.

In terms of R_{q0}^{CV} three samples exhibit values significantly higher than the others which is compatible with the results of R_{q0}^{IV}. The other SiPMs W1-B2-S3, W1-B3-S2, W1-B3-S3 and W1-B3-S4 have very similar values. From the IV curves and the extraction of R_{q0}^{IV}, one can tell that the samples missing CV-f measurements before irradiation behave similar to these four samples. Thus, to fill the gaps in Tab. 4.7 their mean values are used to calculate the ratios plotted in Fig. 4.19.
In the right graph of Fig. 4.19, similar to the IV analysis, a change of R_q is noticeable. However, the change as well as the errors are smaller. For the IV analysis, errors of about $\pm$ 5 % are observed, whereas for the CV-f analysis the errors are about $\pm$ 1 %. Also the increase of R_q^{IV} for the highest fluence is about 10 % and for R_q^{CV} only 3 %. Additionally, the analysis of the IV curves gives results up to 10 % higher than the values of the CV-f analysis.
To conclude, the CV-f results are interpreted to be the more precise ones also because of the wrong assumption of a linear behavior of the forward IV curves. The quenching resistances of the SiPMs stay constant within 1 %, which is also the magnitude of the error, for fluences up to 10^{11} n/cm^2. For the fluence of 10^{12} n/cm^2 the values increase up to 3 %.

4.2.2 Investigation of the Pixel Capacitance

Fig. 4.20 shows the ratios the pixel capacitance before and after neutron irradiation. Again, the values calculated after irradiation are divided by the values extracted before irradiation. The absolute values are shown in Tab. 4.8.

From previous studies, it is expected that neutron irradiation does not cause any significant changes in C_{pix}. However, Fig. 4.20 implies something else: There is a systematic decrease of approximately 1.5 % in C_{pix} for every SiPM after irradiation. Since this increase is independent of the fluence, the change is expected to origin from something else than radiation damages. A possible explanation is that the measurements were done using a different setup.
In the laboratory there are two setups available for the IV and CV-f measurements that in principal are identical to each other, but of course do not have the exact same properties. Unfortunately, it has not been documented at which setup the first measurements were done. Additionally, the old measurements were done a year before the new CV-f measurements with the irradiated sensors which also reduces the comparability of the measurements; although C_p is not expected to change over time.
For comparison, the reference sample W1-B3-S1, that has not been irradiated, has been measured again. Fig. 4.21 shows the two different CV-f measurements that should in

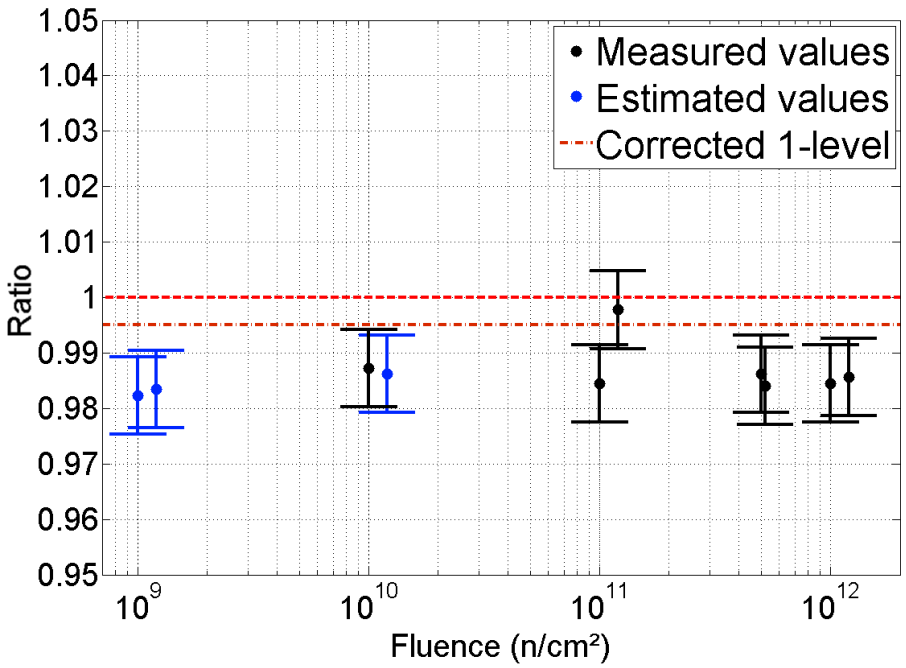

Fig. 4.20: The ratios of C_{pix} after/before neutron irradiation extracted from the CV-f measurements. Blue markers are partly based on values that had to be estimated due to missing measurements. The dark red line is a corrected 1-level, necessary because of systematic errors of the CV-f measurements taken at a different time. For clarity, the SiPMs irradiated at the same fluence are plotted offset.

principal be the same. However, it can be seen that the new measurement of C_p gives higher values than the old one. The measured values of C_p differ by 0.5 %. To correct for this systematic shift, a corrected 1-level is added to Fig. 4.20 (dark red line).

Similar to the parasitic resistances, the values for C_{pix0} hardly differ for the single SiPMs. Again the mean values of C_{pix0} and the corresponding errors are used to produce the blue marked points in Fig. 4.20. After neutron irradiation, the mean value of $C_{pix,i}$ is slightly lower. The pixel capacitances have declined by around 1 % which, however is also the uncertainty of the calculated values.

4.2.3 Investigation of the Recharge Time

Combining the results showed in tables 4.7 and 4.8, the recharge time $\tau_r = R_q \cdot C_{pix}$ can be calculated. The typical recharge time for this type of SiPM is around 10-12 ns. The results of this analysis is shown in Tab. 4.9.

Most of the values of τ_r do not change within their uncertainties. The only deviation larger than the uncertainty is observed for W1-B2-S5 and the change corresponds to an increase of τ_r by (2.3 $\pm$ 2.0) %.

From the signal shapes of the SiPMs (See Fig. 3.25) values for τ_r between 12 and 15 ns

Tab. 4.8: Pixel Capacitances of the SiPMs before C_{pix0} and after $C_{pix,i}$ neutron irradiation determined from the CV-f measurements done at 25 °C. The applied voltage at which the data is extracted is 26.5 V. C_{pix} is extracted from C_p at 30 kHz.

Sample	$\mathbf{\Phi(n/cm^2)}$	$\mathbf{C_{pix0}(fF)}$	$\mathbf{C_{pix,i}(fF)}$
W1-B2-S1	10^9	/	17.764 ± 0.888
W1-B2-S2	10^9	/	17.777 ± 0.889
W1-B2-S3	10^{10}	18.052 ± 0.903	17.822 ± 0.891
W1-B2-S4	10^{10}	/	17.829 ± 0.892
W1-B2-S5	10^{11}	18.102 ± 0.905	17.817 ± 0.891
W1-B2-S6	10^{11}	17.873 ± 0.894	17.832 ± 0.892
W1-B3-S2	$5 \cdot 10^{11}$	18.137 ± 0.907	17.894 ± 0.895
W1-B3-S3	$5 \cdot 10^{11}$	18.147 ± 0.908	17.859 ± 0.893
W1-B3-S4	10^{12}	18.085 ± 0.905	17.812 ± 0.891
W1-B3-S5	10^{12}	18.160 ± 0.908	17.900 ± 0.895
Mean	/	18.080 ± 0.904	17.830 ± 0.892
STD	/	0.100	0.044

Tab. 4.9: Recharge times of the SiPMs before τ_{r0} and after $\tau_{r,i}$ neutron irradiation determined from the CV-f measurements done at 25 °C. The applied voltage at which the data is extracted is 26.5 V.

Sample	$\mathbf{\Phi(n/cm^2)}$	$\tau_{\mathbf{r0}}(\mathbf{ns})$	$\tau_{\mathbf{r,i}}(\mathbf{ns})$	$\mathbf{\Delta}\tau_{\mathbf{r}}(ns)$
W1-B2-S1	10^9	/	9.38 ± 0.09	/
W1-B2-S2	10^9	/	9.42 ± 0.09	/
W1-B2-S3	10^{10}	9.64 ± 0.10	9.64 ± 0.10	0.00 ± 0.20
W1-B2-S4	10^{10}	/	9.54 ± 0.10	/
W1-B2-S5	10^{11}	11.66 ± 0.12	11.39 ± 0.11	0.27 ± 0.23
W1-B2-S6	10^{11}	12.68 ± 0.13	12.55 ± 0.13	0.13 ± 0.26
W1-B3-S2	$5 \cdot 10^{11}$	9.42 ± 0.09	9.46 ± 0.09	-0.04 ± 0.18
W1-B3-S3	$5 \cdot 10^{11}$	9.62 ± 0.10	9.46 ± 0.09	0.16 ± 0.19
W1-B3-S4	10^{12}	9.44 ± 0.09	9.43 ± 0.09	0.01 ± 0.18
W1-B3-S5	10^{12}	10.39 ± 0.10	10.55 ± 0.11	-0.16 ± 0.21
Mean	/	10.41 ± 0.10	10.08 ± 0.10	0.05 ± 0.21
STD	/	1.28	1.09	/

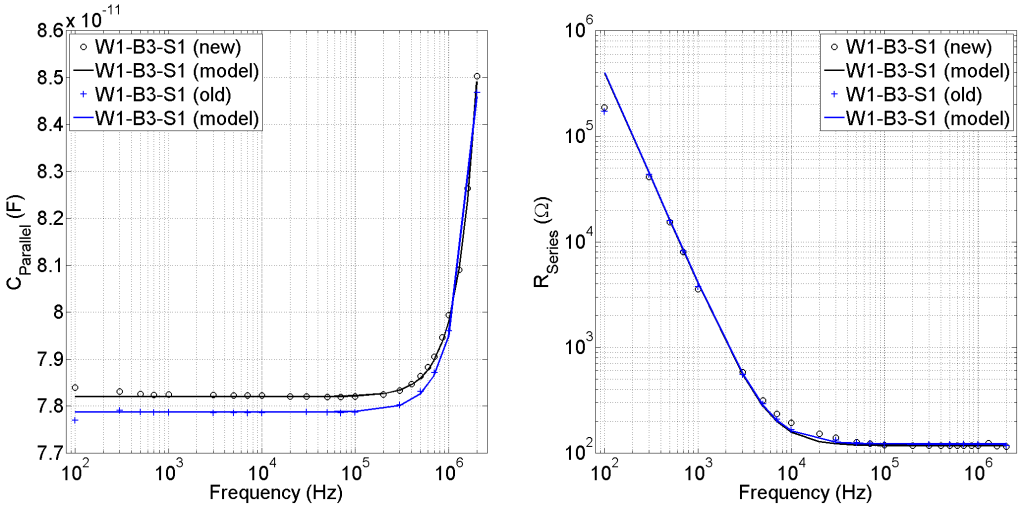

Fig. 4.21: Old (black) and new (blue) CV-f measurements. The parallel capacitances are shown on the left and series resistances on the right. In the case of C_p, a systematic difference is visible, whereas the measurements of R_s produce the same results.

are determined. The values calculated are 2 to 3 ns smaller than those, but the determination of τ_r from the oscilloscope is thought as a rough first estimate, so this deviation is comprehensible.

4.2.4 Investigation of the Series Inductance

In this section, the analysis results for the series inductance that is introduced to explain the rise of C_p at high frequencies are presented. Fig. 4.22 shows the ratios of L_{s0} before and $L_{s,i}$ after neutron irradiation. the absolute values of L_{s0} and $L_{s,i}$ are listed in Tab. 4.10. Since the origin and the dependences of L_s are not clearly understood, estimating the errors is not straight-forward. In order to calculate L_s, the value of C_p at 2 MHz is needed and as shown in section 4.2.2, C_p differs for the old and new measurements. The error for L_s is hence estimated, comparing the results calculated for the reference sample (W1-B3-S1) from the different measurements.

Looking at the absolute values in Tab. 4.10, one sees that the calculated values for L_s are all very similar to each other. After irradiation, decreases of the values between 1 and 4 % for all samples but one, that exhibits an increase of 2 %, are observed. However, the uncertainties of L_s are of the same magnitude.

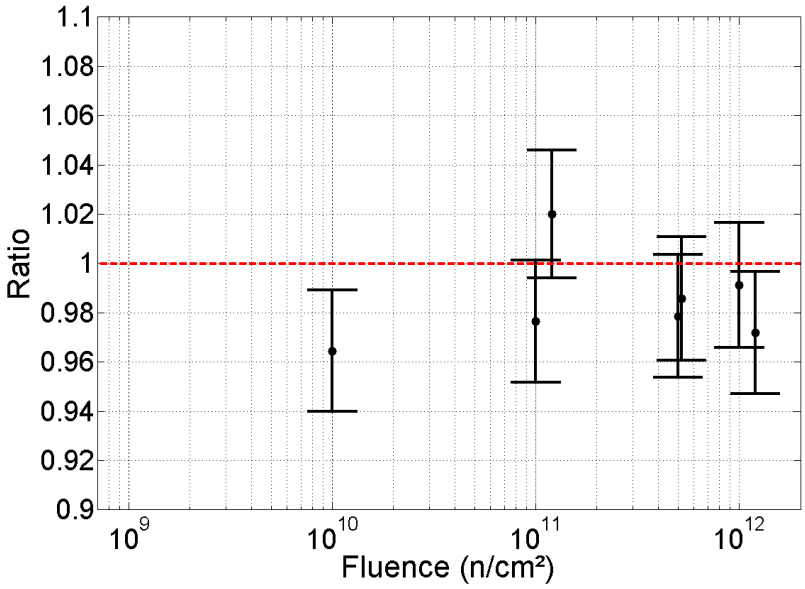

Fig. 4.22: The ratios of L_s after/before neutron irradiation extracted from the CV-f measurements. For clarity, the SiPMs irradiated at the same fluence are plotted offset.

Tab. 4.10: Series inductances of the SiPMs before L_{s0} and after $L_{s,i}$ neutron irradiation determined from the CV-f measurements at 25 °C. The applied voltage at which the data is extracted is 26.5 V. L_s is calculated from C_p at 2 MHz.

Sample	$\mathbf{\Phi(n/cm^2)}$	$\mathbf{L_{s0}}(\mu\mathbf{H})$	$\mathbf{L_{s,i}}(\mu\mathbf{H})$
W1-B2-S1	10^9	/	7.684 ± 0.138
W1-B2-S2	10^9	/	7.805 ± 0.140
W1-B2-S3	10^{10}	7.870 ± 0.142	7.591 ± 0.137
W1-B2-S4	10^{10}	/	7.626 ± 0.137
W1-B2-S5	10^{11}	7.790 ± 0.140	7.607 ± 0.137
W1-B2-S6	10^{11}	7.428 ± 0.134	7.576 ± 0.136
W1-B3-S2	$5 \cdot 10^{11}$	7.849 ± 0.141	7.681 ± 0.138
W1-B3-S3	$5 \cdot 10^{11}$	7.882 ± 0.142	7.769 ± 0.140
W1-B3-S4	10^{12}	7.857 ± 0.141	7.788 ± 0.140
W1-B3-S5	10^{12}	7.837 ± 0.141	7.617 ± 0.137
Mean	/	7.788 ± 0.140	7.674 ± 0.138
STD	/	0.161	0.086

4.3 Charge-Voltage Measurements

This chapter is divided into two parts. The first section presents the analysis results of the QDC measurements before neutron irradiation. Originally, it was planned to compare these results to the results of the measurements after neutron irradiation, like it was done with the IV and CV-f measurements. Why this is not possible is explained in section 4.3.2.

4.3.1 QDC measurements before Neutron Irradiation

In this section the gain of the SiPMs as well as the breakdown voltages determined from the gain are investigated. Also the DCR and the XT/AP probability are subject of the investigation. All the QDC measurements were done at 20 °C.

Investigation of the Gain and the Breakdown Voltage

Fig. 4.23 shows the gain of the devices as a function of voltage. For clarity, the results are divided over two graphs, each showing five of the ten samples. As described in section 3.4.3, the gain increases linearly with increasing voltage. Also the spread of the gain of all the devices is really small, the single devices vary by less than 1 % from each other. Tab. 4.11 shows the mean values of the gain extracted from the QDC histograms at three different voltages and for comparison, calculated values based on equation (3.29). For the calculation, the values of C_{pix}^{CV} from Tab. 4.8 were used and the breakdown voltage determined from the gain (see Tab. 4.12). To convert the gain into absolute values, equation (3.30) is used, with $G_{Amp} = 50$ and $IR(\frac{q}{ch}) = 25fC/ch$. The errors of the fit for the gain are in the range of per mil, but a systematic error of 2 % is assumed.

Tab. 4.11: Mean values of the gain G^{QDC} calculated from the QDC measurements of non-irradiated SiPMs compared to results calculated using the CV-f analysis G^{CV}. The breakdown voltages of the devices are approximately 26.6 V.

	@ 29.5 V	**@ 32 V**	**@ 35 V**
$\mathbf{G^{QDC}}$	$(252.82 \pm 5.06) \cdot 10^3$	$(478.58 \pm 9.57) \cdot 10^3$	$(740.20 \pm 14.80) \cdot 10^3$
STD	$5.40 \cdot 10^3$	$5.83 \cdot 10^3$	$6.73 \cdot 10^3$
$\mathbf{G^{CV}}$	$(327.25 \pm 16.37) \cdot 10^3$	$(609.37 \pm 30.47) \cdot 10^3$	$(947.91 \pm 47.40) \cdot 10^3$
STD	$1.48 \cdot 10^3$	$2.76 \cdot 10^3$	$4.30 \cdot 10^3$
Difference	$(74.43 \pm 21.43) \cdot 10^3$	$(130.79 \pm 40.04) \cdot 10^3$	$(207.71 \pm 62.20) \cdot 10^3$

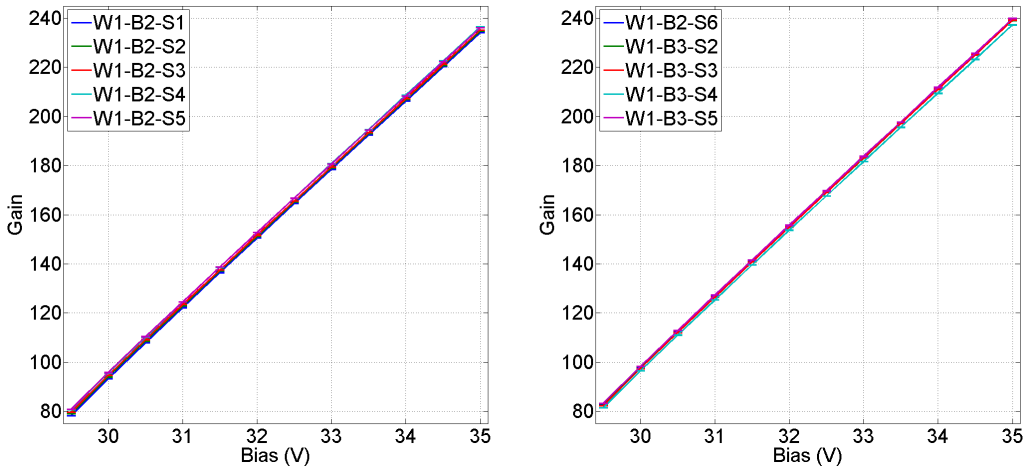

Fig. 4.23: The calculated values of the gain G^{QDC} of the non-irradiated SiPMs in units of channels and as a function of voltage.

Tab. 4.12: Breakdown voltages of the SiPMs before irradiation determined from the interpolation of the gain and the linear fit of the ILD. For comparison, their differences are also shown.

Sample	$\mathbf{V_{bd}^{G}\,(V)}$	$\mathbf{V_{bd}^{IV}\,(V)}$	$\mathbf{\Delta V_{bd}\,(V)}$
W1-B2-S1	26.67 ± 0.12	27.64 ± 0.03	0.97 ± 0.15
W1-B2-S2	26.64 ± 0.12	27.61 ± 0.03	0.97 ± 0.15
W1-B2-S3	26.61 ± 0.11	27.59 ± 0.02	0.98 ± 0.13
W1-B2-S4	26.59 ± 0.11	27.57 ± 0.02	0.98 ± 0.13
W1-B2-S5	26.57 ± 0.10	27.55 ± 0.02	0.98 ± 0.12
W1-B2-S6	26.55 ± 0.11	27.53 ± 0.03	0.98 ± 0.14
W1-B3-S2	26.53 ± 0.10	27.53 ± 0.02	1.00 ± 0.12
W1-B3-S3	26.54 ± 0.10	27.54 ± 0.02	1.00 ± 0.12
W1-B3-S4	26.55 ± 0.12	27.55 ± 0.02	1.00 ± 0.14
W1-B3-S5	26.53 ± 0.12	27.50 ± 0.03	0.97 ± 0.15
Mean	26.58 ± 0.11	27.56 ± 0.02	0.98 ± 0.13
STD	0.05	0.04	0.01

The values calculated with equation (3.29) are around 30 % larger than the values from the QDC measurement. This difference still has to be investigated. In Tab. 4.12, the values of V_{bd}^{G} determined by interpolating the gain curves to zero are shown. The errors given, are based on the statistics of the Gaussian fits to determine the peak position. Furthermore, the values extracted from the linear fit of the ILD and the differences of the two methods are added to the table.

A difference between the breakdown voltages of about 1 V is observed. The reason for this difference is not yet understood. Investigating the breakdown behavior of the SiPMs

Tab. 4.13: Mean values of the gain G^{QDC} calculated from the QDC measurements of non-irradiated SiPMs compared to calculated results using the CV-f analysis G^{CV}_{IV}. The breakdown voltages V^{G}_{bd} of the devices are approximately 26.6 V. For the calculation of G^{CV}_{IV} the breakdown voltage of the IV measurements has been used ($\approx 27.6\ V$).

	@ 29.5 V	**@ 32 V**	**@ 35 V**
$\mathbf{G^{QDC}}$	$(252.82 \pm 5.06) \cdot 10^3$	$(478.58 \pm 9.57) \cdot 10^3$	$(740.20 \pm 14.80) \cdot 10^3$
STD	$5.40 \cdot 10^3$	$5.83 \cdot 10^3$	$6.73 \cdot 10^3$
$\mathbf{G^{CV}_{IV}}$	$(214.41 \pm 10.72) \cdot 10^3$	$(496.52 \pm 24.83) \cdot 10^3$	$(835.06 \pm 41.76) \cdot 10^3$
STD	$0.97 \cdot 10^3$	$2.25 \cdot 10^3$	$3.78 \cdot 10^3$
Difference	$(-38.39 \pm 15.78) \cdot 10^3$	$(17.94 \pm 34.4) \cdot 10^3$	$(94.86 \pm 56.56) \cdot 10^3$

with the oscilloscope shows, that the first peaks due to pixel discharges appear for voltages slightly above 27.5 V. This gives a hint that V^{IV}_{bd} is the correct value. However, recent studies suggest that there is no 'correct' value, but only a difference in the turn-on and turn-off voltages of Geiger discharges [48]. During these studies, it was also shown that the difference depends on the pixel size of the SiPM. When operating a SiPM, V^{G}_{bd} is thought to be the relevant quantity for the user, because the gain is proportional to $V - V^{G}_{bd}$. Consequently, the excess voltage should be calculated using the value of V^{G}_{bd}. Nevertheless, using V^{IV}_{bd} for the calculation of G^{CV}, results in smaller values that are closer to the values of G^{QDC} (see Tab. 4.13). This raises the question which value for V_{bd} is the proper one in this case.

To further investigate this difference, the values from Tab. 4.13 and Tab. 4.11 are plotted in Fig. 4.24.

It can be seen that the curves for the different gain extraction methods exhibit a different slope. According to equation (3.27) this corresponds to a difference in the value of C_{pix}. This difference between the two extraction methods has already been observed in [27] and has been accredited to the absolute calibration of the gain measurement. The values for C^{QDC}_{pix} determined from the QDC measurements are around 20 % smaller than the values C^{CV}_{pix} extracted from the CV-f measurements. The respective mean values are: $< C^{QDC}_{pix} >= 14.15\ fF$ and $< C^{CV}_{pix} >= 18.08\ fF$.

The lower values of C^{QDC}_{pix} also lead to lower values of the recharge time τ_r. Using their values results in values of τ_r between 7 and 10 ns, which is too low compared to the pulse shapes of the SiPMs. As a result, the values of C^{CV}_{pix} are considered to be more precise. However, further studies are required, in order to understand the different values and their origin.

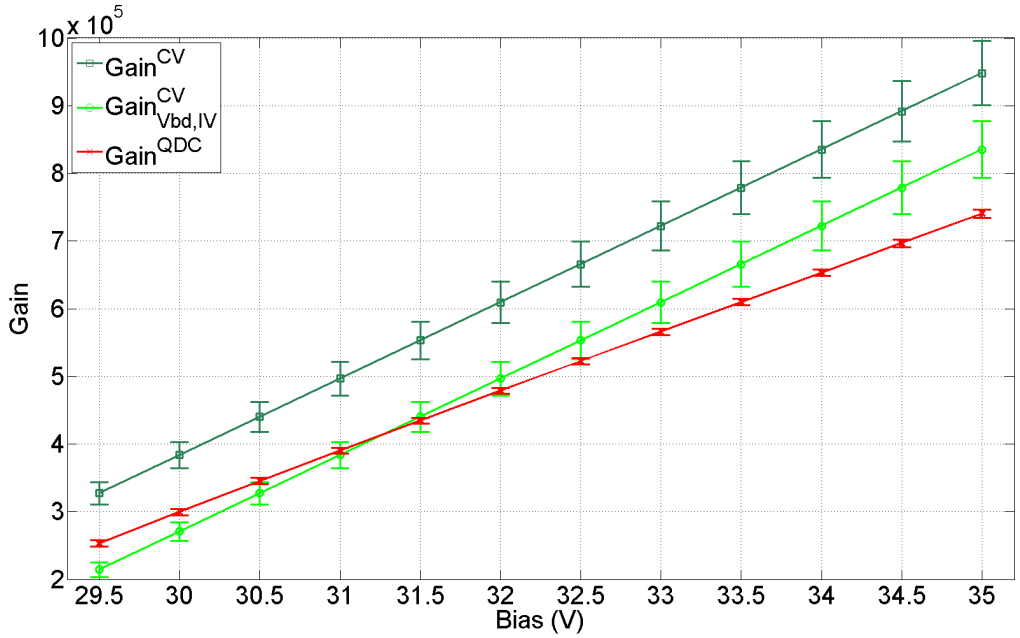

Fig. 4.24: The calculated values of the dark count rate (DCR) of the non-irradiated SiPMs as a function of voltage. The dark green curve shows G^CV assuming the breakdown voltage of the QDC measurements, whereas for the light green curves the breakdown voltage of the IV measurements is assumed. The red curve is based entirely on the QDC measurements. The difference in the curves slopes corresponds to a different pixel capacitance.

Investigation of the Dark Count Rate

In Fig. 4.25 the DCR values extracted from the QDC histograms of non-irradiated SiPMs are shown. The single devices reach similar values for the DCR, but a larger spread than in the gain is observable. The DCR of the device with the lowest value at 35 V (W1-B3-S5: 161.8 $\pm$ 1.9 kcps) is 40 % smaller than that of the device with the highest DCR (W1-B2-S5: 281.9 $\pm$ 2.6 kcps).
The results of the DCR analysis as well as the value of DCR^{IV} calculated using equation (4.6) are shown in Tab. 4.14. The errors of the QDC values are taken from the fit. For the errors of the IV measurements an error of 1 % for each measurement is estimated, based on the hysteresis analysis (see Fig. 4.2). The DCR behavior matches what has been observed in the IV curves in Fig. 4.1. Namely, that the SiPMs with the highest DCR (W1-B2-S5 and W1-B2-S6) also exhibit the highest dark currents below breakdown. Above the breakdown, the influence of cross-talk and afterpulses comes in and a direct comparison becomes less easy.

In general, the values extracted from the IV curves are three times larger than the QDC values. If the assumptions used for the determination of DCR^{IV} are correct, the factor 3 would originate from the Geiger discharge probability P_{Gd} that should be contained in

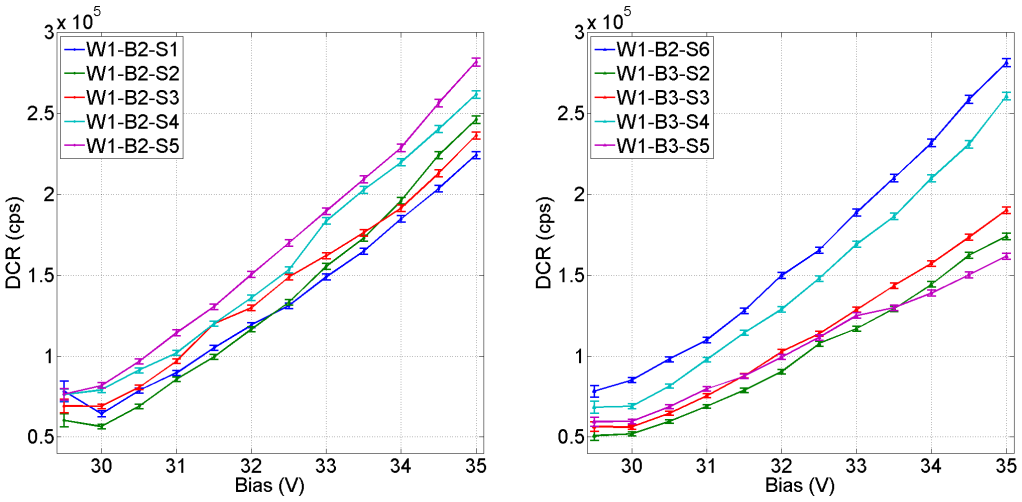

Fig. 4.25: The calculated values of the dark count rate DCR^{QDC} extracted from the QDC measurements of the non-irradiated SiPMs as a function of voltage.

Tab. 4.14: Mean values of the dark count rates DCR^{QDC} calculated from the QDC measurements of non-irradiated SiPMs compared to the results of the IV analysis DCR^{IV}. The breakdown voltages of the devices are approximately 26.6 V.

	@ 29.5 V (kcps)	**@ 32 V (kcps)**	**@ 35 V (kcps)**
DCR^{QDC}	67.37 ± 3.79	122.42 ± 1.65	190.37 ± 2.05
STD	10.04	20.58	33.93
DCR^{IV}	245.69 ± 4.91	376.26 ± 7.53	568.36 ± 11.37
STD	44.51	73.49	118.88
Ratio	3.65 ± 0.28	3.07 ± 0.10	2.99 ± 0.09
Ratio^{-1}	0.2739 ± 0.0210	0.3257 ± 0.01061	0.3344 ± 0.0101

the value of DCR^{IV} (see equation (4.6)). Assuming this is correct, dividing DCR^{QDC} by DCR^{IV} should result in the Geiger discharge probability. The values are shown in Tab. 4.14 as $Ratio^{-1}$.

According to Tab. 4.14 and Fig. 4.26, P_{Gd} would be in the range of 30 %. However, one would expect a much stronger increase for P_{Gd} with increasing excess voltage [41] and also values closer to 80 or 90 % [67]. The values of P_{Gd} can be extracted from simulations, which has not been done in the course of this thesis. As a result, the informative value of DCR^{IV} still has to be confirmed.

To check if the different breakdown voltage definitions might change something, the values of DCR^{IV} and DCR^{QDC} are plotted as a function of the excess voltage in Fig. 4.26. The excess voltages are based on the values of V_{bd}^{IV} in the case of DCR^{IV} and V_{bd}^{QDC} in the case of DCR^{QDC}. The applied reverse voltages range between 29.5 V and 40 V. As it can be seen, there is no significant change caused by the different breakdown voltages compared to what is reported in Tab. 4.14. The jump in the ratio at 2.9 V is due to problems

in setting the pixel thresholds in the histograms at low excess voltages (see Fig. 3.34).

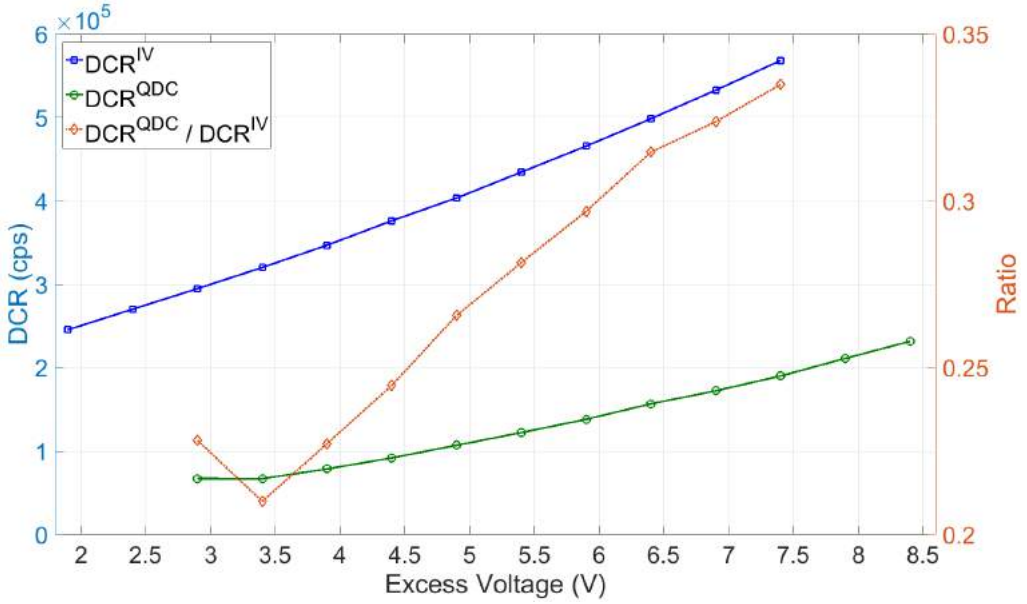

Fig. 4.26: The average dark count rate (DCR) of the non-irradiated SiPMs determined from the QDC measurements DCR^{QDC} and the IV measurements DCR^{IV} using equation (4.6). DCR^{IV} contains the Geiger discharge probability that should be represented in the ratios (orange curve) of the two different curves.

Since the analysis of the QDC measurements has been already used and approved in the thesis of C. Xu [27] and their values are also closer to the values of other KETEK devices [35], the QDC analysis is thought to be the more precise method to determine the DCR.

However, there is a different method currently under investigation that could predict the DCR of the SiPMs after irradiation. Assuming that the only dynamic parameter of the SiPM that changes due to neutron irradiation is the dark count rate and that other parameters like the gain, photon detection efficiency or correlated noise probability stay the nearly same, the following would apply:

$$I_{dark}(\Phi) = q_0 \cdot DCR(\Phi) \cdot G \cdot (1 + CNP) \tag{4.7}$$

Thus the DCR after neutron irradiation, $DCR(\Phi)$ could be calculated by:

$$DCR(\Phi) = \frac{I_{dark}(\Phi)}{I_{dark}(0)} \cdot DCR(0) \tag{4.8}$$

If and how good this method works is not yet studied in detail. The benefit of this method would be that the DCR after irradiation could be calculated from measurements that are not affected by the irradiation induced changes of the SiPMs. Namely, one would need IV measurements before and after irradiation and QDC measurements before irradiation. In section 4.3.2 it is explained why the increased dark current of the SiPMs after irradia-

tion causes major problems to the QDC measurements and the corresponding analysis. These problems could be avoided once the functionality of this method is proven.
A first test is presented in Fig. 4.27. The graph shows the calculated values of the DCR after irradiation for the sample W1-B2-S2 based on equation (4.8) compared to values extracted from QDC spectra. For the calculated values, the errors are composed of the errors from the value of $DCR(0)$ and the uncertainties of the current measurements.
The sample investigated is the only sample whose QDC measurements provided suitable dark current spectra after neutron irradiation. Unfortunately, only four out of twelve histograms, namely the histograms from 30.5 V to 32.0 V, show the single peak spectrum needed to apply the pixel thresholds for the DCR determination. Nevertheless, the first six histograms were investigated for the points shown in Fig. 4.27.
The errors of the QDC values are estimated to be around 10 %, but more investigation of the fits used is needed to give a good estimation. As a consequence, the QDC values are plotted without error bars.

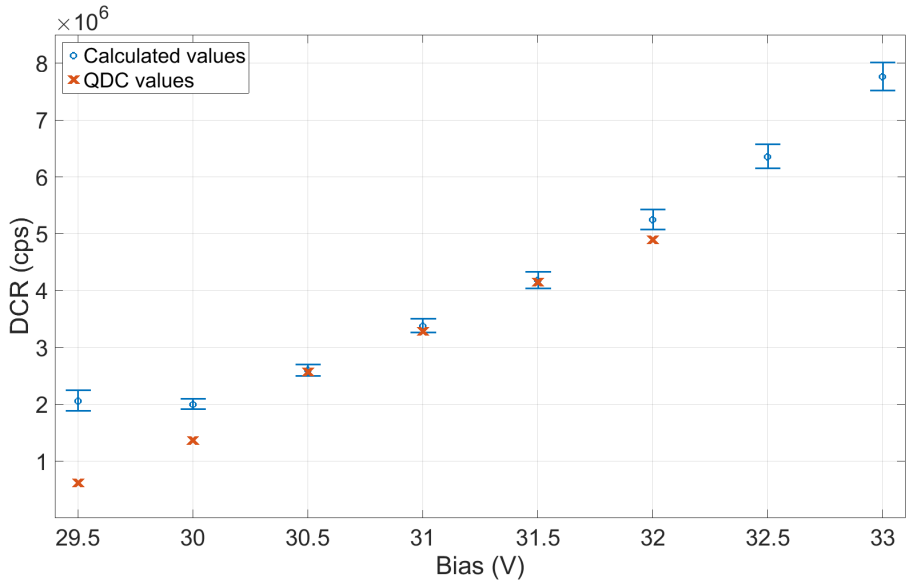

Fig. 4.27: Values of the DCR of sample W1-B2-S2 after neutron irradiation at 10^9 n/cm^2 calculated using equation (4.8) compared to the data extracted from QDC histograms. Due to the lack of suitable dark current spectra only six points are available for the comparison.

Due to the lack of sufficient data for comparison, this first test is not heavily significant, but already gives a good outlook. From 30.5 V to 32 V, the values extracted from the QDC histograms are close to the calculated values. The QDC histograms and the applied fits are plotted in Fig. 4.28 and Fig. 4.29.

Why the values extracted from the histograms at 29.5 V and 30 V are not the same as the ones calculated from equation (4.8) becomes clear looking at the histograms in Fig. 4.28: For the two lowest voltages the second peak is barely developed and determining the

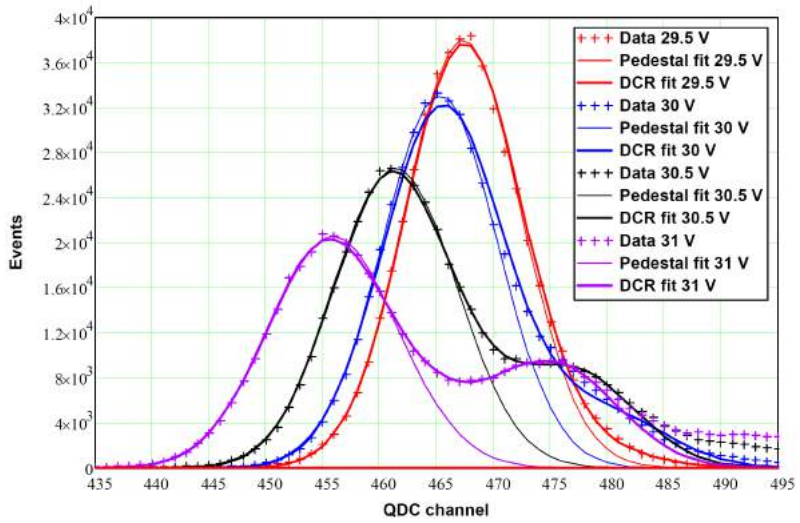

Fig. 4.28: QDC histograms of the SiPM W1-B2-S2 after neutron-irradiation at 10^9 n/cm^2. Shown are the four lowest voltages. The histograms of the two lowest voltages lack a well developed second peak.

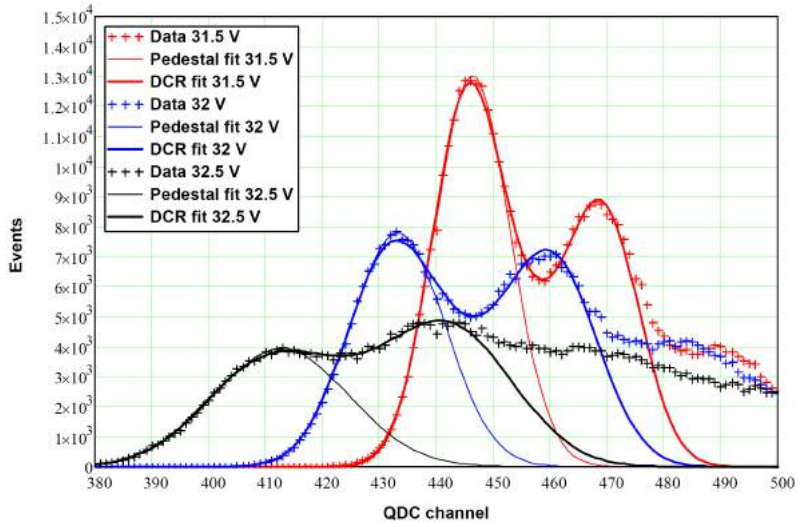

Fig. 4.29: QDC histograms of the SiPM W1-B2-S2 after neutron-irradiation at 10^9 n/cm^2. The histograms of the highest voltage exhibits a deterioration of the distinctness of the single peaks.

0.5 pixel threshold is not easily done. In a similar way Fig. 4.29 can be used to explain why the extraction fails for voltages above 32 V: The peaks are smeared out and a clear distinction between the two first peaks becomes less easy than for the lower voltages and the fits fail to deliver reasonable results.

Nevertheless, these first results look promising and whether this method, to determine the DCR, is applicable for higher fluences will be part of future studies.

Investigation of the Cross-talk and Afterpulse Probability

The values of the cross-talk and afterpulse or correlated noise probability (CNP) extracted from the QDC histograms of the non-irradiated SiPMs are plotted in Fig. 4.30. In Tab. 4.15 the mean values of the CNP for three different excess voltages are shown.

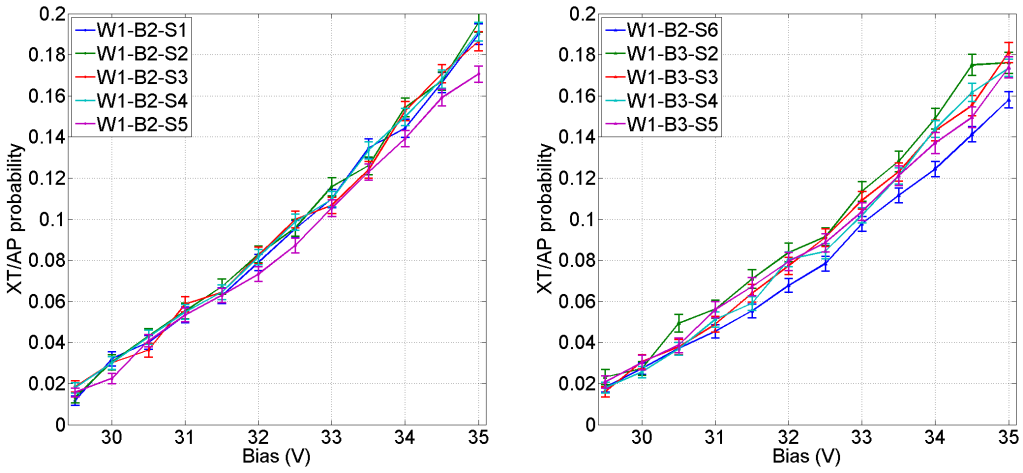

Fig. 4.30: The calculated values of the cross-talk (XT) and afterpulse (AP) probability of the non-irradiated SiPMs extracted from the QDC measurements as a function of voltage.

Tab. 4.15: Mean values of the correlated noise probability CNP calculated from the QDC measurements of non-irradiated SiPMs. The breakdown voltages of the devices are approximately 26.6 V.

	@ 29.5 V	**@ 32 V**	**@ 35 V**
CNP	0.0180 ± 0.0026	0.0788 ± 0.0040	0.1786 ± 0.0046
STD	0.0027	0.0049	0.0108

What is remarkable is that the samples with the lowest correlated noise probability are the same that show the highest DCR (W1-B2-S5 and W1-B2-S6). This partly confirms the assumption that the dark current before neutron irradiation does not experience the same multiplication as the LED current does. Otherwise, one would expect that the SiPMs with the highest DCR are also amongst the SiPMs with a higher CNP. The highest reached value at the highest excess voltage is 0.196 ± 0.005 (W1-B2-S2) and the lowest is 0.158 ± 0.004 (W1-B2-S6), which corresponds to a difference of 19.4 %. The SiPMs with the highest values of the dark current above breakdown (W1-B2-S2, W1-B2-S1) are also amongst the ones exhibiting the highest CNP. Which confirms that above breakdown, the CNP becomes more important and can play a bigger role than the DCR.

4.3.2 QDC measurements after Neutron Irradiation

The analysis of the QDC measurements is dependent on the quality of the histograms taken and the separation of the single peaks that correspond to the number of pixels discharging. When these peaks are not clearly separated, fitting them with Gaussian functions ceases to work. This is what happens for the measurements at room temperature after having the SiPMs irradiated with neutrons. Due to the increased dark current at room temperature, the single peaks disappear in the background signal.
In order to avoid measuring too many of the dark counts, a shorter integration gate of 10 ns was tested. In Fig. 4.31, the resulting histogram at an excess voltage of 2.9 V is depicted. The SiPM investigated (W1-B2-S1) was irradiated at 10^9 n/cm^2 and illuminated with an LED at low light intensity. For the lowest irradiation step, the single peaks are still separable. The signals corresponding to the single peaks are also visible on the oscilloscope (see Fig. 4.32). However, a cut-off appears at low channels in the QDC spectrum.

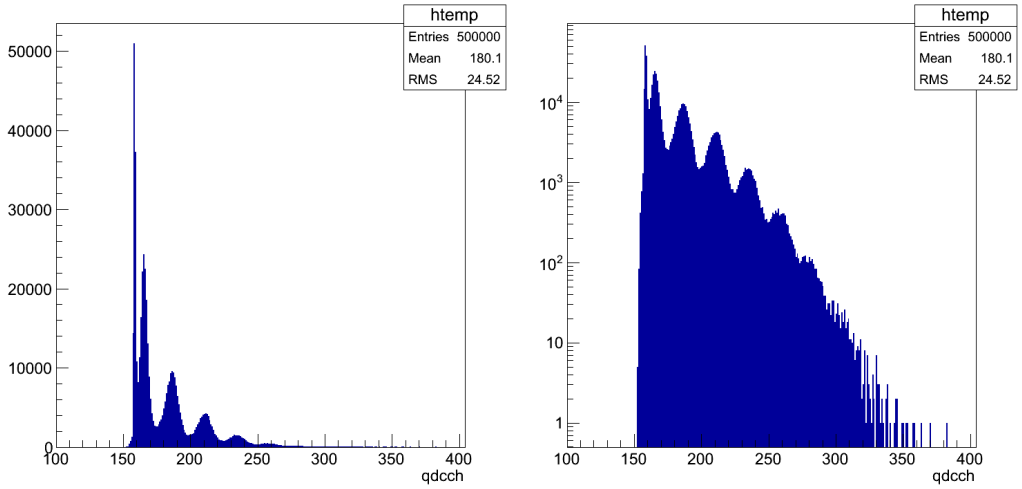

Fig. 4.31: Histograms of a charge-voltage measurement of a SiPM (W1-B2-S1) irradiated at 10^9 n/cm^2 in linear (left) and logarithmic scale (right). The integration gate length is 10 ns and the applied voltage is 29 V, which corresponds to an excess voltage of 2.4 V at room temperature. The single peaks are visible but a cutoff for lower channels appears. For illumination the low LED intensity setting is used.

Investigating the SiPM signal with the oscilloscope, reveals the cause of the cut-off (see Fig. 4.32): Before irradiation, the baseline (i.e. signals of no pixels discharging) was symmetrically placed with respect to the zero level (the teal line). However, after irradiation the signals are shifted and a greater fraction of the signals lies above the zero level. This causes the integration procedure of the QDC to malfunction and the values of these signals result in the non-physical peak at channel 160. What happens in detail and why the entries peak at that certain channel was not further studied.

To resolve this problem, a constant DC signal was added with a 8-channel fast amplifier (CAEN N412). Since this device has an built-in amplification factor of 10, the Phillips amplifier used before was replaced with an amplifier of the same model, but with an amplification factor of 5. This was necessary, in order to maintain the total amplification factor of 50.

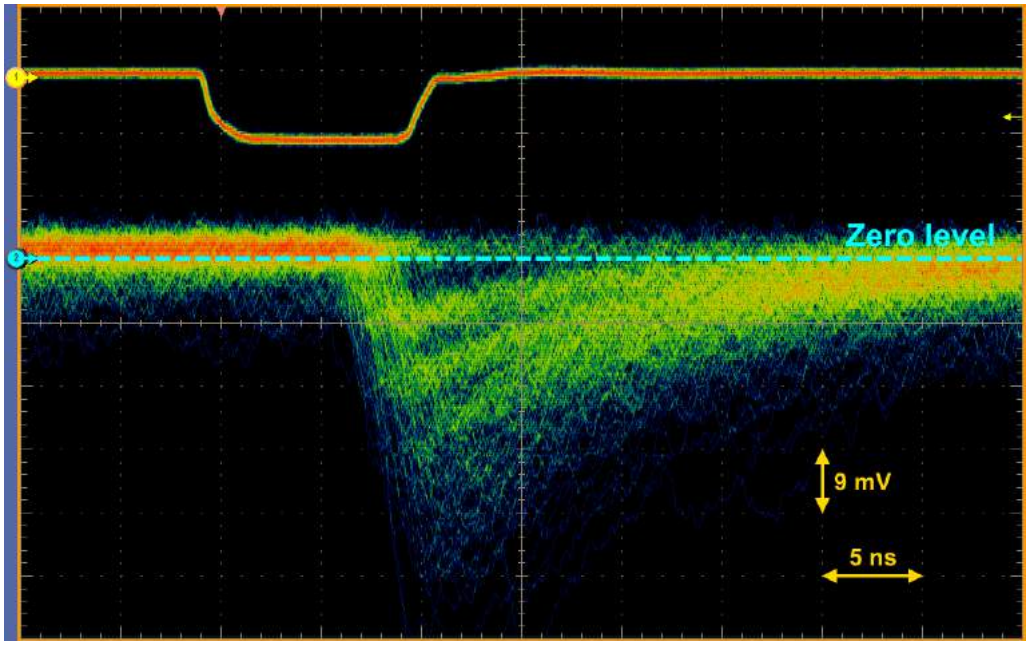

Fig. 4.32: Oscillogram of the signal of a SiPM after neutron irradiation at 10^9 n/cm^2. The detector is operated at 30 V, which corresponds to an excess voltage of 3.4 V at room temperature. The main fraction of the measured values for no pixel discharging lies above the zero level. For illumination the low LED intensity setting is used.

Figures 4.33 and 4.34 show the histograms of a SiPM (W1-B2-S4) irradiated at 10^{10} n/cm^2, illuminated with low LED intensity. Fig. 4.33 is the result of a measurement with a short integration gate of 10 ns. Unlike in Fig. 4.31 the single peak resolution is lost. Additionally, even more entries are collected at 160. Subsequently, the same measurement has been repeated with a longer integration gate of 100 ns. The results are shown in Fig. 4.34. In these histograms the peak structure can be spotted, but the single peaks are heavily smeared and a Gaussian fit fails to determine the mean value of the peak position. The measurement was done without the DC shift, but due to the larger gate, the cut-off disappeared.

As a result, the analysis described in chapter 3 could not be applied to the irradiated samples. Fig. 4.35 shows the oscilloscope image of a SiPM irradiated at 10^{11} n/cm^2. It is illuminated by the LED with the same LED voltage that was used for the low light setting before irradiation. The SiPM is operated at 30 V at room temperature.

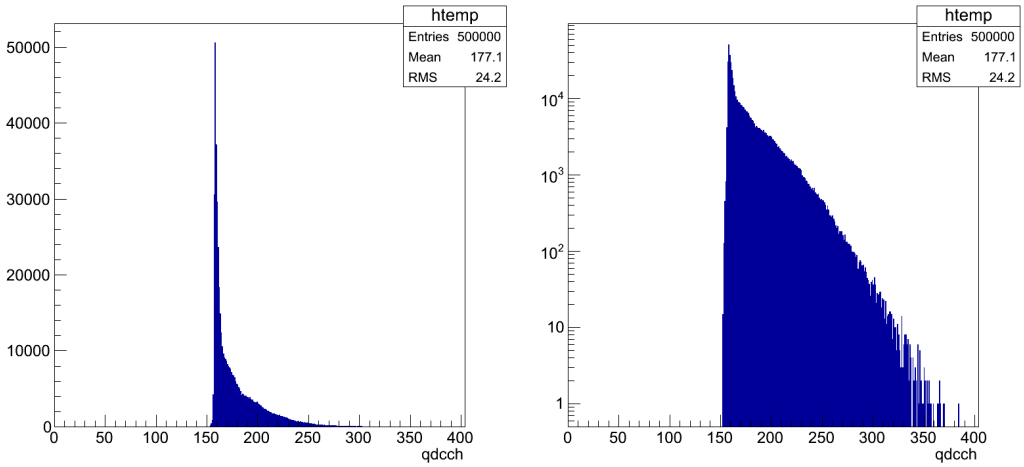

Fig. 4.33: Histograms of a charge-voltage measurement of an illuminated SiPM irradiated at 10^{10} n/cm^2 in linear (left) and logarithmic scale (right). The integration gate length is 10 ns and the applied voltage is 29 V, which corresponds to an excess voltage of 2.4 V at room temperature. The single peak resolution is lost and the a cut-off at lower channels is even more drastic.

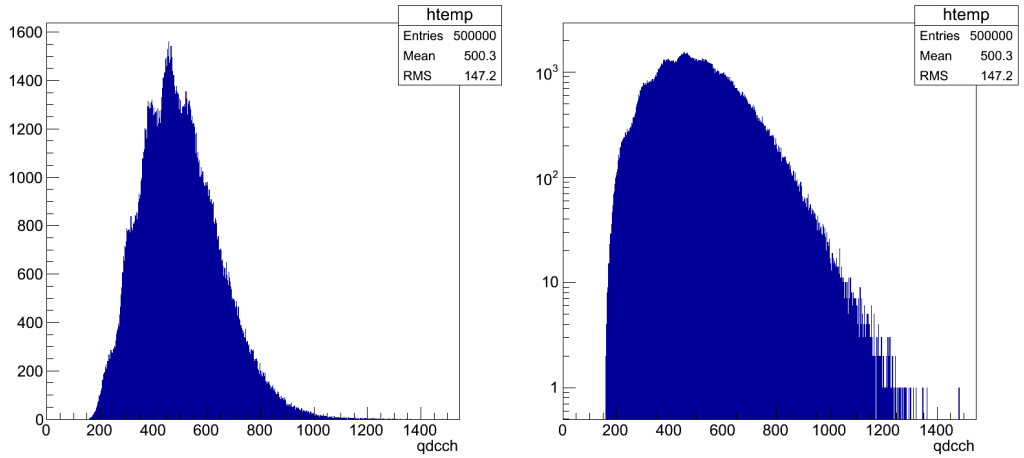

Fig. 4.34: Histograms of a charge-voltage measurement of an illuminated SiPM irradiated at 10^{10} n/cm^2 in linear (left) and logarithmic scale (right). The integration gate length is 100 ns and the applied voltage is 29.5 V, which corresponds to an excess voltage of 2.9 V at room temperature. The position of the single peaks can be estimated but they are not well-defined. The cut-off at lower channels disappeared because of the longer gate.

Several important features are depicted in the picture: Firstly, the zero level that is shifted using the CAEN N412. Between the zero level and the mean value of the baseline is a difference of about 50 mV. This does not recover the single peaks in the histograms, but results in a more reasonable histogram without a cut-off.
Secondly, compared to Fig. 4.31, the width of the baseline has increased from 10 mV to 40 mV. This corresponds to and confirms the fluence dependent increase of the dark current. Thirdly, due to the increased dark current, the peak of the firing pixels is not

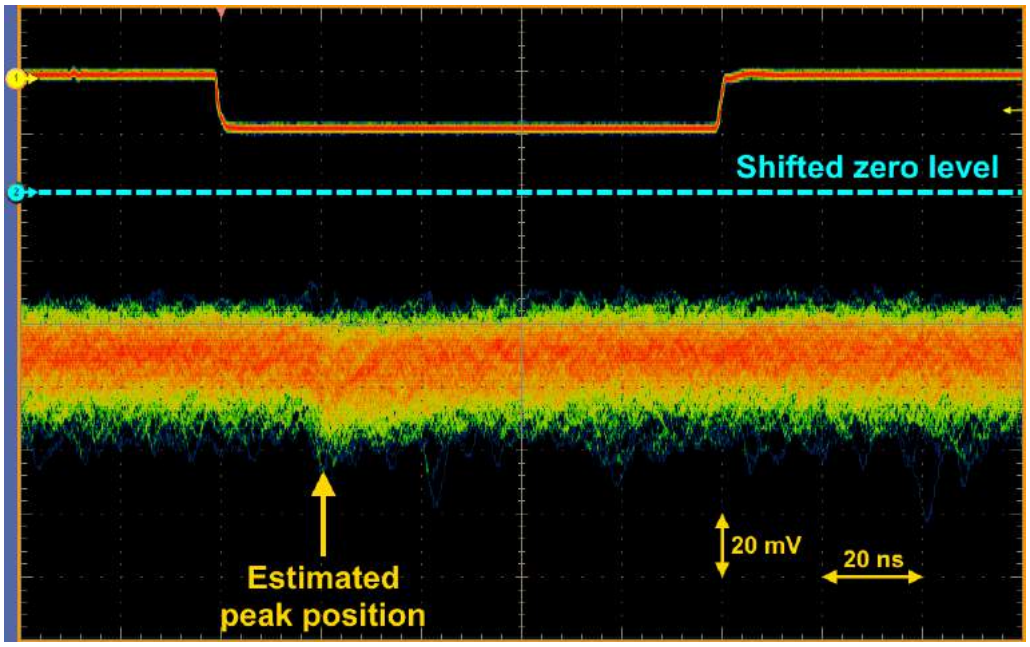

Fig. 4.35: Oscillogram of the signal of a SiPM after neutron irradiation at 10^{11} n/cm^2. The detector is operated at 30 V, which corresponds to an excess voltage of 3.4 V at room temperature. To obtain reasonable histograms, the zero line has been shifted, applying a DC voltage. For illumination the low LED intensity setting is used. The position of the peak, corresponding to the pixels firing, is barely visible.

clearly distinguishable anymore. There is a bump visible at the estimated peak position, but it is very small.
Fig. 4.36 shows an oscillogram of the same device, operating at the same voltage and temperature but illuminated with the higher LED intensity with 8 V LED voltage. In this case, the peak of the pixels firing is clearly visible, but unlike to Fig. 4.32, it is impossible to divide it into single contributions of a different number of pixels firing.

Future Plans and Predictions for QDC measurements

A possible way to regain the single pixel resolution, is to take the measurements at lower temperatures in order to reduce the dark current. This has proven to work at -40 °C in [15]. However, the setup used in the course of this thesis is not able to reach temperatures this low. Additionally, there is no dry air supply included which is needed to avoid condensation of water on the detectors while performing low temperature measurements.
As a consequence, the QDC measurements after neutron irradiation were not pursued further. For each sample, measurements with high LED intensity were taken, but due to the lack of proper analysis methods not yet investigated. For the future, it is planned to redesign the setup, using a different climate chamber that can cool down to -40 °C and

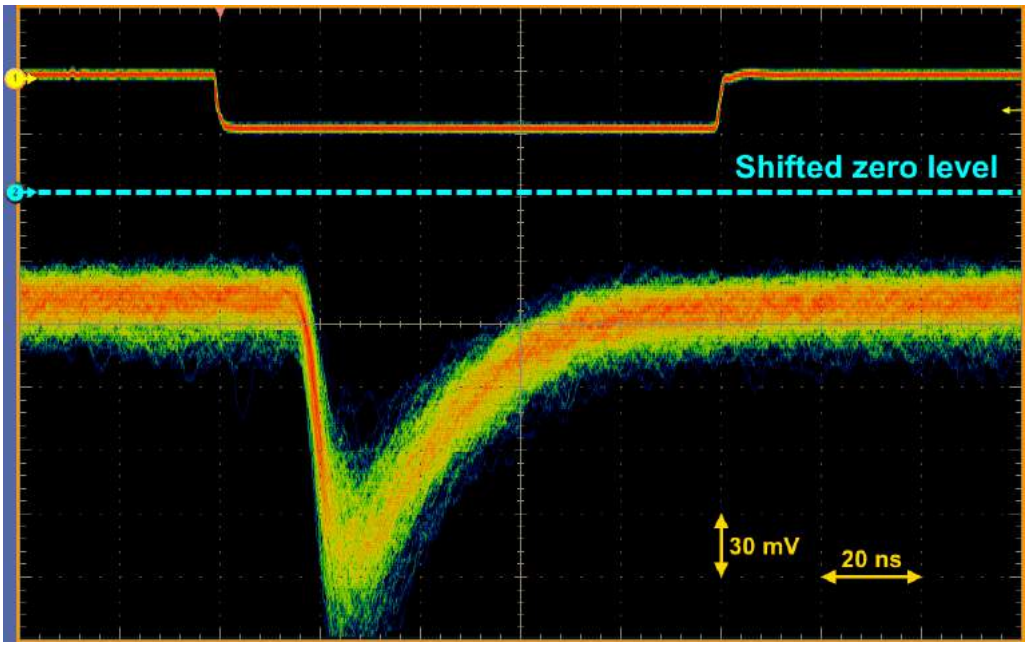

Fig. 4.36: Oscillogram of the signal of a SiPM after neutron irradiation at 10^{11} n/cm^2. The detector is operated at 30 V, which corresponds to an excess voltage of 3.4 V at room temperature. The zero line has been shifted, applying a DC voltage. For illumination the high LED intensity setting is used. The peak position of the firing pixels is clearly visible, but single lines are not perceivable.

has a dry air supply. Once this is finished, the measurements with the low light setting will be repeated, in the hope that the established analysis methods will then work again. Nonetheless, judging from the analysis already done, some expectations of the future DC results can be given: Looking at the analysis of the IV curves, neither the breakdown voltage nor the behavior of the LED current of the SiPMs has changed due to neutron irradiation (compare Tab. 4.5 and Fig. 4.6). Consequently, no change or only minor changes in the gain and the breakdown voltages extracted from the QDC measurements are expected. However, it has to be kept in mind that the planned measurements will be done at -40 °C, thus the results have to be corrected for the temperature.
On the other hand, major changes in the dark current have been observed after neutron irradiation. As a result, the DCR of the devices is expected to have increased seriously as a function of fluence. Comparing the normalized LED currents before and after irradiation, small changes below 10 % have been observed. This might hint to an increase of the CNP because of trap-assisted effects like afterpulses and delayed cross-talk.

5 Conclusion and Outlook

In the course of this thesis, ten SiPMs produced by KETEK have been investigated before and after irradiation with neutrons. There is an additional set of ten SiPMs with a slightly different design, that have been measured before neutron irradiation but due to time constraints not yet investigated further. For irradiation, five fluences between 10^9 and 10^{12} n/cm^2 have been chosen. These values are comparable to the fluences SiPMs will have to endure when used in high energy physic experiments like the LHC or CALICE.
To extract information about the devices properties and performance, IV, CV-f and QDC measurements have been taken.
The IV curves were used to investigate the breakdown behavior of the SiPMs as well as their quenching resistances. Taking IV curves with and without LED illumination allowed to study the behavior of the dark current of the devices and compare it to the photo current of the SiPMs. Studying the inverse logarithmic derivative of the IV curves in the breakdown region, it was shown that the breakdown voltage does not change after irradiation. Several methods to extract the breakdown voltage were used and compared for systematic investigation, but the result is unchanged for all methods.
The quenching resistances of the devices show an increase of 5 to 8 % for the two highest fluences. Additionally, with increasing fluence a rise of the dark current by several orders of magnitude has been observed. This drastic increase, especially at the highest fluence, is one of the main concerns when operating SiPMs in radiation environments and poses a limit to their use. However, it was also observed that the normalized LED current changed by less than 10 % after neutron irradiation, even at the highest fluence. This means that the SiPMs light detecting abilities have barely deteriorated. This could also be confirmed, investigating the n-factor that can be extracted from a fit of the ILD. The factor contains information about SiPM properties like the gain or the cross-talk and has not changed after neutron irradiation. To conclude, in order to make SiPMs more suitable for operation in radiation environments, the main goal should be to minimize their dark current.
From the CV-f measurements several static parameters of the SiPMs have been extracted. Namely the pixel capacitance, the quenching resistance and the parasitic resistance. Additionally, a series inductance had to be introduced in order to explain the behavior of the SiPMs parallel capacitance at high frequencies. Its source is not yet understood. All of these parameters have been compared before and after neutron irradiation.
The values of the pixel capacitances have decreased by around 1.5 % after irradiation, independent of the fluence. From this 1.5 %, a part can be contributed to a systematic difference between the CV-f measurements that have been done at different points in time. The remaining change is of the same order of magnitude as the uncertainties of the C_{pix}

determination.
In the case of the quenching resistances an increase has been observed for the highest fluences, similar to what has been observed in the IV analysis. However, the maximum change was only 3 %. Since the determination of R_q^{IV} from the IV curves is based on the flawed assumption that the forward IV curve behaves linearly in a certain range, the values determined from the CV-f measurements are thought to be the more precise ones. The parasitic resistances exhibit a fluence dependent decrease. At 10^{10} n/cm^2 R_{par} has decreased by $\approx$ 50 % and at the highest fluence, the parasitic resistance is only a tenth of its original value. This decrease corresponds to the observed rise of the SiPMs dark current.
Lastly, the analysis of the series inductances found that their values have not changed within their determination uncertainties.
The third type of measurement, namely the QDC measurements, were used to determine performance parameters of the SiPMs like the gain, the dark count rate or the correlated noise probability. Analyzing the gain as a function of voltage, offers a second way to extract the breakdown voltage. The gain, DCR and CNP all showed the expected increase with increasing excess voltage and were compatible with the parameters of other KETEK devices. The breakdown voltages, calculated from the QDC measurements, though are lower by around 1 V compared to the values of the IV analysis. This feature is still under investigation. Tests with different KETEK devices showed that this difference is dependent on the pixel size of the SiPM. As reported in [48], a possible explanation for the feature is the existence of a difference between the turn-on and turn-off voltage of the Geiger discharges.
However, from comparing the values of the pixel capacitances extracted from the QDC and the CV-f measurements, a systematic difference has been observed. This influences the slope of the gain and thus the extracted value of the breakdown voltage. The pulse shape of the SiPMs signal indicates that the values of C_{pix}^{CV} extracted from the CV-f measurements are more precise, because they result in a value of the recharge time τ_r that agree with the pulse shape of the SiPMs. To finally evaluate this difference, more systematic studies are needed.
In contrast to the other two types of measurements, the QDC measurements could not be done properly after neutron irradiation. The analysis methods of the QDC measurements are based on single peak spectra and due to the increased dark currents, the SiPMs lost their single photon resolution at room temperature. This made it impossible to apply the analysis methods used before the neutron irradiation.

Outlook

To study the defects caused by the neutron irradiation as well as their influences, further IV measurements are planned.
Since the defects have a temperature dependent behavior, IV measurements with and without LED illumination at several different temperatures will be taken. Based on these measurements, Arrhenius plots can be generated. Arrhenius plots are often used to study radiation effects. They allow to extract the activation energies of defects and to distinguish the contributions of the diffusion and generation current to the DCR. To interpret the measurements TCAD simulations are needed which are currently in development. The results are intended to be presented at the IEEE conference 2016 in Strasbourg and will also be part of the bachelor thesis of Svenja Sonder.
Another possibility to further investigate the defects caused by irradiation are annealing studies. This means that the SiPMs will be stored at higher temperatures (60-80 °C) for a certain amount of time (several days). In a high physics experiment, SiPMs are exposed to radiation and will nonetheless operate for several months or even years. During this period of time, some of the irradiation induced defects will alter and be annealed. To simulate these conditions after a longer operation time is the idea of annealing studies.
In order to characterize the performance parameters of the SiPMs, more QDC measurements at low temperatures have to be done. The temperature aimed for is -40 °C. As already mentioned, the setup used was not suited for measurements under such conditions. However, a new setup is being prepared which will operate at -40 °C. Once the new setup is established, it is also possible to further investigate why the QDC measurements result in different values for the breakdown voltage, gain and pixel capacitance of the SiPMs compared to the IV or CV-f measurements.
More CV-f measurements at different temperatures or conditions are not prioritized, because it was shown that the parameters extracted from these measurements do not alter much. If the series inductance, the electric field or effective doping concentrations of the SiPMs should be further investigated, more CV-f measurements might be considered.
The future studies will first focus on the wafer 1 SiPMs, due to the fact that they already provide a lot of potential data for analysis. In addition to this, IV and CV-f measurements are very time-consuming. A single IV measurement takes up to two hours and a CV-f measurement around one hour, which excludes the waiting time for parameters like temperature or humidity to reach the desired values. A QDC measurement only takes around 20 minutes, but once the new setup is prepared, it will need to be calibrated and optimized, which will also cost some time.

In the end, our hope is to be able to gain sufficient insight on the mechanism of generation of the dark current before and in particular after irradiation to be able to control and possibly reduce it.

A Appendix

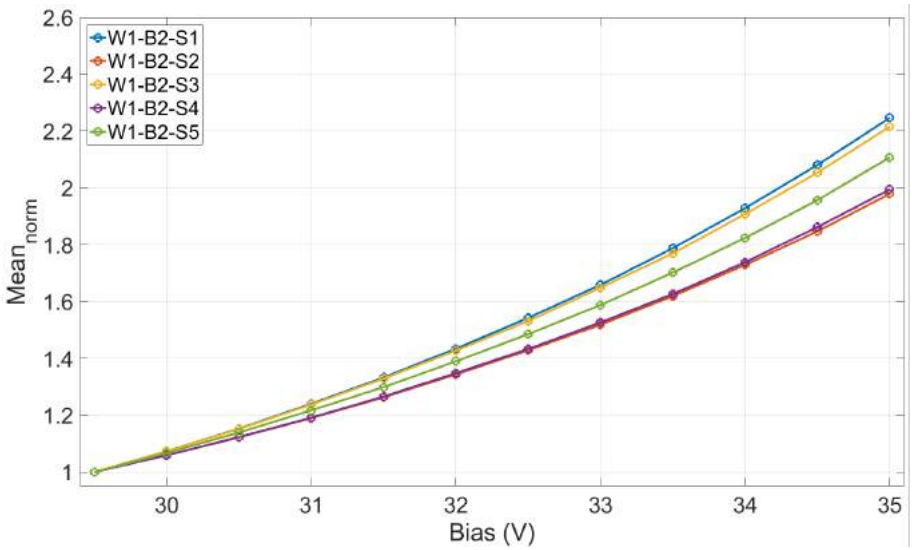

Fig. A.1: Mean values of the low light QDC histograms of the wafer 1 SiPMs before irradiation. The values are normalized to the first measurement point.

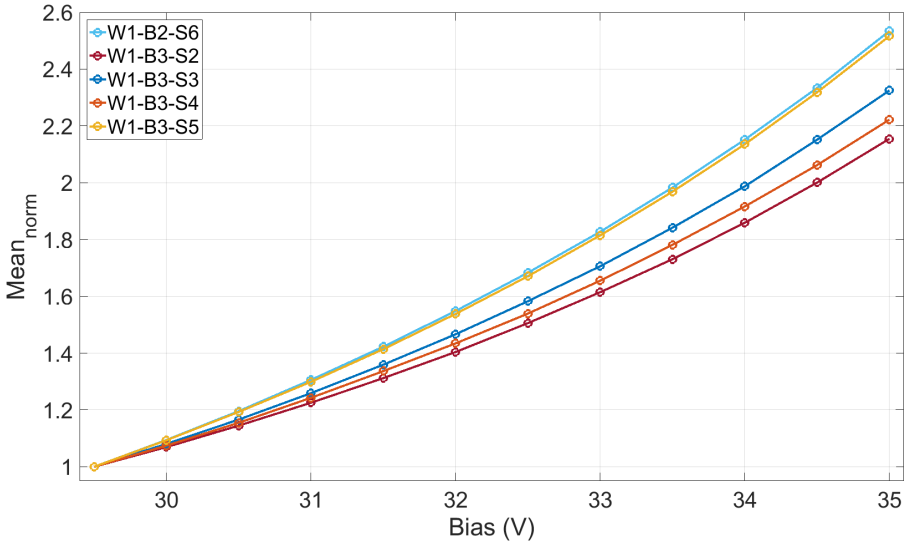

Fig. A.2: Mean values of the low light QDC histograms of the wafer 1 SiPMs before irradiation. The values are normalized to the first measurement point.

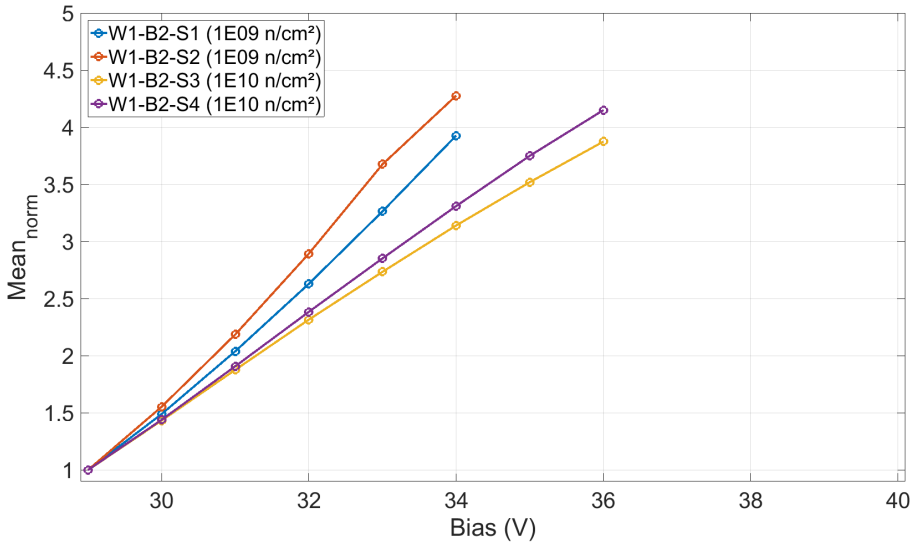

Fig. A.3: Mean values of the high light QDC histograms of the wafer 1 SiPMs after irradiation. The values are normalized to the first measurement point. The samples irradiated at the two lowest fluences are shown. Compared to figure A.4 several data points are missing. This is due to the measurement exceeding the QDCs dynamic range.

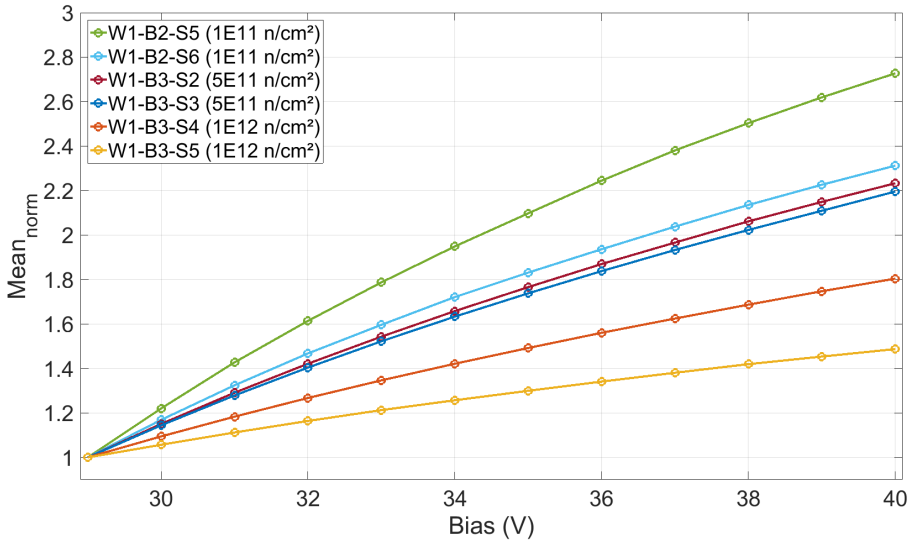

Fig. A.4: Mean values of the high light QDC histograms of the wafer 1 SiPMs after irradiation. The values are normalized to the first measurement point. The samples irradiated at the three highest fluences are shown.

Bibliography

[1] Frank Träger. *Springer Handbook of Lasers and Optics, 2nd Edition*. Springer-Verlag Berlin Heidelberg, 2012.

[2] Paul A. Tipler. *Physik*. Spektrum Akademischer Verlag, 2000.

[3] Wolfgang Demtroeder. *Experimentalphysik 3, 3. Auflage*. Springer-Verlag Berlin Heidelberg, 2005.

[4] Glenn F. Knoll. *Radiation Detection and Measurement, Third Edition*. John Wiley & Sons, Inc., 2000.

[5] Hamatsu Photonics K.K. microPMT Hamamatsu, micro PMT Assembly, micro PMT modules, 2014. http://www.hamamatsu.com/resources/pdf/etd/MicroPMTTPMZ1019E.pdf.

[6] N. Otte. The Silicon Photomultiplier - A new device for High Energy Physics, Astroparticle Physics, Industrial and Medical Applications. Stanford, California, USA, April 2006. SNIC Symposium.

[7] D. Renker and E. Lorenz. Advances in solid state photon detectors. *Journal Of Instrumentation*, 4:P04004, 2009.

[8] E. Garutti. SiPMs for HEP detectors. Justus-Liebig-University, Giessen, Germany, April 2011. DIRC.

[9] Y. Musienko, D. Renker, Z. Charifoulline, K. Deiters, S. Reucroft, and J. Swain. Study of radiation damage induced by 82 MeV protons on multi-pixel Geiger-mode avalanche photodiodes. *Nuclear Instruments and Methods in Physics Research Section A*, 610(1):87–92, 2009.

[10] Y. Qiang, C. Zorn, F. Barbosa, and E. Smith. Radiation Hardness Tests of SiPMs for the JLab Hall D Barrel Calorimeter. *Nuclear Instruments and Methods in Physics Research Section A*, 698:P 234–241, 2013.

[11] C. Xu, R. Klanner, E. Garutti, and W.L. Hellweg. Influence of X-ray irradiation on the properties of the Hamamatsu silicon photomultiplier S10362-11-050C. *Nuclear Instruments and Methods in Physics Research Section A*, 762:149–161, 2014.

[12] G. Lindstroem, M. Moll, and E. Fretwurst. Radiation hardness of silicon detectors - a challenge from high-energy physics. *Nuclear Instruments and Methods in Physics Research Section A*, 426:1–15, 1999.

[13] G. Casse an P. Allport and M. Hanlon. Improving the radiation hardness properties of silicon detectors using oxygenated n-type and p-type silicon. *IEEE Transactions on Nuclear Science*, 47(3):527–532, 2000.

[14] T. Nakamori et al. Development of Radiation-hardened Multi Pixel Photon Counters. Rio de Janeiro, Brazil, July 2013. ICRC.

[15] D. Gerick. Dark noise rates in irradiated silicon photomultiplier arrays. Hamburg, Germany, March 2016. DPG Früjahrstagung 2016.

[16] Wolfgang Demtroeder. *Experimentalphysik 4, 2. Auflage*. Springer-Verlag Berlin Heidelberg, 2005.

[17] Robert D. Purrington. *Physics In The Nineteenth Century*. Rutgers University Press, 1997.

[18] Claude Leroy and Pier-Giorgio Rancoita. *Silicon Solid State Devices and Radiation Detection*. World Scientific Publishing Co. Pte. Ltd., 2012.

[19] David R. Lide. *CRC Handbook of Chemistry and Physics*. CRC Press, 2005.

[20] Jasprit Singh and Umesh K. Mishra. *Semiconductor Device Physics and Design, 3rd Edition*. Springer, 2008.

[21] Simon M. Sze. *Physics of Semiconductor Devices, 3rd Edition*. John Wiley & Sons, Inc., 2007.

[22] J.P. Colinge and C.A. Colinge. *Physics of Semiconductor Devices*. Springer US, 2002.

[23] Paul A. Tipler. *Physics for Scientists and Engineers, Fifth Edition*. W. H. Freeman and Company, 2004.

[24] Sami Franssila. *Introduction to Microfabricatoin, Second Edition*. John Wiley & Sons, Inc., 2010.

[25] J.S. Chitode. *Power Electronics - III*. Technical Publications Pune, 2009.

[26] Andrew S. Grove. *Physics and Technology of Semiconductor Devices, Wiley International edition*. John Wiley & Sons, Inc., 1967.

[27] Chen Xu. *Study of the Silicon Photomultipliers and Their Applications in Positron Emission Tomography*. PhD thesis, Universität Hamburg, 2014.

[28] Gerhard Lutz. *Semiconductor Radiation Detectors*. Springer-Verlag Berlin Heidelberg, 2007.

[29] Sandro Carrara. *Nano-Bio-Sensing*. Springer Science+Business Media, 2011.

[30] L. Rossi, P. Fischer, T. Rohe, and N. Wermes. *Pixel Detectors: From Fundamentals to Applications*. Springer-Verlag Berlin Heidelberg, 2006.

[31] G. Gorfine, M. Hoeferkamp, G. Santistevan, and S. Seidel. Capacitance of silicon pixels. *Nuclear Instruments and Methods in Physics Research Section A*, 460(2-3):336–351, 2001.

[32] Daniel Durini. *High Performance Silicon Imaging*. Elsevier Ltd., 2014.

[33] Laurent Vivien and Lorenzo Pavesi. *Handbook of Silicon Photonics*. Taylor & Francis Group. LLC, 2013.

[34] Anders Brahme. *Comprehensive Biomedical Physics*. Elsevier B.V., 2014.

[35] KETEK GmbH. Ketek official website, 2016. www.ketek.net.

[36] Y. Okuto and C. R. Crowell. Energy-Conservation Consideration in the Characterization of Impact Ionization in Semiconductors. *Physical Review B*, 6(8):3076–3080, 1972.

[37] F. Nagy, M. Mazzillo, L. Renna, G. Valvo, D. Sanfilippo, B. Carbone, A. Piana, G. Fallica, and J. Molnár. Afterpulse and delayed crosstalk analysis on a STMicroelectronics silicon photomultiplier. *Nuclear Instruments and Methods in Physics Research Section A: Accelerators, Spectrometers, Detectors and Associated Equipment*, 759:44–49, 2014.

[38] W. Shockley and W.T Read. Statistics of the Recombinations of Holes and Electrons. *Physical Review*, 87:835–842, 1952.

[39] Andreas Schenk. *Advanced Physical Models for Silicon Device Simulation*. Springer-Verlag Wien GmbH, 1998.

[40] L. Gallego, J. Rosado, F. Blanco, and F. Arqueros. Modeling crosstalk in silicon photomultipliers. *Journal Of Instrumentation*, 8:P05010, 2013.

[41] R. McIntyre. On the avalanche initiation probability of avalanche diodes above the breakdown voltage. *IEEE transactions on Electron Devices*, 7(20):637–641, 1973.

[42] Alan Migdall, Sergey Polyakov, Jingyun Fan, and Joshua Bienfang. *Single-Photon Generation and Detection, Physics and Applications, Volume 45*. Elsevier Inc., 2013.

[43] Y. Du and F. Retière. After-pulsing and cross-talk in multi-pixel photon counters. *Nuclear Instruments and Methods in Physics Research Section A*, 596:396–401, 2008.

[44] Hermann Kolanoski and Norbert Wermes. *Teilchendetektoren: Grundlagen und Anwendungen*. Springer-Verlag Berlin Heidelberg, 2016.

[45] Frank Hoenniger. *Radiation Damage in Silicon - Defect Analysis and Detector Properties* -. PhD thesis, Universität Hamburg, 2007.

[46] Y. Musienko, A. Heering, R. Ruchti, M. Wayne, A. Koornev, and V. Postoev. Radiation Damage Studies of Silicon Photomultipliers for the CMS HCAL Phase I Upgrade. Vinci International Congress Center, Tours, France, June 2014. NDIP.

[47] E. Garutti, M. Gensch, R. Klanner, M. Ramilli, and C. Xu. Afterpulse effect in SiPMs and neutron irradiation studies. IEEE Nuclear Science Symposium and Medical Imaging Conference (NSS/MIC), November 2014.

[48] R. Klanner, V. Chmill, E. Garutti, M. Nitschke, and J. Schwandt. Study of the breakdown voltage of SiPMs. Vienna, Austria, February 2016. VCI 2016.

[49] Agilent Technologies. *Agilent E3631A Triple Output DC Power Supply*. Agilent Technologies, 5301 Stevens Creek Blvd, Santa Clara, CA 95051, United States, 2007.

[50] ATT Systems GmbH. *Manual, Control Unit A/P/M/C Series*. ATT Systems GmbH, Fraunhofer Strasse 11, 82152 Martinsried, Germany, 2006.

[51] Inc. Keithley Instruments. *Model 6517B Electrometer, User's Manual*. Keithley Instruments, Inc., 28775 Aurora Road, Cleveland, Ohio 44139, United States, 2008.

[52] Agilent Technologies. *Agilent E4980A Precision LCR Meter, User's Guide*. Agilent Technologies, 5301 Stevens Creek Blvd, Santa Clara, CA 95051, United States, 2007.

[53] R. Klanner, M. Centis Vignali, V. Chmill, E. Garutti, M. Nitschke, and J. Schwandt. Study of the radiation damage of SiPMs by neutrons. Strasbourg, France, October 2016. IEEE 2016.

[54] E. Garutti, M. Ramilli, C. Xu, W. L. Hellweg, and R. Klanner. Characterization and X-Ray damage of Silicon Photomultipliers. POS for the conference Technology and Instrumentation in Particle Physics, June 2014.

[55] MathWorks. Documentation: Evaluating goodness of fit, 2016. http://de.mathworks.com/help/curvefit/evaluating-goodness-of-fit.html.

[56] M. Ershov, H. C. Liu, L. Li, M. Buchanan, Z. R. Wasilewski, and A. K. Jonscher. Negative capacitance effect in semiconductor devices. *IEEE transactions on Electron Devices*, 45(10):2196–2206, 1998.

[57] ESPEC CORP. *Temperature and Humidity Cabinet & Low Temperature Cabinet, LU-123*. ESPEC CORP., Artisan Technology Group, 101 E. Mercury Drive, Champaign, IL 61822, 1999.

[58] Agilent Technologies. *Agilent 8110A 150 MHz Pulse Generator, User's Guide*. Hewlett Packard, Hewlett Packard GmbH, Herrenberger Str. 130, D-71034 Böblingen, 1995.

[59] Stanford Research Systems. *DG645 Digital Delay Generator*. Stanford Research Systems, Stanford Research Systems, Inc., 1290-C Reamwood Avenue, Sunnyvale, California 94089, 2008.

[60] Inc. Keithley Instruments. *Model 6487 Picoammeter/Voltage Source, User's Manual*. Keithley Instruments, Inc., 28775 Aurora Road, Cleveland, Ohio 44139, United States, 2003.

[61] CAEN S.p.A. *Technical Information Manual, Mod. V965/V965A, 16/8 channel dual range QDC*. CAEN S.p.A., Via della Vetraia, 11, 55049 Viareggio LU, Italy, 2008.

[62] Phillips Scientific. *Fast Pulse Preamplifier, Model 6954*. Phillips Scientific, 31 Industrial Ave., Mahwah, NJ 07430, 2008.

[63] Tektronix Inc. *DPO7000 Series and DSA/DPO70000 Series, Digital Phosphor Oscilloscope, Quick Start User Manual*. Tektronix Inc., 14200 SW Karl Braun Drive, P.O. Box 500, Beaverton, OR 97077, USA, 2008.

[64] Jozef Stefan Institute. Reactor TRIGA Mark II at Jozef Stefan Institute, 2016. www.rcp.ijs.si/ric/reactor-a.htm.

[65] Sonja Meike Jaster-Merz. Characterization of Silicon Photomultipliers as a Function of Humidity, 2014. Bachelor thesis, Universität Hamburg.

[66] E. Fred Schubert. *Light-Emitting Diodes*. Cambridge Universal Press, 2003.

[67] B. Aull, A. Loomis, D. Young, R. Heinrichs, B. Felton, P. Daniels, and D. Landers. Geiger-mode avalanche photodiodes for three-dimensional imaging. *Lincoln Laboratory Journal*, 13(2):335–349, 2002.

B Acknowledgement

First of all, I have to thank Prof. Erika Garutti for letting me write my master thesis in your group. I learned a lot of interesting things and got to know many nice people during my time here.
Secondly, I have to catch up on thanking the persons who helped me with my bachelor thesis, since I forgot to put an acknowledgment in it... So thank you Prof. Roland Wiesendanger, Dr. Alexander Schwarz and most of all thank you Hai Zhong and Gotthold Fläschner. Wish you all the best.

Also I would like to thank the following people and living beings:

- My mother and my father for that I am alive. As well as the rest of my family.
- Paola mi regalo, patita, equilibrio, bateria y fortuna. Gracias para ti, ti tiempo y ti apoyo. La vida es mejor contigo y la música suena mejor contigo.
- All my friends, the ones here in Hamburg and the others that I do not see that often anymore. Special thanks to my flatmate Cedric and his understanding for me neglecting my flatshare duties in the past months.
- My band, because everything is better with music and non-sense conversations about pigs in space.
- Otti (aka la bestia), my furry little nag and loyal companion, you're the best.
- Major thanks to Silka and Ottis dog gang, namely Ayka, Sammy and Jessi. Without someone looking after my dog the whole time, I do not know how I could have managed to write my master thesis. I am pretty sure Otti will miss you. In memory of Ayka, who is now hopefully running around again in dog heaven chasing giant steaks.
- Robert Klanner, for providing me with much more enlightenment than confusion, though he might state it the other way around. Also many many thanks for the last-minute analysis.
- Valery Chmill, for funny, interesting and productive co-working. Spasibo brat!
- Jörn Schwandt, for his knowledge and help with SiPMs.

- My office colleagues Christian, Finn and Ioannis, for a nice daily working atmosphere.

- The lunch and kicker gang, including the just mentioned as well as Daniele, Matteo, Milan, Ole, Sarah, Sebastian and Sebastian, Severin and Svenja.

- Michael Matysek and Peter Buhmann, for providing me with technical help, holes for my bass guitar as well as the nice microscope pictures.

- Rainer Peter Feller and Ronald Mohrmann, for support in IT questions.

- Everybody from the Prüfcenter and the Produktionskontrolle at Albis Plastics. You made working accompanying to my studies as pleasant as it could have been.

Some last thanks to the inventors of the following things: Music, pizza, fries, shibboleths, penguins, dogs, funny animal videos, awful puns, awesome dance moves like "The Robot", books, Astra, Mexikaner, the auto-complete function, anime, comic and science fiction series, cookies, chocolate, tattoos, weekends, hugs and kisses, Hamburg, WolframAlpha, comfy beds, multicolor pens and of course potato chips.

Thanks to all of you! I am a lucky guy to know so many great people :) I appreciate all the marks you left.

Eidesstattliche Erklärung

Ich versichere, dass ich die vorstehende Arbeit selbstständig und ohne fremde Hilfe angefertigt und mich anderer als der im beigefügten Verzeichnis angegebenen Hilfsmittel nicht bedient habe. Alle Stellen, die wörtlich oder sinngemäß aus Veröffentlichungen entnommen wurden, sind als solche kenntlich gemacht.

Ich bin mit einer Einstellung in den Bestand der Bibliothek des Fachbereiches einverstanden.

Hamburg, den _____ Unterschrift: _____